

Microfluidic Self-Assembly of Quantum Dot Compound Micelles

by

Greg Schabas
B.A.Sc., University of Toronto, 2005

A Thesis Submitted in Partial Fulfillment of the
Requirements for the Degree of

MASTER OF APPLIED SCIENCE

in the Department of Mechanical Engineering

© GREG SCHABAS, 2007
University of Victoria

All rights reserved. This thesis may not be reproduced in whole or in part, by photocopy or other means, without the permission of the author.

Microfluidic Self-Assembly of Quantum Dot Compound Micelles

by

Greg Schabas
B.A.Sc., University of Toronto, 2005

Supervisory Committee

Dr. David Sinton, Supervisor
(Department of Mechanical Engineering)

Dr. Majid Bahrami, Departmental Member
(Department of Mechanical Engineering)

Dr. Matt Moffitt, Outside Member
(Department of Chemistry)

Dr. Geoff Steeves, External Examination
(Department of Physics and Astronomy)

Supervisory Committee

Dr. David Sinton, Supervisor
(Department of Mechanical Engineering)

Dr. Majid Bahrami, Departmental Member
(Department of Mechanical Engineering)

Dr. Matt Moffitt, Outside Member
(Department of Chemistry)

Dr. Geoff Steeves, External Examination
(Department of Physics and Astronomy)

ABSTRACT

This thesis is devoted to the development of microfluidic processes for the controlled self-assembly of quantum dot compound micelles (QDCMs). Microfluidic processes are developed to combine the constituents (cadmium sulfide quantum dots, and block copolymer stabilizing chains) with water to facilitate self-assembly of the composite particles, QDCMs, through initial phase separation, subsequent growth, and eventual quenching. Two genres of microfluidic reactors are developed. The on-chip evolution of QDCM formation and growth is resolved through fluorescence microscopy; QDCM size distributions and associated statistics are determined through off-chip analysis by transmission electron microscopy (TEM). In a flow-focusing reactor, control over the mean size of QDCMs is demonstrated through both the water concentration and the growth time (or reactor channel length). Controlled QDCM self-assembly is also demonstrated in a multiphase gas-liquid reactor. In contrast to the flow-focusing reactor, increasing the multiphase reactor channel length results in a decrease in QDCM size and polydispersity.

TABLE OF CONTENTS

SUPERVISORY COMMITTEE.....	ii
ABSTRACT	iii
TABLE OF CONTENTS.....	iv
LIST OF FIGURES	vi
ACKNOWLEDGEMENTS	xiii

Chapter 1 INTRODUCTION

1.1 Aims and Motivation of this thesis.....	1
1.2 Microfluidics Transport Phenomena.....	4
1.2.1 The Navier-Stokes Equations and Microscale Fluid Flow	6
1.2.2 Diffusion-Based Microfluidic Mixing	9
1.2.3 Multiphase Microfluidics.....	12
1.3 Quantum Dot/Semiconductor overview	16
1.4 QDCM Self-Assembly Overview	19
1.5 Methodology	24
1.5.1 Microfabrication	24
1.5.1.1 Rapid Prototyping	24
1.5.1.2 Replica Molding.....	27
1.5.2 Experimental Methods.....	31
1.5.2.1 Fluorescence Microscopy	31
1.5.2.2 Working Solutions and Materials	33
1.5.2.3 Experimental Apparatus.....	34
1.5.2.4 Fluorescence Image Processing.....	37
1.5.2.5 Transmission Electron Microscopy (TEM)	38
1.6 Overview of this thesis.....	38

Chapter 2: QDCM SELF-ASSEMBLY IN SHEATH-FLOW MICROFLUIDIC REACTORS

2.1 Introduction.....	40
2.2 Analytical Analysis of Sheath-Flow Mixing	42
2.2.1 Diffusion in a Microfluidic T-Sensor	43
2.2.2 Particle Size Estimation in a Microfluidic Focuser	46
2.3 Experimental Setup.....	48
2.3.1 Microchannel Fabrication	48
2.3.2 Chemical Preparation.....	49
2.3.3 Flow delivery and control	50
2.3.4 Sample Collection and Image Processing.....	50

2.4 Results and Discussion	52
2.4.1 QDCM Self-Assembly in a Microfluidic T-Sensor	52
2.4.1.1 Fluorescence Results.....	53
2.4.2 QDCM Self-Assembly in a Microfluidic Flow-Focusing Reactor	57
2.4.2.1 Fluorescence Results.....	60
2.4.2.2 TEM Results	69
2.5 Summary	76

Chapter 3: QDCM SELF-ASSEMBLY IN MULTIPHASE MICROFLUIDIC REACTORS

3.1 Introduction.....	78
3.2 Experimental Setup.....	80
3.2.1 Microchannel Fabrication	81
3.2.2 Chemical Preparation.....	82
3.2.3 Flow delivery and control	83
3.2.4 Sample Collection and Image Processing.....	84
3.3 Results and Discussion	85
3.3.1 QDCM Self-Assembly in a Microfluidic Droplet Reactor	85
3.3.1.1 Fluorescence Results.....	87
3.3.2 QDCM Self-Assembly in a Microfluidic Gas-Liquid Reactor	93
3.3.2.1 Fluorescence Results.....	96
3.3.2.2 TEM Results	103
3.4 Summary	107

Chapter 4: CONCLUSIONS AND FUTURE WORK

4.1 Contributions of this Thesis.....	110
4.1.1 QDCM Self-Assembly in a Microfluidic T-sensor.....	111
4.1.2 QDCM Self-Assembly in a Microfluidic Focuser	111
4.1.3 QDCM Self-Assembly in a Multiphase Droplet Reactor	112
4.1.4 QDCM Self-Assembly in a Multiphase Gas-Liquid Reactor	113
4.2 Proposed Extensions of This Work.....	113
4.2.1 On-chip Diffusion-Based QDCM Size-Sorting in a Flow Focusing Microfluidic Reactor.....	114
4.2.2 Further Enhancement of the Gas-Liquid Microfluidic Reactor.....	115
4.2.3 The Formation of Large-Scale Quantum Dot Structures in a Microfluidic Device	115

REFERENCES	117
------------------	-----

LIST OF FIGURES

- Figure 1.1:** Pressure driven flow velocity profile, $u(y)$, between two parallel plates.... 8
- Figure 1.2:** Pressure driven flow velocity profile, $u(z)$, across the major axis in a rectangular cross-section microchannel..... 9
- Figure 1.3:** Channel configurations of two passive microfluidic mixers; a (a) T-mixer and a (b) focuser..... 11
- Figure 1.4:** Schematic illustration of droplet/bubble formation in microchannels. (a) The droplet/bubble phase enters the main channel. (b) The droplet begins to form and grows downstream. (c) The droplet grows to cover the entire cross-section of the main channel, increasing the pressure in the continuous phase until the neck of the droplet breaks. (d) The droplet moves downstream and the cycle is repeated. 14
- Figure 1.5:** Schematic showing mixing patterns inside droplets moving at downstream velocity u in a (a) straight channel and (b) a sinusoidal channel. The geometry of (b) induces time-dependent fluctuations in vortex size, enhancing mixing as a result. Similar vortex patterns exist in the carrier fluid [Günther et al. (2004)]...... 15
- Figure 1.6:** Schematic illustrating spacing of the conduction and valence energy bands for a (a) conductor, (b) insulator and (c) semiconductor [Cohen and Chelikowsky (1988)]. 17
- Figure 1.7:** Energy band/band-gap structure schematics for (a) a large semiconductor particle and (b) a quantum dot. In (a), the particle radius is much larger than its exciton Bohr radius and the energy levels are separated by an insignificant amount of energy. The band-gap energy remains constant for increasing particle size. In (b), the particle radius is smaller than the exciton Bohr radius and the energy levels in each energy band are discrete and separated by a significant amount of energy. Slight modifications to the size of the quantum dot can significantly alter the energy level spacing and band-gap energy [Brus (1991)]. 19
- Figure 1.8:** Schematic showing different classifications of micelles assembled from diblock copolymers. (a) Star-like and (b) crew cut regular micelles with a hydrophobic core and hydrophilic corona. (c) Star-like and (d) crew-cut reverse micelles with a hydrophobic corona and hydrophilic core..... 20

- Figure 1.9:** Illustration of the QDCM self-assembly process from PS-CdS QDs and PS-*b*-PAA block copolymer stabilizing chains with the addition of water. The PS-*b*-PAA and PS-CdS constituents agglomerate and form QDCMs when the water concentration in the DMF/solids solution exceeds the CWC (~1-2 wt%). When the water concentration reaches the freezing point (~8-11 wt%), the QDCMs become kinetically frozen and can no longer grow. 22
- Figure 1.10:** An example of a photomask used to produce a simple microfluidic focuser using negative-tone photoresist..... 25
- Figure 1.11:** Fabrication of a negative master of a microfluidic chip using photolithography. A cross-sectional schematic of the device is shown at various stages in the process; (a) after cleaning and drying of substrate; (b) after spin coating SU-8 onto the substrate, (c) during exposure to UV light; (d) during development and (e) when the process is finished. 27
- Figure 1.12:** A cross-sectional schematic of the microchip during the replica molding and sealing process at different stages of fabrication: (a) prior to pouring of PDMS onto the negative SU-8 master; (b) after pouring and curing of PDMS; (c) the PDMS microchip and a glass slide with a thin layer of cured PDMS are exposed to oxygen plasma for 30 seconds and then sealed to one another; (d) the final microchip ready for experimental use..... 29
- Figure 1.13:** Pictures of finished products at different stages of the microfabrication process: (a) finished negative SU-8 master on a silicon wafer; (b) silicon wafer in petri dish submerged in cured PDMS; and (c) cut-out and sealed PDMS microchip ready for use..... 30
- Figure 1.14:** The absorption and emission spectra of PS-CdS QDs. The emission spectrum was obtained using an excitation wavelength of 400 nm [Yusuf et al. (2007a)]. 32
- Figure 1.15:** (a) Absorption and (b) emission spectrum of fluorescein dissolved in solution at different pH (Invitrogen Inc, ON). 33
- Figure 1.16:** The experimental apparatus used in this work. The microchip from Figure 1.13c is mounted on the DMI 6000B microscope (left) connected via teflon tubing to the gastight syringes mounted on syringe pumps (right). 35

- Figure 1.17:** Schematic illustrating the operating principles of a fluorescence filter cube. The filter cube consists of two perpendicular filters, the excitation and emission filters with a dichroic mirror positioned in between them at a 45° angle. The excitation and emission filters block all light from passing except that which is in the excitation and emission wavelength range of the fluorescent particle respectively. The dichroic mirror reflects the shorter wavelength excitation light but is transparent to the longer wavelength emission light. The excitation light passes through the excitation filter and is reflected upwards by the dichroic mirror and then passes into the microscope objective before impinging on the sample. After undergoing the Stokes shift, the light is re-emitted at a longer wavelength. This emitted light travels downward and passes through the dichroic mirror and the emission filter before reaching the CCD camera. 36
- Figure 2.1:** Geometry of the T-sensor mixing problem showing the boundary conditions used to derive Equation 2.3 from Equation 2.1. Equation 2.3 is only valid if $c_w \approx 0$ at the right-side wall (or equivalently, the z -domain is effectively infinite). 43
- Figure 2.2:** The predicted water concentration profiles using Equation 2.3 at 4 downstream (x -direction) positions, in the T-sensor. The walls of the T-sensor are located at $z = \pm 0.75$ mm and the water concentration did not change significantly at the walls. The c_w concentration (~1-2 wt%) is indicated by a dashed line (assuming a c_0 corresponding to a 50 wt% water-DMF solution). 45
- Figure 2.3:** Schematic of the microfluidic T-sensor used for QDCM self-assembly.. 53
- Figure 2.4:** Compilation of normalized fluorescence images of the T-sensor taken during the QDCM self-assembly process at 11 different downstream locations in the mixing channel. 56
- Figure 2.5:** Normalized cross-stream fluorescence intensity plots in the DMF/solids stream of the T-sensor at five downstream locations in the mixing channel. 57
- Figure 2.6:** Schematic of the microfluidic flow-focusing reactor used for the self-assembly of QDCMs. The DMF/solids stream was focused by a sheath-flow of DMF/water and species mixing and particle growth occurred in the 240 mm long growth channel before the quench step where sufficient water was focused into the system such that the QDCMs became kinetically frozen. The flowrates at the DMF/water and water inlets were two- and six-times greater than that of the DMF/solids inlet, respectively. 59

- Figure 2.7:** Normalized fluorescence images of the QDCM self-assembly process in the flow-focusing reactor (at the downstream locations indicated) for a total growth channel flowrate of $Q = 3 \mu\text{L}/\text{min}$ ($u = 4 \text{ mm}/\text{s}$) and total cross-sectional average water concentrations of (a) 0 wt%, (b) 4 wt%, (c) 8 wt%, (d) 33 wt%, and (e) 33 wt% with a fluorescein tracer imaged. 64
- Figure 2.8:** Normalized fluorescence images of the QDCM self-assembly process in the flow-focusing reactor (at the downstream locations indicated) for a total growth channel flowrate of $Q = 9 \mu\text{L}/\text{min}$ ($u = 12 \text{ mm}/\text{s}$) and total cross-sectional average water concentrations of (a) 0 wt%, (b) 4 wt%, (c) 8 wt%, (d) 33 wt%, and (e) 33 wt% with a fluorescein tracer imaged. 65
- Figure 2.9:** Fluorescein and QD emission based analysis: combined image of fluorescein emission (shown red) and QD emission (shown green) with expanded cross-stream region. 66
- Figure 2.10:** Cross-stream QDCM normalized intensity profiles with $Q = 3 \mu\text{L}/\text{min}$ at 5 different downstream locations in the growth channel (a) 0 mm, (b) 15 mm, (c) 50 mm, (d) 110 mm and (e) 230 mm. A normalized intensity value of 1 represents base-case QD emission prior to QDCM formation. ...
..... 67
- Figure 2.11:** Cross-stream QDCM normalized intensity profiles with $Q = 9 \mu\text{L}/\text{min}$ at 5 different downstream locations in the growth channel (a) 0 mm, (b) 15 mm, (c) 50 mm, (d) 110 mm and (e) 230 mm. A normalized intensity value of 1 represents base-case QD emission prior to QDCM formation. ...
..... 68
- Figure 2.12:** Cross-stream fluorescein intensity for the 33 wt% trial at growth channel flowrates of (a) $3 \mu\text{L}/\text{min}$ and (b) $9 \mu\text{L}/\text{min}$ 69
- Figure 2.13:** A TEM image of QDCM particles formed with the microfluidics-based method. These particles were formed at a total flowrate of $Q = 3 \mu\text{L}/\text{min}$ ($u = 4 \text{ mm}/\text{s}$) and a steady-state water concentration of 4 wt%. 73
- Figure 2.14:** Representative shadowed TEM images of QDCMs formed in the flow-focusing microfluidic reactor. The scale bars indicate 250 nm in all cases (TEM images were black/white inverted for presentation). The flowrate was $3 \mu\text{L}/\text{min}$ in (a), (c) and (e) at steady state water concentrations of 4, 8 and 33 wt% respectively. The flowrate was $9 \mu\text{L}/\text{min}$ in (b), (d) and (f) at steady state water concentrations of 4, 8 and 33 wt% respectively. 74

- Figure 2.15:** QDCM particle size distributions and statistics corresponding to the samples shown in the representative TEM images in Figure 2.14. The flowrate was 3 $\mu\text{L}/\text{min}$ in (a), (c) and (e) at steady state water concentrations of 4, 8 and 33 wt% respectively. The flowrate was 9 $\mu\text{L}/\text{min}$ in (b), (d) and (f) at steady state water concentrations of 4, 8 and 33 wt% respectively. 75
- Figure 2.16:** Summary plot showing measured mean QDCM diameters as a function of sheath fluid water concentration and total flowrate. 76
- Figure 3.1:** Schematic of the microfluidic droplet reactor used for QDCM self-assembly experiments. 86
- Figure 3.2:** Fluorescein emission of fluorescein/water droplets formed in the mixing channel of the microfluidic droplet reactor. (a) No surfactant was dissolved in the PFD. (b) A surfactant, 1H,1H,2H,2H-perfluorooctanol, was dissolved in the PFD at a concentration of 9 wt%. In both cases, the totals inlet flowrates for the fluorescein/water phase and PFD were 0.3 and 0.6 $\mu\text{L}/\text{min}$ respectively. (contrast ratio and brightness have been adjusted for clarity of presentation) 90
- Figure 3.3:** QD emission of DMF/water plugs formed in the growth channel of the droplet reactor with a steady-state water concentration of 4 wt%. (a) No surfactant was dissolved in the PFD. (b) A surfactant, 1H,1H,2H,2H-perfluorooctanol, was dissolved in the PFD at a concentration of 9 wt%. In both cases, the total inlet flowrates for the DMF/water/solids phase and PFD were 0.3 and 0.6 $\mu\text{L}/\text{min}$ respectively. (contrast ratio and brightness have been adjusted for clarity of presentation) 91
- Figure 3.4:** QD emission at the injector of the droplet reactor with a steady-state water concentration of 33 wt%. (a) No surfactant was dissolved in the PFD. (b) A surfactant, 1H,1H,2H,2H-perfluorooctanol, was dissolved in the PFD at a concentration of 9 wt%. In both cases the reactor was highly unstable and did not facilitate the QDCM self-assembly process in a controlled or detectable manner (contrast ratio and brightness have been adjusted for clarity of presentation). 92
- Figure 3.5:** QD emission in the expansion chamber of the droplet reactor with a steady-state water concentration of 4 wt%. The small fluorescent dots likely represent the emission of individual QDCMs. However the small size of these dots and the background fluorescent emission made size measurements of QDCMs from these images impractical. 92
- Figure 3.6:** Schematic of the 200 mm long microfluidic gas-liquid reactor for QDCM self-assembly experiments. 95

- Figure 3.7:** Schematic of the 740 mm long microfluidic gas-liquid reactor for QDCM self-assembly experiments. 96
- Figure 3.8:** QD emission in the microfluidic gas-liquid bubble reactor during operation: the images were captured at (a) the injector, (b) the middle of the growth channel and (c) at the quencher. These images were captured in the 200 mm reactor at a steady-state water concentration was 4 wt% with the on-chip quencher in operation (prior to the breakdown of flow). The variations in fluorescent intensity of the plugs from the bottom to top of each image is a byproduct of a non-uniform distribution of excitation light and does not indicate any change in the properties of QDCMs. (contrast ratio and brightness have been adjusted for clarity of presentation). 99
- Figure 3.9:** Fluorescein emission in multiphase fluorescein/water-argon system. The intensity peaks seen at the two-phase interface are attributed to total internal reflection at the gas-liquid interface. 100
- Figure 3.10:** Bubble formation process at the injector of the gas-liquid reactor. These images were taken at 100 ms intervals. The steady-state water concentration was 4 wt%. (contrast ratio and brightness have been adjusted for clarity of presentation) 100
- Figure 3.11:** Normalized fluorescein emission taken at three downstream locations in the mixing channel during the trial where fluorescein was added to water and the steady-state water concentration was 33 wt%. The images were captured at downstream distances of (a) 0 mm, (b) 2 mm and (c) 5 mm from the injector. 101
- Figure 3.12:** Normalized QD emission in the mixing channel for the 33 wt% water trial. The images were captured at downstream distances of (a) 0 mm, (b) 2 mm and (c) 5 mm from the injector. 102
- Figure 3.13:** Representative shadowed TEM images of QDCMs formed in a 200 mm gas-liquid reactor at a steady-state water concentration of 4 wt%. (TEM images were black/white inverted for presentation). 105
- Figure 3.14:** Representative shadowed TEM images of QDCMs formed in a 740 mm gas-liquid reactor at a steady-state water concentration of 4 wt%. (TEM images were black/white inverted for presentation). 105
- Figure 3.15:** Representative shadowed TEM images of QDCMs formed in a 200 mm gas-liquid reactor at a steady-state water concentration of 33 wt%. (TEM images were black/white inverted for presentation). 106

Figure 3.16: QDCM particle size distributions and statistics for QDCMs formed in the microfluidic gas-liquid reactor. In each case, the steady-state water concentration and reactor length were (a) 4 wt% and 200 mm, (b) 4 wt% and 740 mm and (c) 33 wt% and 200 mm. 107

Figure 4.1: Large QD structures formed inside microfluidic reactors. The largest particles shown have dimensions on the order of 100 μm 116

ACKNOWLEDGEMENTS

I would like to express my sincerest thanks to my supervisor, Dr. David Sinton, for his guidance, assistance and support in this endeavor and for providing me with the opportunity to work with him. I would also like to thank Dr. Matt Moffitt from the Department of Chemistry for his large contribution to this work. Also, I would like to acknowledge and thank the members of the Microfluidics Lab, past and present, for the support, feedback and assistance they have provided during my tenure.

Finally, it is to my family that I dedicate this work for their loving support.

Chapter 1

INTRODUCTION

1.1 Aims and Motivation of this thesis

Microfluidics is the study and application of fluid flow in microstructures [Stone et al. (2004)]. Microfluidic, or ‘on-chip’, processes can offer several advantages over their macroscale counterparts with respect to control. Most notably, in the absence of turbulence, chemical processes may be controlled very accurately using a combination of laminar flow and species diffusion. Furthermore, microfluidic processes benefit from the increase in surface area to volume ratio which accompanies miniaturization [Sinton (2004)]. This translates into improved heat dissipation, shorter processing times and a significant reduction in sample and reagent requirements. Interest in microfluidics has grown tremendously over the past decade primarily due to the potential of microfluidic based analytical and diagnostic devices [Dolnik et al. (2000); Wang (2000); Beebe et al. (2002); Reyes et al. (2002); Erickson and Li (2004); Kamholz (2005); Yager et al.

(2006)]. Microfluidic technology has also shown significant promise in power generation in the form of miniaturized fuel cells [Dyer (2002); Bazylak et al. (2005); Kjeang et al. (2007)] and for the controlled synthesis of nanoparticles [Jahn et al. (2002); Shestopalov et al. (2004); Yen et al. (2005)].

Colloidal quantum dots (QDs) are semiconductor nanoparticles (typically 1-10 nm in diameter) with size-tunable optical and electronic properties that are significantly different from bulk semiconductor materials. Their unique characteristics have motivated the study of QDs as potential functional elements in photonics, electroluminescence, and sensing [Krishnadasan et al. (2004)]. Specifically, when a semiconductor's particle radius becomes smaller than its exciton Bohr radius, the energy levels in the valence and conduction bands are no longer continuous but discrete [Krishnadasan et al. (2004)]. In this regime, the emission frequency of the QD becomes a function of the size of the particle. In particular, the intense and size tunable light emission exhibited by colloidal II/VI semiconductors such as cadmium sulfide (CdS) QDs, make them intriguing candidates for use in fluorescent bio-labels [Wang and Moffitt (2004)]. However biological applications using QDs have been hindered by the difficulties encountered in assembling these inorganic semiconductors into larger, biocompatible probes [Pinaud et al. (2005)].

It has been previously demonstrated that hydrophobic block copolymer-stabilized CdS QDs with an external polystyrene (PS) brush layer (PS-CdS) and polystyrene-*block*-poly(acrylic acid) (PS-*b*-PAA) stabilizing chains co-dissolved in dimethylformamide (DMF) will organize into spherical assemblies termed quantum dot compound micelles (QDCMs) with the addition of water [Moffitt et al. (1998); Yusuf et al. (2007a); Yusuf et

al. (2007b)]. Quantum dot compound micelles offer numerous advantages over CdS QDs due to their larger/controllable size, structural complexity and their stability in aqueous media [Moffitt et al. (1998)]. These characteristics make them promising candidates for biological and photonic applications [Yusuf et al. (2007a)]. In particular, QDCMs are good candidates for use as fluorescent bio-labels which are commonly used in biomedical and bioimaging applications [Pinaud et al. (2005)]. For these applications, control over QDCM size is a critical issue since transport and cell uptake in biological systems is size dependent [Yusuf et al. (2007a)]. It has also been demonstrated that QDCMs can be organized into three-dimensional photonic crystal arrays which could be used as materials for QD lasers and optical switching devices [Yusuf et al. (2007b)]. In a photonic crystal array, particle polydispersity is a critical issue and a very narrow QDCM size distribution is required to achieve macroscale ordering [Yusuf et al. (2007b)].

Microfluidic confinement and associated mass transport phenomena have been shown to be well suited to the controlled synthesis of QDs [Krishnadasan et al. (2004); Yen et al. (2005)]; in addition, microfluidics shows promise for the controlled self-assembly of CdS QDs into QDCMs since self-assembly events are generally sensitive to local concentrations of reagents (e.g. QD concentrations, pH, water content), which can be finely tuned in a microfluidic environment. Microfluidics has already been successfully applied to a variety of nanoparticle synthesis applications including the size controlled high-temperature synthesis of CdSe nanocrystals [Chan et al. (2002); Chan et al. (2003)], synthesis of Janus particles with narrow size distributions [Nie et al. (2006)] and for the synthesis of a variety of polymer particles [Seo et al. (2005)]. Microfluidic processes have also been applied to accelerate the synthesis process of titanium oxide

nanostructures [Cottam et al. (2006)]. The self-assembly of a variety of other nanostructures including organosilicon microcapsules [Steibacher et al. (2006)] and lipid-bilayer membranes [Malmstadt et al. (2006)] has also been demonstrated on microfluidic devices.

The aim of this thesis is to develop microfluidic strategies for producing QDCMs with narrow and controllable size-distributions. Two microfluidic strategies are employed: the first strategy involves mixing the basic building blocks with water in a continuous sheath-flow reactor where species mixing is dominated by diffusion. The second strategy involves introducing a second immiscible phase into the system such as oil or gas to create a multiphase system where mixing occurs rapidly due to chaotic advection [Song et al. (2003)].

Though the focus in this work was limited to the self-assembly of QDCMs from CdS QDs, the techniques developed here are applicable to a range of micelle self-assembly processes involving block copolymers [Malmsten and Lindman (1992); Gao and Eisenberg (1993)]. Micelles such as these have applications in biology and medicine, particularly targeting drug delivery [Katoaka et al. (2001)].

1.2 Microfluidics Transport Phenomena

Microfluidics refers to fluid flow in channels and structures with characteristic dimensions on the order of 1-1000 μm . The flow characteristics of microscale flow are significantly different than its macroscale counterpart due to its laminar nature and characteristically low Reynolds number. The Reynolds number, Re , is a dimensionless

number that is the ratio of the inertial to viscous forces in a fluid and is commonly used to classify fluid flow into one of two regimes, laminar and turbulent flow [Reynolds (1883)]. Laminar flow is characterized by fluid particles moving slowly in smooth parallel lines whereas turbulent fluid flow is fast and chaotic. The Reynolds number is calculated using the formula shown below.

$$\text{Re} = \frac{\rho V_c d_H}{\mu} \quad (1.1)$$

Here, V_c is the characteristic fluid velocity, d_H is the characteristic channel diameter, ρ is the fluid density and μ is the fluid's dynamic viscosity. Because of the small channel dimensions associated with microfluidics, the Reynolds number is commonly on the order of unity and is well within the laminar flow regime [Sinton (2004)]. At low Reynolds number, the effects of inertial and gravitational forces become negligible and viscous and surface tension forces dominate [Purcell (1976)]. The absence of inertia also makes microfluidic flow effectively instantaneous, meaning that the fluid cannot store momentum and fluid motion is not dependent on any forces exerted on it at a previous moment in time [Purcell (1976)]. The microfluidic systems operated in this work had characteristic dimensions on the order of 100 μm , running at fluid velocities on the order of 1 mm/s, with a corresponding Reynolds number on the order of 0.1 and thus low Reynolds number behavior is expected.

The study of microfluidic transport phenomena has been documented in a number of review papers and texts covering topics such as fluid flow [Sharp et al. (2002); Kirby and Hasslebrink (2004); Stone et al. (2004)], diffusion [Yager et al.(2004); Squires and Quake (2005)] and multiphase kinetics [Bringer et al. (2004); deMello (2006)]. In the

context of this thesis, the most pertinent aspects of these topics are briefly outlined in the remainder of this section.

1.2.1 The Navier-Stokes Equations and Microscale Fluid Flow

Based on Newton's 2nd Law, the Navier-Stokes equations describe fluid motion in an Eulerian fixed frame of reference. They establish that changes of momentum on an infinitesimally small fluid element results from the net forces acting on the element. These include body forces such as gravity and surface forces such as changes in pressure and shear across the surface of the element. The assumptions required for the validity of the Navier-Stokes equation are incompressible flow, constant viscosity and a Newtonian fluid meaning that shear is proportional to the velocity gradient [White (2003)]. Full derivations of the Navier-Stokes equations are available in fluid mechanic textbooks [Acheson (1990); White (2003)]. The Navier-Stokes equations are shown in Equation 1.2 in vector form.

$$\rho \underbrace{\left(\frac{\partial \vec{V}}{\partial t} + (\vec{V} \cdot \nabla) \vec{V} \right)}_{\text{acceleration}} = \underbrace{\rho \vec{g}}_{\text{body forces}} - \underbrace{\nabla p}_{\text{surface forces}} + \mu \nabla^2 \vec{V} \quad (1.2)$$

Here, \vec{g} is the gravitational field, p is the pressure and \vec{V} is the velocity vector. Each term represents one type of force (per unit volume) that may be exerted on a fluid element. The $\rho \vec{g}$ term represents the gravitational forces, the ∇p term represents the forces from pressure changes, the $\mu \nabla^2 \vec{V}$ term represents the viscous (shear) forces around

the surface of the element (for a Newtonian fluid) and the term on the left-hand side collectively represents the acceleration of the fluid.

A non-dimensionalized version of the Navier-Stokes equations can be derived by applying the following substitutions to Equation 1.2:

$$\vec{V} = \vec{V}^* V_c, \quad \vec{\nabla} = \vec{\nabla}^* \left(\frac{1}{d_H} \right), \quad t = t^* \left(\frac{d_H}{V_c} \right), \quad p = p^* (\rho V_c^2), \quad \vec{g} = \vec{g}^* \left(\frac{V_c^2}{d_H} \right) \quad (1.3)$$

Here, the \vec{V}^* , $\vec{\nabla}^*$, t^* , p^* , and \vec{g}^* terms are non-dimensionalized versions of their respective counterparts. Substituting Equations 1.3 into 1.2 and replacing the ρ , V_c , d_H and μ terms with Re using Equation 1.1 yields the non-dimensionalized Navier-Stokes equations.

$$\text{Re} \left(\frac{\partial \vec{V}^*}{\partial t^*} + (\vec{V}^* \cdot \vec{\nabla}^*) \vec{V}^* \right) = \text{Re} \left(\rho \vec{g}^* + \vec{\nabla}^* p^* \right) + \vec{\nabla}^{*2} \vec{V}^* \quad (1.4)$$

Equation 1.4 shows that the influence of the gravitational and inertial effects on the motion of a fluid particle vary linearly with Re. Thus at low Reynolds numbers, the viscous forces dominate. The non-dimensionalized Equation 1.4 also shows that in order to drive a low Reynolds number flow, a relatively high pressure gradient is required. By removing the inertial and gravitational terms the Navier-Stokes equations can be simplified into linear partial differential equations known as the Stokes equations. The Stokes equation, written in Cartesian coordinates (x,y,z) is shown below for fluid flow in the x -direction.

$$\frac{\partial p}{\partial x} = \mu \left(\frac{\partial^2 u}{\partial x^2} + \frac{\partial^2 u}{\partial y^2} + \frac{\partial^2 u}{\partial z^2} \right) \quad (1.5)$$

Here, u , is the velocity component of \vec{V} in the x -direction.

An important solution to the Stokes equations is that of laminar, fully developed, steady-state, parallel flow between two parallel plates separated by a distance H . The solution for the velocity profile is one-dimensional with the origin ($y = 0$) found at the midpoint between the two plates.

$$u(y) = \frac{1}{2\mu} \frac{\partial p}{\partial x} \left(y^2 - \left(\frac{H}{2} \right)^2 \right), -\frac{H}{2} \leq y \leq \frac{H}{2} \quad (1.6)$$

This type of flow is called Poiseuille flow and it is very common in microfluidics. Specifically, Poiseuille flow is approximated in channels with a small depth relative to other dimensions. The resulting velocity profile is parabolic, reaching its peak at the midpoint between the two plates and zero at each end due to the no-slip wall condition. The velocity profile of Poiseuille flow is shown below in Figure 1.1 [White (2003)].

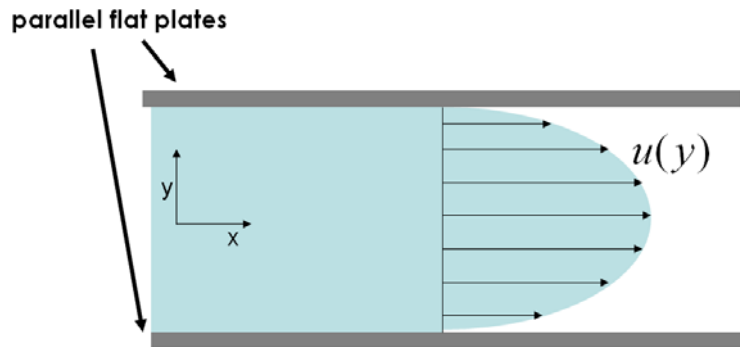


Figure 1.1: Pressure driven flow velocity profile, $u(y)$, between two parallel plates.

The microchannels used in this work were rectangular in cross-section and the velocity profile varied in both cross-sectional dimensions. For a rectangular cross-section, the velocity profile is only roughly parabolic along the minor axis. Along the major axis, the velocity profile develops near the wall on a length-scale proportional to

the channel depth, and is more uniform across the remainder of the major axis. As the aspect ratio of the rectangle increases, the velocity profile along the major axis becomes more uniform, only dropping to zero very close to the walls, as shown in Figure 1.2.

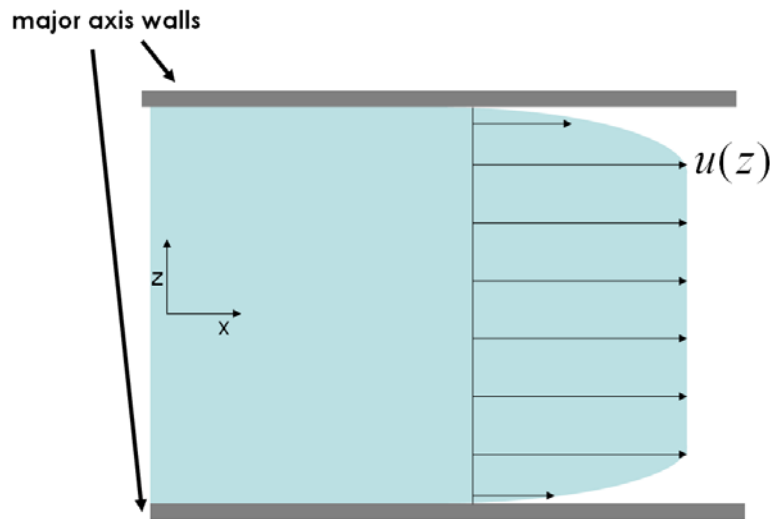


Figure 1.2: Pressure driven flow velocity profile, $u(z)$, across the major axis in a rectangular cross-section microchannel.

1.2.2 Diffusion-Based Microfluidic Mixing

Due to the absence of turbulence in microfluidic flow, fluid mass transport inside a microchannel is often dominated by diffusion. In terms of mass transport, diffusion is the movement of particles from areas of high concentration to low concentration in response to a concentration gradient. Unlike mixing from advection, diffusion is a passive process [Hertzog et al. (2006)].

Fast and effective mixing of species and reagents is central to many on-chip microfluidic processes [Nguyen and Wu (2004)] including chemical synthesis [Jahn et al.

(2004)], immunoassays [Vilkner et al. (2002)] and protein analysis [Kakuta et al. (2003); Hertzog et al. (2006)]. Microfluidic mixing strategies can be divided into two categories: active mixing where external forces such as pressure modulations are utilized to enhance mixing and passive mixing where two or more streams mix via cross-stream diffusion [Coleman et al. (2006)]. The most basic form of passive mixing utilizes a T-mixer or focuser configuration [Nguyen and Wu (2005)], shown in Figure 1.3, where co-laminar streams are combined and mixing occurs mainly via diffusion in the cross-stream direction. Other passive configurations such as parallel and serial lamination [Nguyen and Wu (2005)] and the addition of grooves [Nguyen and Wu (2006)] or heterogeneous surface patches [Erickson and Li (2001)] in the mixing channel have been developed as a means of increasing mixing rates. Although in many microfluidic applications fast mixing of analytes and reagents is desired [Coleman et al. (2006)], in some cases the slow rates of diffusion that characterize the T-mixer have been exploited to investigate rates of chemical reactions [Hatch et al. (2004)]. In those cases the T-mixer geometry is referred to as a T-sensor.

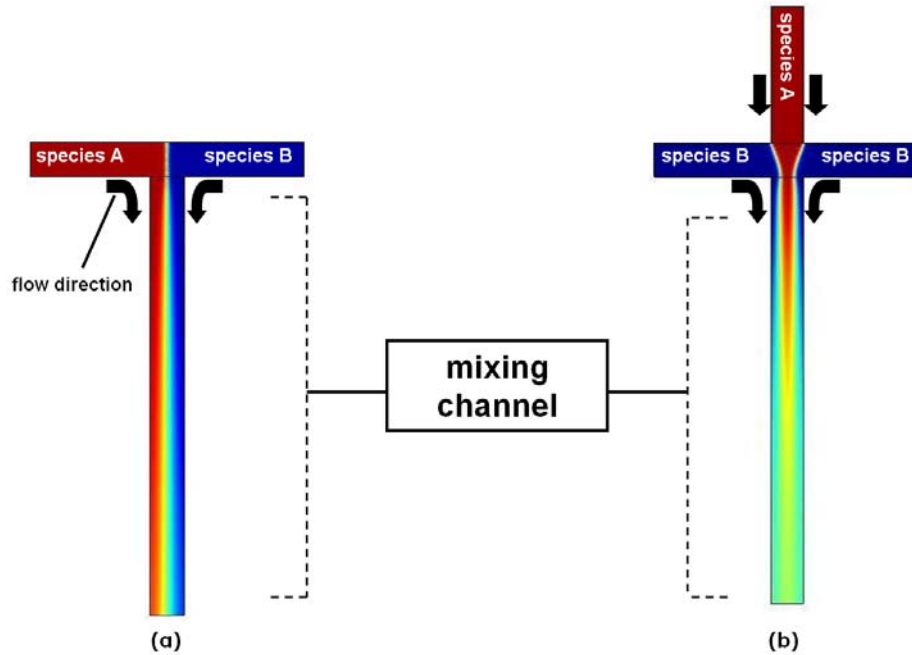


Figure 1.3: Channel configurations of two passive microfluidic mixers; a (a) T-mixer and a (b) focuser.

The general equation for mass transport, termed the convective diffusion equation [Probstein (1994)] which combines unsteady, advective, diffusive and reaction effects is shown below.

$$\underbrace{\frac{\partial c_A}{\partial t}}_{\text{unsteady term}} + \underbrace{\vec{V} \cdot \vec{\nabla} c_A}_{\text{advective term}} = \underbrace{\phi \vec{\nabla}^2 c_A}_{\text{diffusion term}} + \underbrace{r_A}_{\text{reaction rate}} \tag{1.7}$$

Here, c_A is the concentration of species A, ϕ is the diffusion coefficient and r_A is the molar rate of production of species A per unit volume. For passive co-laminar microfluidic mixers such as the T-mixer and focuser, a number of simplifications can be made to Equation 1.7. The advective term can be eliminated as the downstream fluid velocity is orthogonal to the cross-stream concentration gradients. The reaction rate term,

r_A , can be eliminated assuming no chemical reaction involving species A is underway. Further assuming only one-dimensional cross-stream diffusion, these simplifications lead to the one-dimensional diffusion equation shown below.

$$\frac{\partial c(z,t)}{\partial t} = \mathcal{D} \frac{\partial^2 c(z,t)}{\partial z^2} \quad (1.8)$$

Here, z is the cross-stream position across the channel. The one-dimensional diffusion equation can often be used to predict (either analytically or numerically with the aid of a computational fluid dynamics software), the rate mixing of two or more microfluidic co-laminar streams along the length of the channel. However, Equation 1.8 assumes one-dimensional cross-stream diffusion and does not include multi-dimensional effects such as dispersion which arise due to the non-uniformity of the pressure driven velocity profile [Ismagilov et al. (2000); Stone et al. (2004); Bazylak et al. (2005)]. In a co-laminar stream configuration, dispersion results in an increase in the rate of mixing above that which would be predicted using Equation 1.8.

1.2.3 Multiphase Microfluidics

Achieving rapid and efficient mixing in single-phase microfluidics is problematic due to the relatively slow-nature of diffusion [deMello (2006)]. Also, the parabolic velocity profile associated with pressure driven flow yields an on-chip residence time distribution (RTD) that may cause significant variation in the yield, efficiency and product distribution of an on-chip reaction [deMello (2006)]. Multiphase microfluidics can mitigate these problems by localizing reagents into discrete aqueous droplets or plugs separated by an immiscible fluid such as oil [Tice et al. (2003); Song et al. (2004)] or gas

[Günther et al. (2004); Günther and Jensen (2006)]. Multiphase kinetics offers numerous advantages over single-phase flow due to the presence of chaotic advection [Bringer et al. (2003)] which causes reactants to mix extremely rapidly and also because the uniform, steady velocity of a droplet or plug significantly reduces the RTD when compared to single-phase pressure driven flow [Günther and Jensen (2006)]. These characteristics have made multiphase microfluidic systems a popular choice for nanoparticle synthesis applications [Günther et al. (2004); Shestopalov et al. (2004); Yen et al. (2005)].

The mechanisms of droplet and bubble formation in fluid flow depend on the value of the Capillary number [Garstecki et al. (2006)]. The capillary number, shown in Equation 1.9, is a dimensionless quantity which represents the ratio of the viscous forces to the interfacial forces.

$$Ca = \frac{\mu u}{\gamma} \quad (1.9)$$

Here, γ is the interfacial tension at the fluid interface. In microfluidics, values of the capillary number are typically small ($Ca < 10^{-2}$) [Garstecki et al. (2006)]. In this regime, break-up is not dominated by shear stresses but by the pressure drop which arises across the emerging droplet or bubble [Garstecki et al. (2006)]. When two immiscible liquid phases are merged in a microchannel, the stream of the droplet phase penetrates into the main channel containing the continuous phase and a droplet begins to grow. As the droplet grows to cover the entire cross-section of the main channel, the flow upstream of the emerging droplet becomes inhibited, causing an increase in pressure. Once the pressure reaches a critical value, the neck connecting the droplet to its inlet channel breaks and the droplet moves downstream [Garstecki et al. (2006)]. A schematic of this process is provided in Figure 1.4. The formation of bubbles in a gas-liquid system occurs

in a similar fashion [Garstecki et al. (2006)]. The wetting properties of the fluids dictate which phase forms droplets and which phase constitutes the carrier fluid. The less wetting fluid, the one with a higher interfacial tension at the channel walls, forms into droplets.

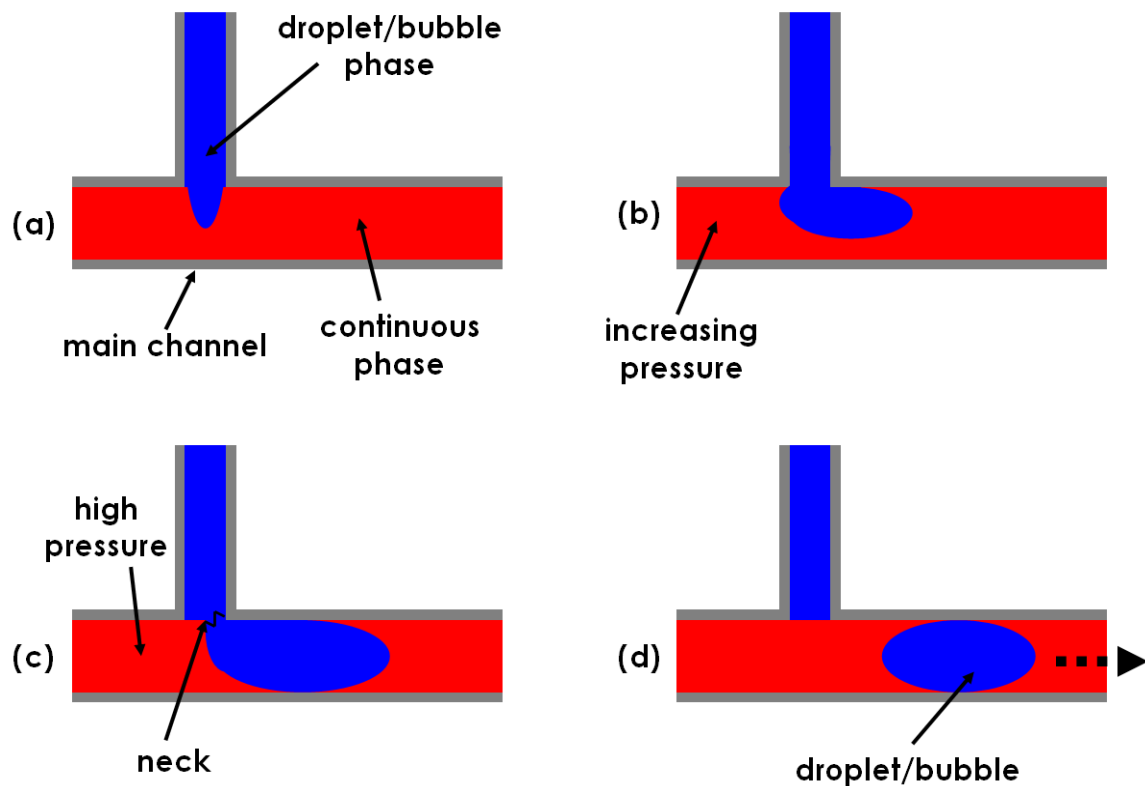


Figure 1.4: Schematic illustration of droplet/bubble formation in microchannels. (a) The droplet/bubble phase enters the main channel. (b) The droplet begins to form and grows downstream. (c) The droplet grows to cover the entire cross-section of the main channel, increasing the pressure in the continuous phase until the neck of the droplet breaks. (d) The droplet moves downstream and the cycle is repeated.

In multiphase flow, the motion of the two-phase interface induces chaotic advection in the form of pairs of counter-rotating vortices within a droplet [Song et al. (2004)]. Similar motion is induced within the plugs of the carrier fluid [Günther et al.

(2004)]. The advection produced in this manner significantly enhances mixing as compared to laminar cross-stream diffusion [Tice et al. (2003)]. Multiphase mixing can be further enhanced using a sinusoidal channel geometry which induces time-dependent variations in the streamline patterns of the vortices [Song et al. (2003)], as shown in Figure 1.5. Using this technique, complete mixing of aqueous fluid streams is attainable in as little as 2 ms [Song et al. (2003)].

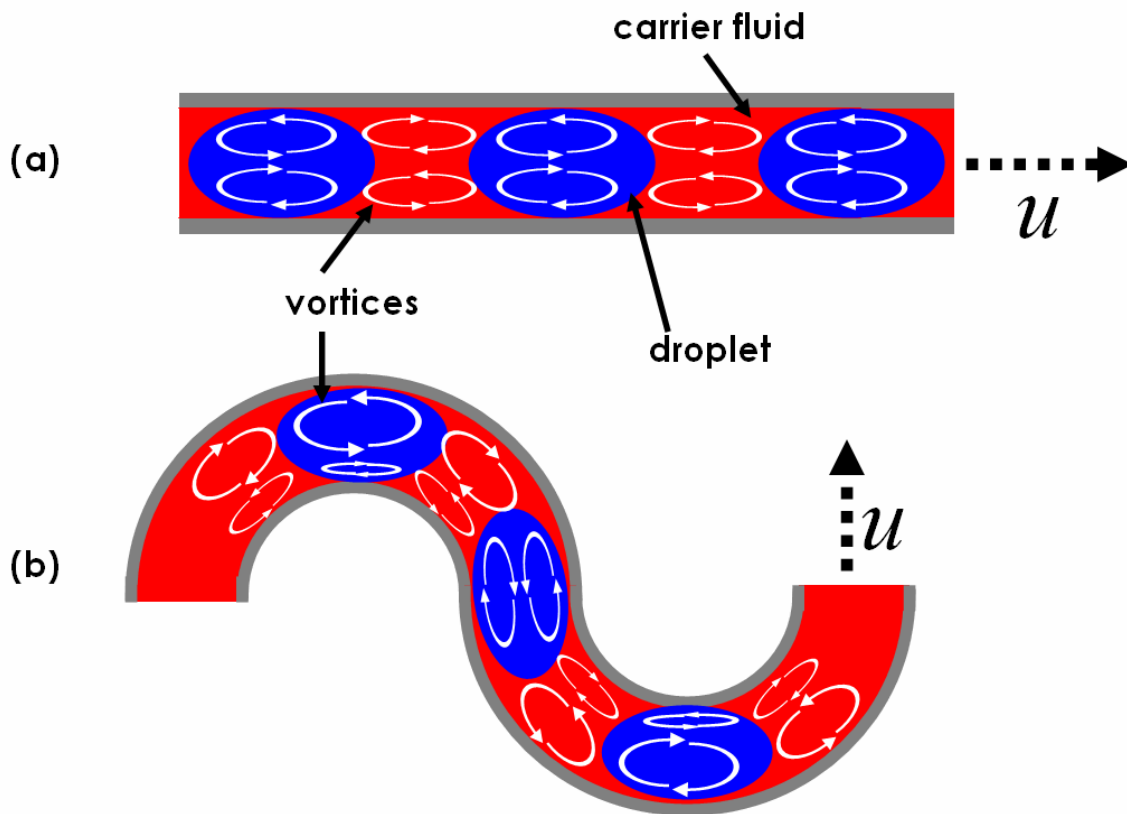


Figure 1.5: Schematic showing mixing patterns inside droplets moving at downstream velocity u in a (a) straight channel and (b) a sinusoidal channel. The geometry of (b) induces time-dependent fluctuations in vortex size, enhancing mixing as a result. Similar vortex patterns exist in the carrier fluid [Günther et al. (2004)].

1.3 Quantum Dot/Semiconductor overview

This thesis work is focused on microfluidics as applied to particle self-assembly. By way of background, a short description of the particle systems of interest is provided in this section with more detailed information available elsewhere [Cohen and Chelikowsky (1988); Wolfe et al. (1989); Brus (1991)].

Materials can be categorized into three groups based on their ability to conduct electricity; conductors, semiconductors and insulators. A conductor is a material that readily conducts an electric current whereas an insulator is one that does not. A semiconductor lies between these two extremes and can behave as both a conductor and an insulator.

Electrons in atoms occupy different energy states known as energy levels with a maximum of two electrons in an energy level at any given time [Wolfe et al. (1989)]. Energy levels separated by insignificant amounts of energy are further grouped together into energy bands. In materials composed of a large number of atoms, the difference in energy between energy levels in an energy band is so small that it is often considered negligible and the energy levels are said to be continuous [Wolfe et al. (1989)]. The two energy bands most important to semiconductor physics are the valence and conduction bands. The valence band is the outermost energy band occupied by electrons in a material at 0 K and the conduction band is the energy band just above the valence band where electrons are freely mobile and can conduct an electric current [Wolfe et al. (1989)]. In conductors, the valence and conduction bands of a material overlap and electrons can freely enter the conduction band [Cohen and Chelikowsky (1988)]. In

semiconductors and insulators, there exists a region between the valence and conduction bands where no electrons can exist, known as the band-gap. In insulators, the energy required for an electron to traverse the band-gap (band-gap energy) is sufficiently large that no free electrons exist in the conduction band. In a semiconductor, under certain stimulus such as an applied voltage, heat or electromagnetic radiation, electrons may be excited into the conduction band [Wolfe et al. (1989)]. In a semiconductor, when an excited electron returns to the valence band it may release a photon with a wavelength corresponding to the band-gap energy. A schematic illustrating the band structures of conductors, insulators and semiconductors is provided in Figure 1.6.

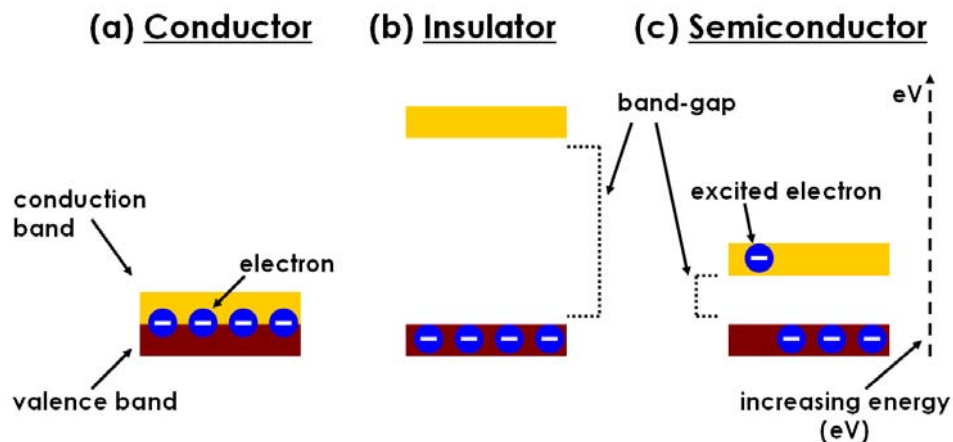


Figure 1.6: Schematic illustrating spacing of the conduction and valence energy bands for a (a) conductor, (b) insulator and (c) semiconductor [Cohen and Chelikowsky (1988)].

Quantum Dots are semiconductor nanoparticles (usually 1-10 nm in diameter [Pinaud et al. (2006)]) with unique optical (band-gap) properties when compared to bulk semiconductor materials [Krishnadasan et al. (2004)]. Specifically, when a semiconductor's particle radius is smaller than its exciton Bohr radius the energy levels

in the valence and conduction bands are no longer continuous but discrete [Hu et al. (1990); Brus (1991); Chan et al. (2002)] meaning that the difference in energy between them is significant. The small size of a QD puts them in this regime. In this regime, the band-gap energy and emission wavelength of the QD is a function of the size of the particle [Kan et al. (2004)]. Thus, by controlling the size of the QD during synthesis, the resulting emission wavelength of the QD can be tuned to emit light at a variety of frequencies. Quantum dots have a number of other beneficial characteristics including high quantum yield (ratio of emitted to absorbed photons) [Chen and Rosenzweig (2000)], excellent photostability, broad absorption cross-sections and long fluorescence lifetimes (>10 ns) [Pinaud et al. (2006)]. These appealing characteristics have made QDs an appealing material for use in fluorescent bio-labels [Wang and Moffitt (2004)], lasers [Marsh et al. (2000)], light emitting diodes (LEDs) [Park et al. (2001)], solar cells [Nozik (2002)] and logical elements for quantum computation [Loss and DiVincenzo (1998)]. Quantum dots are often composed from group II-VI (e.g. CdS, CdSe and ZnSe) or III-V (e.g. InAs and InP) elements in the periodic table [Chan et al. (2002)]. A schematic of the energy bands and energy levels in a QD when compared to bulk semiconductors is provided in Figure 1.7.

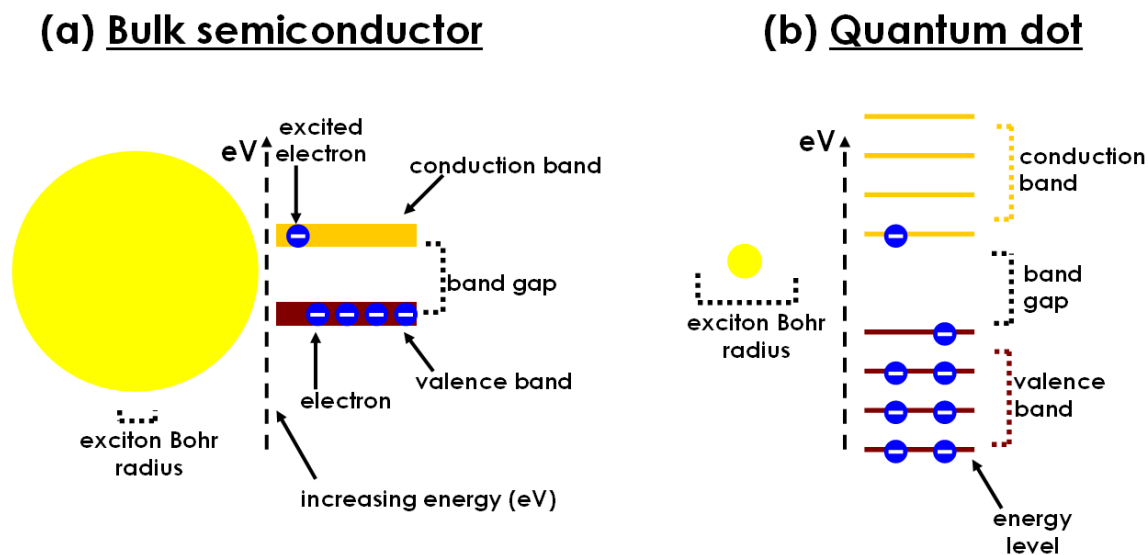


Figure 1.7: Energy band/band-gap structure schematics for (a) a large semiconductor particle and (b) a quantum dot. In (a), the particle radius is much larger than its exciton Bohr radius and the energy levels are separated by an insignificant amount of energy. The band-gap energy remains constant for increasing particle size. In (b), the particle radius is smaller than the exciton Bohr radius and the energy levels in each energy band are discrete and separated by a significant amount of energy. Slight modifications to the size of the quantum dot can significantly alter the energy level spacing and band-gap energy [Brus (1991)].

1.4 QDCM Self-Assembly Overview

It is well established that diblock copolymers (block copolymers with two chains) self-assemble into micelles or aggregates when exposed to a solvent that is a thermodynamically favorable solvent for one block but not the other [Malmsten and Lindman (1992); Gao and Eisenberg (1993); Zhang et al. (1997); Zhang and Eisenberg (1999); Yusuf et al. (2007a)]. The thermodynamically unstable block strives to minimize its unfavorable interaction with the solvent by self-assembling into micelles which consist of a core of the insoluble blocks surrounded by a corona of the soluble blocks

[Zhang et al. (1997)]. In the case of amphiphilic diblock copolymers where one block is hydrophilic and the other hydrophobic, two possible classes of micelles can form. Micelles formed in an organic solvent will contain a hydrophilic core and a hydrophobic corona and are termed reverse micelles. Micelles formed in an aqueous media will contain a hydrophobic core and a hydrophilic corona and are termed regular micelles [Zhang et al. (1997)]. Micelles are also classified based on the respective sizes of their corona and core forming blocks. Micelles with a large corona and a small core are termed ‘star-like’ and those with a large core and small corona are termed ‘crew-cut’ [Zhang et al. (1997)]. A schematic showing these four classifications of micelles is shown in Figure 1.8.

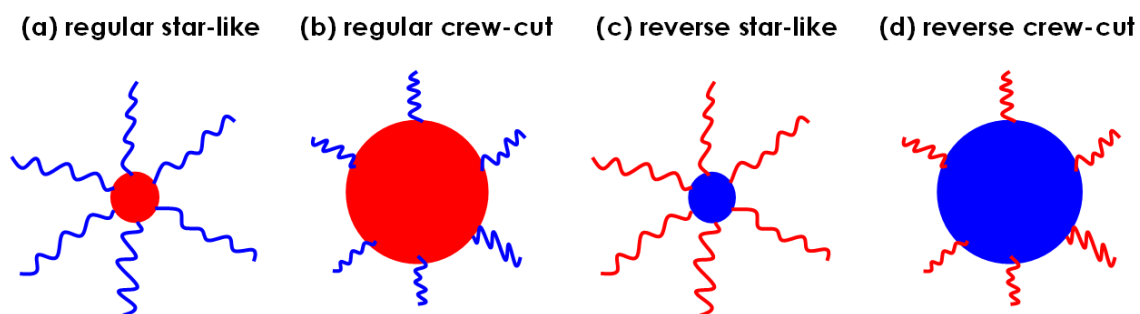


Figure 1.8: Schematic showing different classifications of micelles assembled from diblock copolymers. (a) Star-like and (b) crew cut regular micelles with a hydrophobic core and hydrophilic corona. (c) Star-like and (d) crew-cut reverse micelles with a hydrophobic corona and hydrophilic core.

Block copolymer-stabilized CdS QDs with an external PS brush layer (PS-CdS) and PS-*b*-PAA block copolymer stabilizing chains co-dissolved in dimethylformamide (DMF) organize into QDCMs upon the addition of water above a critical water concentration (cwc ~1-2 wt%) [Yusuf et al. (2007a)]. Self-assembly is driven by phase

separation of PS chains of PS-CdS and PS-*b*-PAA from solution [Eisenberg et al. (1997)], with the PAA chains of the latter component stabilizing the surface of the assemblies in the increasingly hydrophilic DMF/water mixture. With further water addition above the *cwc*, interfacial tension drives continued particle growth. However, increasing water concentration also decreases the mobility of the PS chains as the DMF is progressively leached out of the QDCMs, and when the water concentration reaches ~8-11 wt%, the QDCMs become kinetically frozen meaning they can no longer grow [Yusuf et al. (2007a)]. The basic structures of the PS-CdS QDs, PS-*b*-PAA block copolymer stabilizing chains and QDCMs are shown in Figure 1.9.

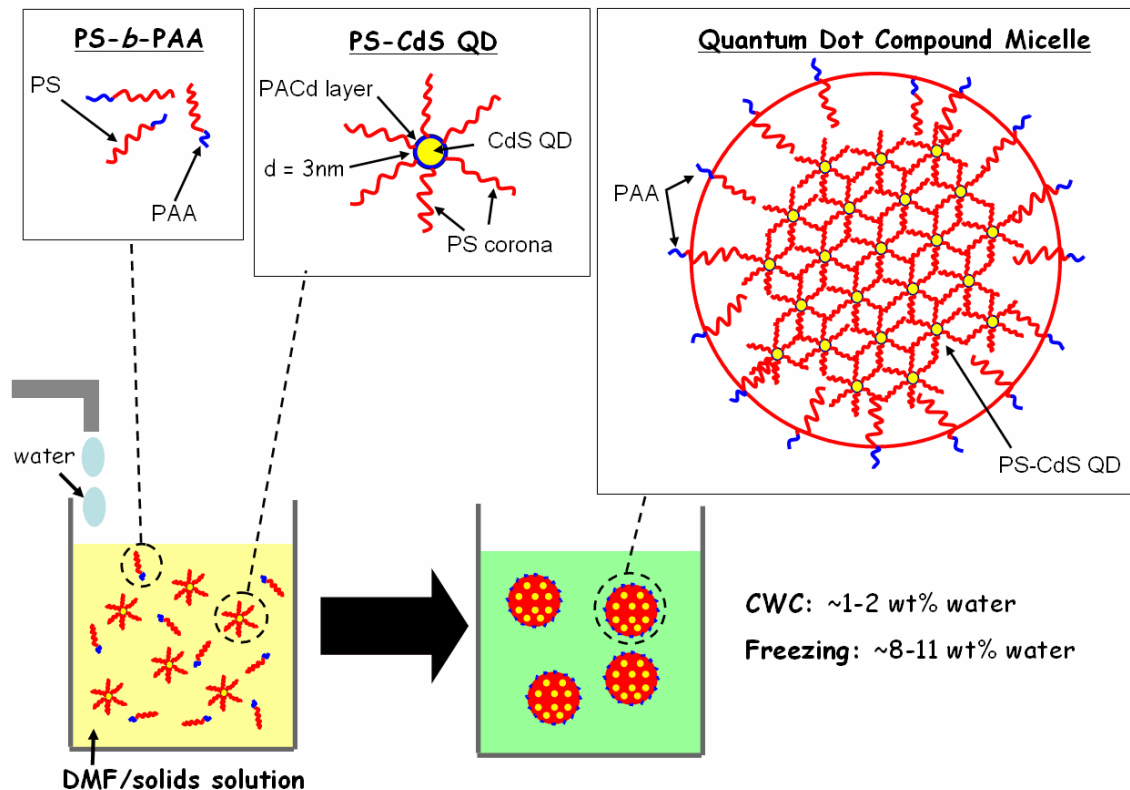


Figure 1.9: Illustration of the QDCM self-assembly process from PS-CdS QDs and PS-*b*-PAA block copolymer stabilizing chains with the addition of water. The PS-*b*-PAA and PS-CdS constituents agglomerate and form QDCMs when the water concentration in the DMF/solids solution exceeds the CWC ($\sim 1\text{-}2\text{ wt\%}$). When the water concentration reaches the freezing point ($\sim 8\text{-}11\text{ wt\%}$), the QDCMs become kinetically frozen and can no longer grow.

Quantum dot compound micelles consist of an inner cluster of CdS QDs encased in an outer layer of PS-*b*-PAA block copolymers [Yusuf et al. (2007a)]. The outer layer of PS-*b*-PAA block copolymers is oriented so that the hydrophilic PAA tails constitute the outer corona of the QDCM. Due to their complex structural hierarchy, QDCMs are promising colloidal elements for applications in biological labeling, diagnostics, and photonics [Wang and Moffitt (2004)]; for these various applications, control of QDCM size and polydispersity is a critical issue.

Previous methodologies for producing QDCMs include the drop-wise addition of water to a blend solution of CdS QDs and PS-*b*-PAA chains dissolved in DMF [Yusuf et al. (2007a)]. Using this technique, results showed that kinetic QDCM size control can be imposed by adjusting the initial polymer concentration or the rate of drop-wise water addition; both of these factors influence the window of growth between the cwc and the freezing point, allowing QDCM sizes and polydispersities to be tuned. Specifically, it was found that as the initial polymer concentration of blends of PS-CdS and PS-*b*-PAA in DMF is increased from 0.5 to 3 wt%, the mean particle diameter of the QDCMs formed increases from 50 to 209 nm [Yusuf et al. (2007a)]. Increasing the rate of water addition played a less significant role as the mean particle diameter of the QDCMs formed decreases by only 12 nm when the rate of water addition is increased from 0.4 to 4.8 wt%/min [Yusuf et al. (2007a)]. A limitation of this method of QDCM self-assembly was that it did not provide a means for controlling particle polydispersity which was relatively high with QDCM populations exhibiting standard deviations between 18-30% of their respective mean diameters [Yusuf et al. (2007a)]. Also, it was not possible to study the influence of water concentration on particle growth in isolation from growth time. New methods of size control based on microfluidics could take advantage of the relatively small length scales of water diffusion to provide better tuning of size and polydispersity of QDCMs, as well as insights into the QDCM formation process.

1.5 Methodology

1.5.1 Microfabrication

The first microfluidic devices were developed in the 1970's and were fabricated out of silicon and glass using photolithography and etching. These processes were both time consuming and expensive, often requiring the use of a clean room for fabrication. More recently, new techniques have been developed for the fabrication of microfluidic devices from soft polymeric materials [Kamholz (2004)]. One such technique, very popular among researchers, is known as soft lithography. Soft lithography is a more appealing technique for microfabrication than the etching of glass and silicon because the materials and equipment required are far less expensive and the entire process can be completed in as little as one day [Duffy et al. (1998); McDonald et al. (2000)]. It is a two stage process: the first stage involves rapid prototyping and the second stage involves replica molding [McDonald et al. (2000)].

1.5.1.1 Rapid Prototyping

Rapid prototyping is a two-step process used to fabricate a negative master of the final microfluidic chip. The first step is the design of the microfluidic channel network using a computer-aided design program (CAD). These CAD designs are called photomasks and a picture of a photomask for a simple microfluidic focuser is shown in Figure 1.10. The second step is the fabrication of a negative master of the microchannel

using photolithography. Photolithography is a process whereby a two-dimensional geometric pattern is transferred into photoresist through light exposure. A photoresist is a light sensitive chemical whose physical properties are altered when exposed to light at a specific frequency. The photoresist is usually deposited as a thin film of uniform thickness onto a flat substrate before exposure. After exposure, the photoresist is placed in a developer solution which removes either the exposed or unexposed portions. Two classes of photoresist exist. A positive-tone photoresist is degraded after exposure and dissolves during development. A negative-tone photoresist is cross-linked during exposure and becomes insoluble in its developer solution. Photoresists are commonly used in microfabrication processes because it is possible to pattern and reproduce micron to nano sized features in these materials [Microchem (2002a)].

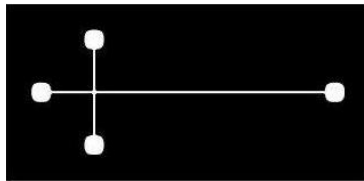


Figure 1.10: An example of a photomask used to produce a simple microfluidic focuser using negative-tone photoresist.

The photoresist used in this work was a negative-toned photoresist called SU-8 (Microchem, MA). SU-8 is an epoxy based photoresist that is chemically, thermally and structurally stable and is ideally suited for applications where the cured photoresist is to become part of the final device, or for molding [Microchem (2002b)]. It is sensitive to light in the ultraviolet (UV) spectrum (350–400 nm). SU-8 films with a thickness ranging from 2 μm to 2 mm can be deposited on a substrate and channel features with

widths as small as 10 μm can be patterned making it suitable for a range of microfluidic applications.

The steps involved in the fabrication of an SU-8 structure are shown schematically in Figure 1.11. The steps are described as follows: an SU-8 film of uniform thickness is deposited onto a flat substrate using a spin coater; the substrate is heated to allow the solvents to evaporate; the substrate is cooled to room temperature to allow the SU-8 film to harden; a photomask is placed over the SU-8 film and the substrate is exposed to UV light; the substrate is again heated to selectively cross-link the exposed portions of the film, improving structural rigidity and adhesion to the substrate; the assembly is cooled to room temperature; and finally, the device is placed in SU-8 developer (4-hydroxyl-4-methyl-2-pentanone) that removes the unexposed SU-8.

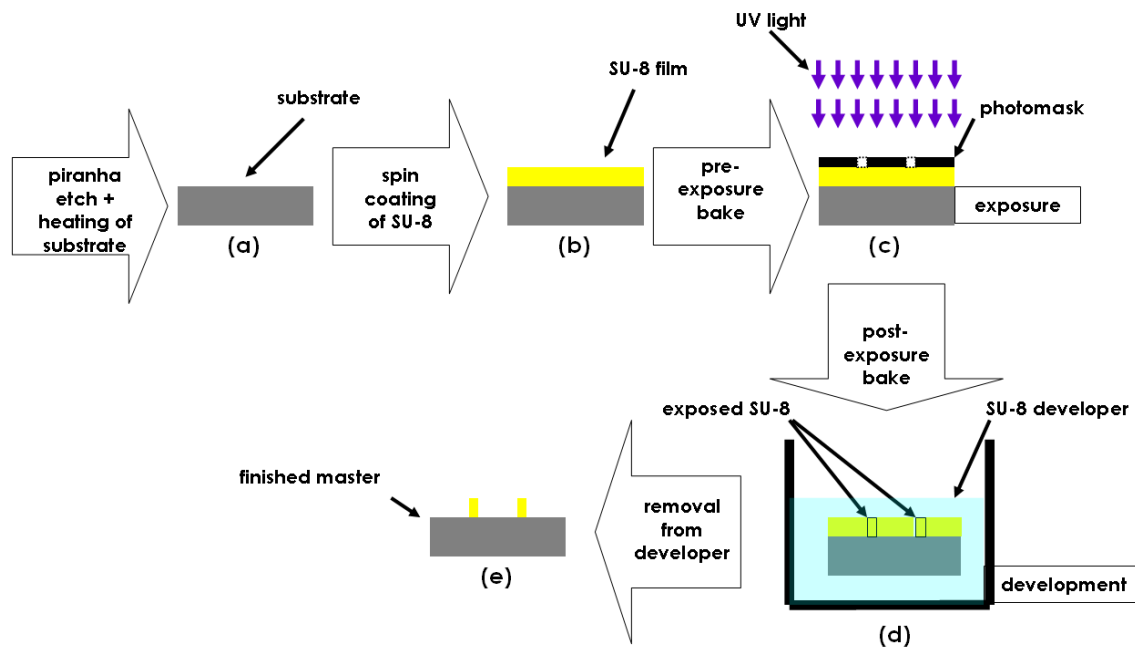


Figure 1.11: Fabrication of a negative master of a microfluidic chip using photolithography. A cross-sectional schematic of the device is shown at various stages in the process; (a) after cleaning and drying of substrate; (b) after spin coating SU-8 onto the substrate, (c) during exposure to UV light; (d) during development and (e) when the process is finished.

1.5.1.2 Replica Molding

Replica molding is a simple process whereby a polymer is cast onto the negative master fabricated during rapid prototyping. In this work, a polymer called poly(dimethylsiloxane) (PDMS) was used as the molding agent. PDMS has many qualities that make it appealing for use in microfluidics. It is an inexpensive material which can reproduce features very well on the micron scale; it is optically transparent down to 280 nm, cures at low temperatures, is non-toxic and can be sealed reversibly or irreversibly to many materials [McDonald et al. (2000)]. It is also resistant to water and

many organic solvents, however, PDMS absorption and subsequent swelling can occur with some solvents [Lee et al. (2003)].

PDMS forms a weak reversible seal to glass provided by simple Van der Waals bonding. Although watertight, this seal cannot generally withstand pressures greater 5 psi [McDonald et al. (2002)] and is not sufficient for most microfluidic applications. A stronger irreversible seal can be created by treating PDMS with oxygen plasma. This treatment is believed to generate silanol groups (Si-OH) on the surface of the PDMS by the oxidization of methyl groups [Owen et al. (1994)]. Surface oxidized PDMS forms a strong irreversible seal via covalent bonding. PDMS can be permanently sealed to a variety of substrates in this manner including itself and glass. Oxygen plasma treatment has a side-effect of altering the surface of the PDMS rendering it hydrophilic [Ng et al. (2002)]. Over time, the PDMS reverts back to its original state, and as such, its surface properties can be tuned to accommodate different applications. Figure 1.12 outlines the replica molding and sealing procedure and images of the different components fabricated during the microfabrication process are shown in Figure 1.13.

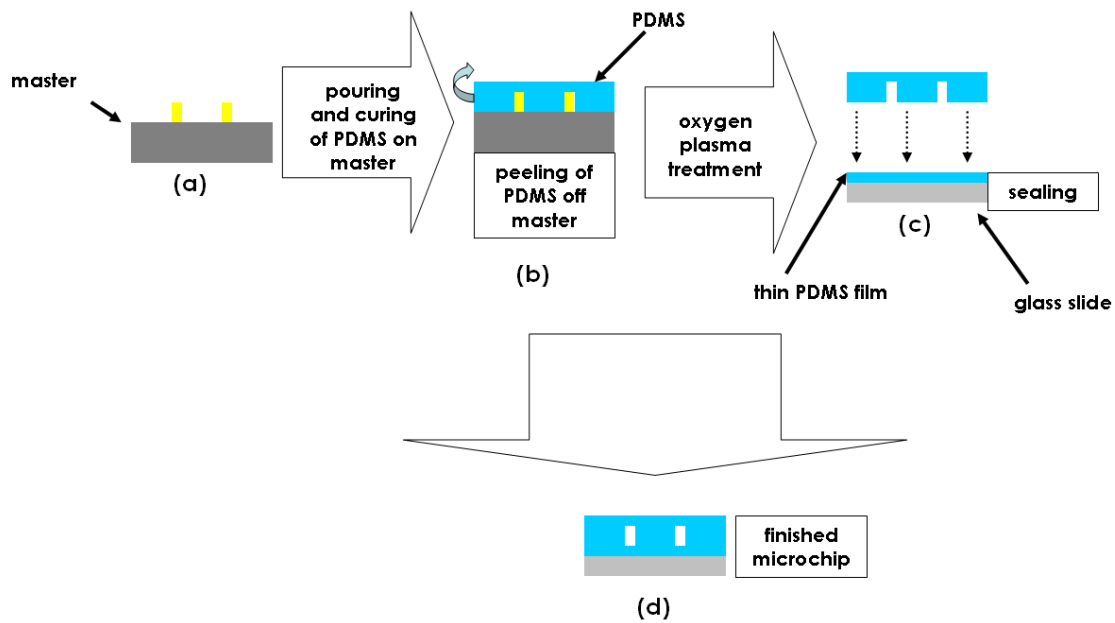


Figure 1.12: A cross-sectional schematic of the microchip during the replica molding and sealing process at different stages of fabrication: (a) prior to pouring of PDMS onto the negative SU-8 master; (b) after pouring and curing of PDMS; (c) the PDMS microchip and a glass slide with a thin layer of cured PDMS are exposed to oxygen plasma for 30 seconds and then sealed to one another; (d) the final microchip ready for experimental use.

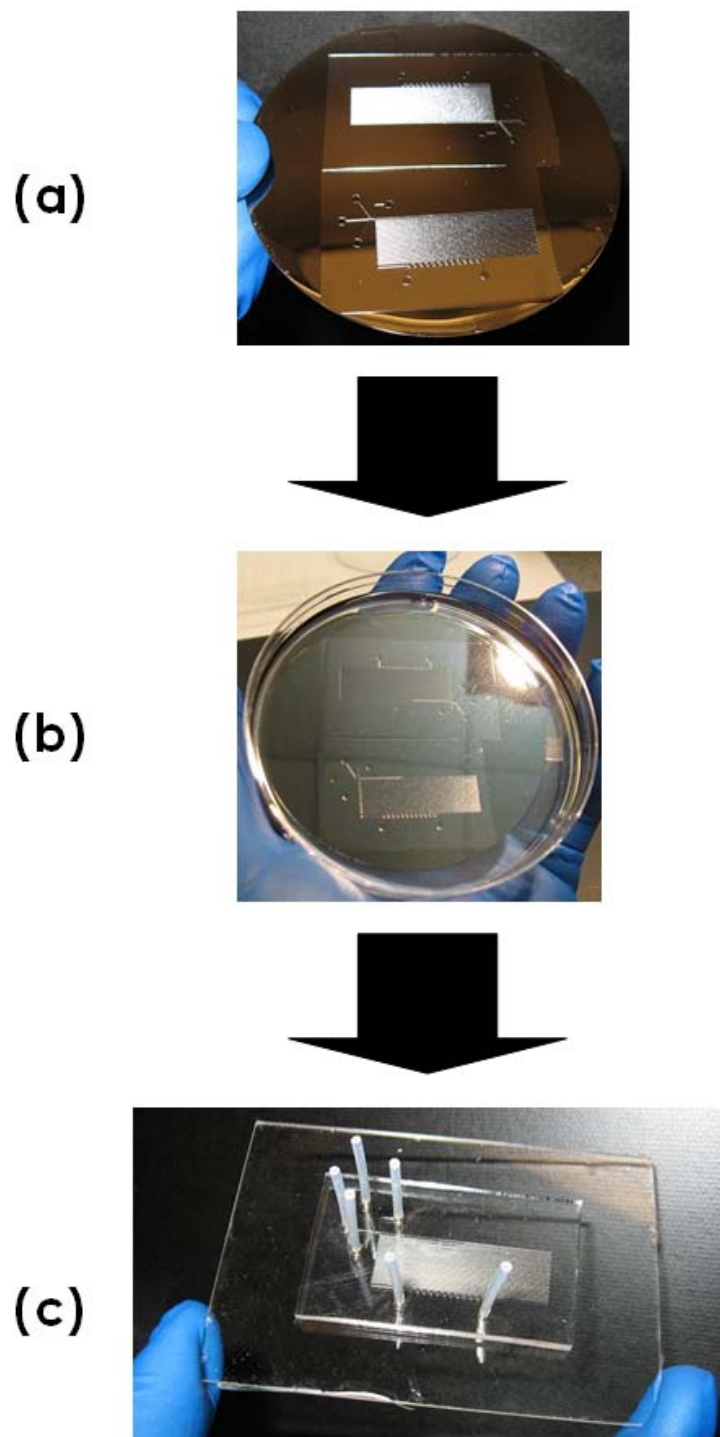


Figure 1.13: Pictures of finished products at different stages of the microfabrication process: (a) finished negative SU-8 master on a silicon wafer; (b) silicon wafer in petri dish submerged in cured PDMS; and (c) cut-out and sealed PDMS microchip ready for use.

1.5.2 Experimental Methods

1.5.2.1 Fluorescence Microscopy

Fluorescence microscopy is a visualization technique commonly used in biology to visualize the components of cells [Johnson et al. (1981)]. More recently, fluorescence microscopy has been widely used in microfluidics for direct visualization of microfluidic processes involving the mixing of multiple streams [Biddiss et al. (2004)] and dispensing [Jacobsen et al. (1998); Sinton et al. (2003)]. Fluorescence is an optical phenomenon which occurs when molecules excited by electromagnetic radiation almost immediately emit a photon [Sinton (2004)]. When a fluorescent molecule absorbs light at a high enough frequency it enters an excited state. The energy from the absorbed photons excites some electrons in the valence band of the fluorescent molecule into its conduction band. After a very brief moment, typically 1-10 ns, the fluorescent molecule returns to its ground state. The excited electrons return to the valence band, releasing energy in the form of emitted photons as they enter this lower energy state. During this process, some of the energy of the absorbed light is dissipated through interactions with other molecules and conformational changes and the emitted photon is of lower energy and higher wavelength [Periasamy and Day (2005)]. The difference in wavelength between the absorbed and emitted photon is termed the Stokes shift and is different for different fluorescent particles.

Two fluorescent particles were used in this work; the CdS QDs and a fluorescent dye, fluorescein. Fluorescent light from the CdS QDs provided a means for the

visualization of the on-chip QDCM self-assembly process. Fluorescent light from the fluorescein provided visual data and a quantitative means of measuring the mixing between water and DMF inside a microfluidic reactor. The absorption and emission spectrums for CdS QDs and fluorescein are shown in Figures 1.14 and 1.15 respectively.

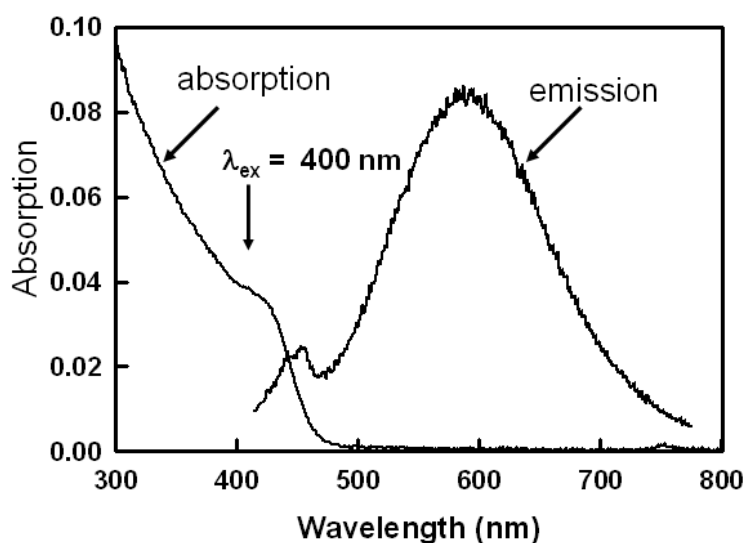


Figure 1.14: The absorption and emission spectra of PS-CdS QDs. The emission spectrum was obtained using an excitation wavelength of 400 nm [Yusuf et al. (2007a)].

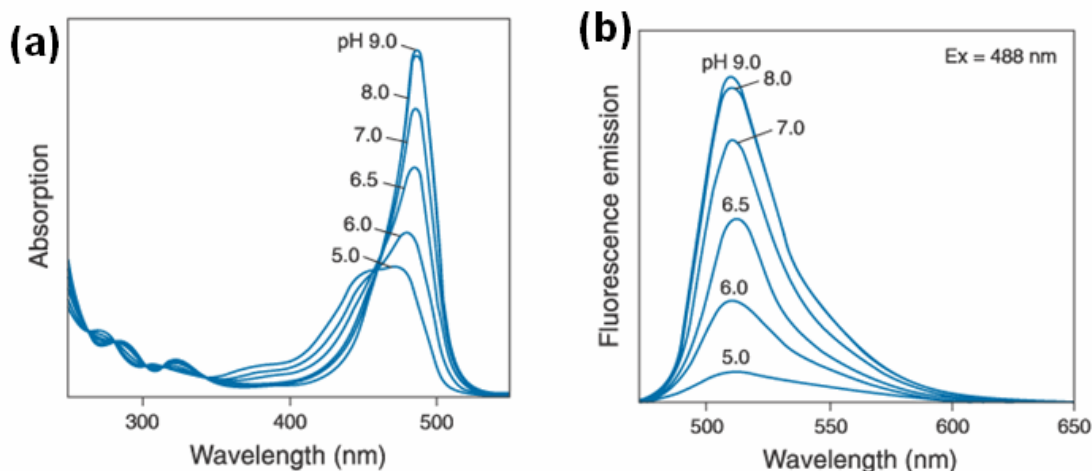


Figure 1.15: (a) Absorption and (b) emission spectrum of fluorescein dissolved in solution at different pH (Invitrogen Inc, ON).

1.5.2.2 Working Solutions and Materials

The working fluids in all cases were an organic solvent, DMF (99.9+ % HPLC Grade, H₂O < 0.03%), 99.9% pure de-ionized water, a low viscosity oil, perfluorodecalin (PFD) (Acros Organics, NJ) and a surfactant, 1H,1H,2H,2H-perfluorooctanol (Acros Organics, NJ).

The CdS QDs used in this work were supplied by the collaborating research group (Moffitt Lab, UVic Chemistry). Only a short description is included here. Block copolymer-stabilized CdS QDs with an external PS brush layer (PS-CdS) were synthesized via self-assembly of a PS-*b*-PAA block copolymer to form reverse micelles in a hydrophobic solvent, followed by templated CdS QD synthesis in the micelle cores. The designation PS-CdS refers to the average degree of polymerization of PS blocks (~300 styrene units) surrounding each CdS QD core. Static and dynamic light scattering results reveal that each stable PS-CdS particle is surrounded by an average of 54 ± 2

copolymer chains (kinetically frozen at the QD surface by the high T_g of the poly(cadmium acrylate), PACd, surface layer), and has a z -average hydrodynamic diameter of $d_h = 36 \pm 2$ nm. Further details on the synthesis and characterization of PS-CdS can be found in Yusuf et al. (2007a). The second constituent for QDCM formation, PS(665)-*b*-PAA(68) stabilizing chains, were synthesized via anionic polymerization of the associated polystyrene-*block*-poly(*tert*-butyl acrylate) block copolymer, followed by hydrolysis of the ester block; numbers in brackets refer to number-average degrees of polymerization of each block [Yusuf et al. (2007a)].

For microfluidic self-assembly experiments, PS-CdS and PS(665)-*b*-PAA(68) were dispersed separately in DMF; the solution of stabilizing chains and dispersion of PS-CdS were then combined to form a 50/50 (w/w) blend of constituents in DMF. DMF/water mixtures were created by adding 99.9% pure de-ionized water to DMF on a digital balance (Denver Instrument, CO). A fluorescein solution was created by dissolving fluorescein powder (Invitrogen Inc., ON) in water at a concentration of 2 mM.

1.5.2.3 Experimental Apparatus

Fluids were driven into microchannel inlets using gastight syringes (Hamilton, NV) mounted on syringe pumps (Harvard Apparatus, QU). Teflon tubing (Scientific Products and Equipment, ON) with a 1/16th inch OD connected the syringes to the inlets of the microchannels. Holes with a slightly smaller diameter than the tubing were punched through the inlets and outlet of the microchannels and the tubing was inserted. The elasticity of the PDMS provided a seal between the chip and the tubing.

Microchannels were observed on an inverted microscope (DMI 6000B, LEICA, NJ). Images were captured using a charge-coupled device (CCD) camera (Orca AG, Hamamatsu, NJ) installed on the microscope. A picture of the experimental apparatus is shown in Figure 1.16.

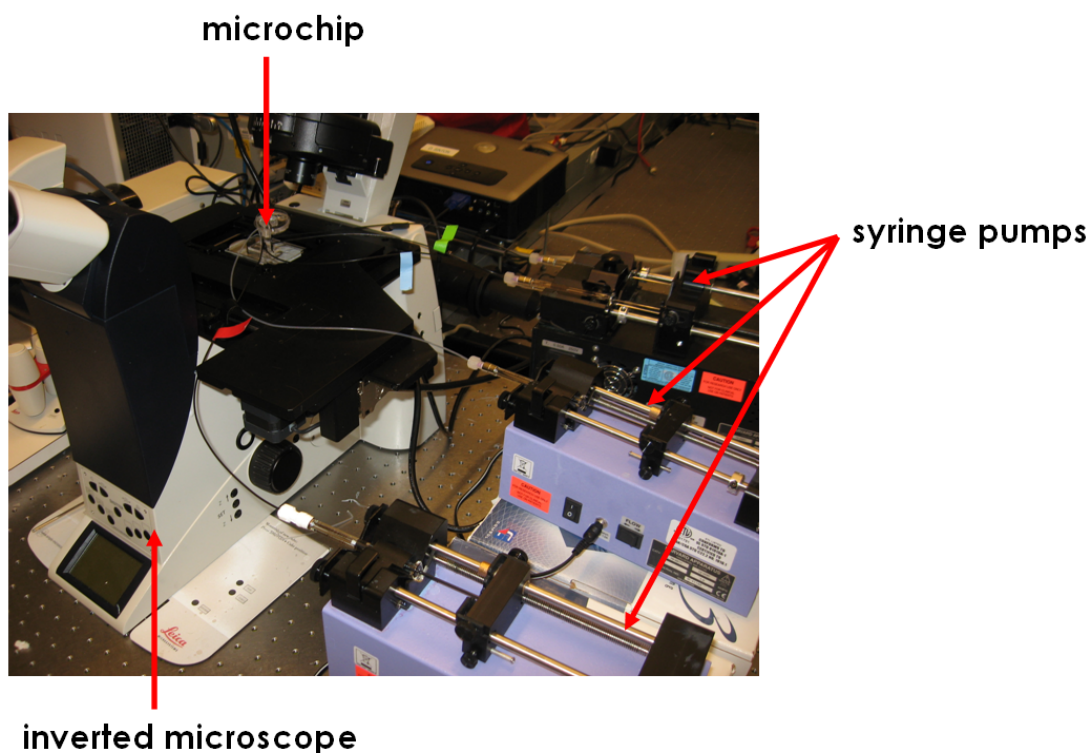


Figure 1.16: The experimental apparatus used in this work. The microchip from Figure 1.13c is mounted on the DMI 6000B microscope (left) connected via teflon tubing to the gastight syringes mounted on syringe pumps (right).

Fluorescence filter cubes (Semrock, NY) installed on the microscope were used to capture the fluorescent light emitted from inside the microchannels onto the CCD camera. A filter cube only transmits light at the fluorescent molecule's excitation wavelength to the microscope stage and only allows the light emitted by the fluorescent

molecule to reach the CCD camera. The operating principles of a fluorescence filter cube are shown in Figure 1.17.

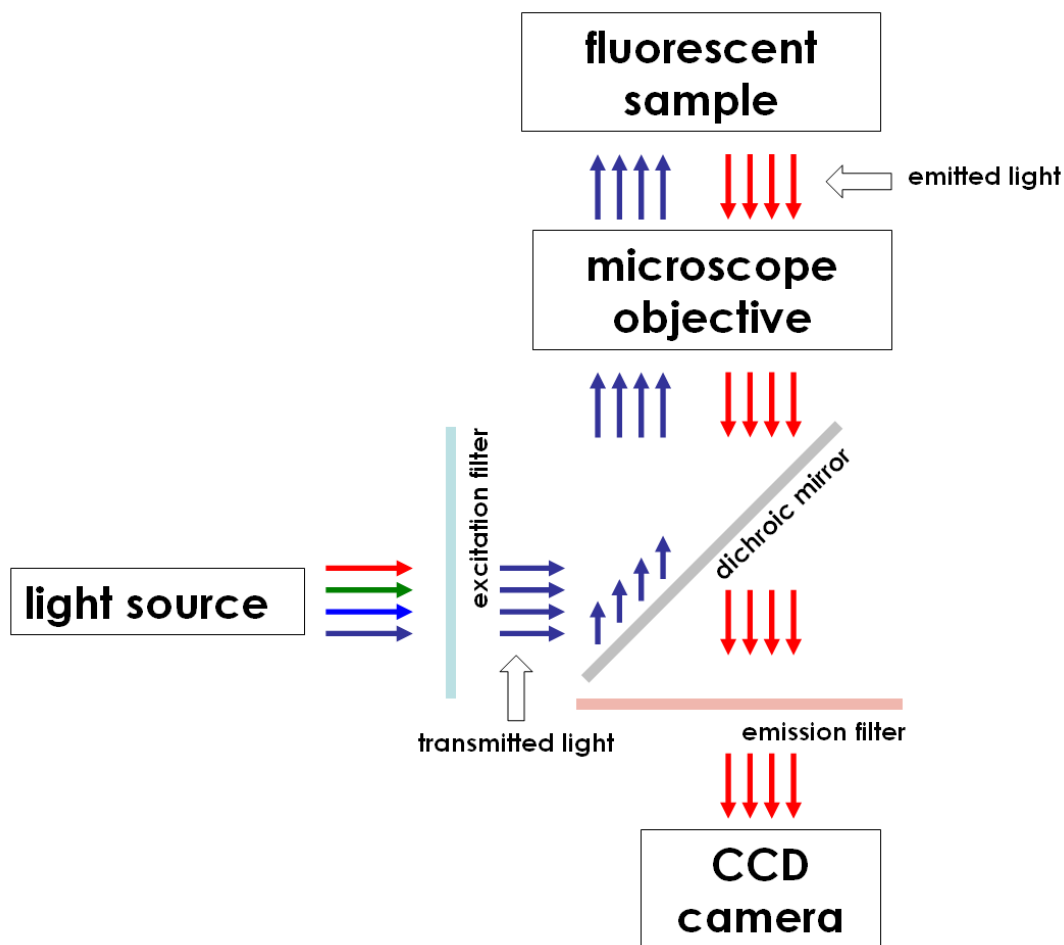


Figure 1.17: Schematic illustrating the operating principles of a fluorescence filter cube. The filter cube consists of two perpendicular filters, the excitation and emission filters with a dichroic mirror positioned in between them at a 45° angle. The excitation and emission filters block all light from passing except that which is in the excitation and emission wavelength range of the fluorescent particle respectively. The dichroic mirror reflects the shorter wavelength excitation light but is transparent to the longer wavelength emission light. The excitation light passes through the excitation filter and is reflected upwards by the dichroic mirror and then passes into the microscope objective before impinging on the sample. After undergoing the Stokes shift, the light is re-emitted at a longer wavelength. This emitted light travels downward and passes through the dichroic mirror and the emission filter before reaching the CCD camera.

1.5.2.4 Fluorescence Image Processing

Fluorescence images taken with a CCD camera can include non-uniformities in intensity due to a non-uniform distribution of the excitation light, ambient lighting and curved surfaces within the channel [Inoue and Spring (1997)]. These non-uniformities are a product of the imaging process and distort the actual emitted light. Image normalization is employed to remove these non-uniformities. Normalized images are generated by combining the images in a microchannel running at steady-state conditions (raw image, I_{raw}) with images where the fluorescent species (bright image, I_{bright}) flows alone in the reactor and similarly for the non-fluorescent species (dark image, I_{dark}) using the formula below.

$$I_{normalized} = \frac{I_{raw} - I_{dark}}{I_{bright} - I_{dark}} \quad (1.10)$$

Normalized images facilitate a means for comparing the light intensity of the CdS QDs before, during and after the on-chip QDCM self-assembly process. A normalized intensity value of 1 represents the base-case QD fluorescence prior to self-assembly. Normalized images are also generated for fluorescein such that light intensity may be correlated with species concentration. In this case, a normalized value of 1 represents a region with the original concentration of fluorescent species and 0 a region devoid of the fluorescent species.

1.5.2.5 Transmission Electron Microscopy (TEM)

Transmission Electron Microscopy (TEM) is an imaging technique where a beam of electrons is transmitted through a sample, obtaining information on its inner structure which is then magnified by a series of electromagnetic lenses and recorded by hitting a fluorescent screen, photographic plate or light sensitive sensor such as a CCD camera [Reimer (1989)]. For this work, The Moffitt Group (UVic Chemistry) provided TEM images of the various aqueous QDCM samples using a Hitachi H-700 electron microscope. The diameters of individual QDCMs could be measured from TEM Images, providing a means for conducting a statistical analysis on the size distributions of QDCMs formed in different local environments.

1.6 Overview of this thesis

The specific contributions of this thesis are outlined below:

In Chapter 1, the aims and motivation of this work were presented. Next an overview of basic microfluidic transport phenomena such as pressure driven flow, diffusion and multiphase flow was presented as well as overviews of semiconductor and quantum dot physics and block-copolymer self-assembly. Finally, the microfabrication procedure and experimental methodologies used for this work were described.

In Chapter 2, microfluidic techniques for the self-assembly of QDCMs in continuous, sheath-flow microfluidic reactors are described. Two types of microfluidic reactors are developed: the first is a microfluidic T-sensor designed for on-chip

fluorescence analysis of QDCM formation and the second is a two stage flow-focusing reactor designed to control the growth of QDCMs by varying key controlling parameters such as flowrates and water concentration. An overview of the experimental methodologies used for both reactors is provided and the results obtained from on-chip fluorescence microscopy and off-chip TEM imaging are analyzed.

In Chapter 3, microfluidic techniques for the self-assembly of QDCMs in multiphase microfluidic reactors are described. This use of multiphase microfluidics represents a first for the University of Victoria Microfluidics Lab. Combining multistep processing and multiphase flow, the chips developed through this chapter are the most complex chips developed in the lab to date. Two types of multiphase microfluidic reactors are developed: the first is a multiphase droplet reactor and the second is a multiphase gas-liquid reactor. The experimental and physical challenges associated with both reactors are described and the results obtained from on-chip fluorescence microscopy and off-chip TEM imaging are analyzed.

In Chapter 4, a brief overview of the key contributions of this thesis is provided and a summary of future work stemming from these findings is proposed.

Chapter 2

QDCM SELF-ASSEMBLY IN SHEATH-FLOW MICROFLUIDIC REACTORS

2.1 Introduction

In this chapter, two continuous flow microfluidic strategies for the self-assembly of quantum dot compound micelles (QDCMs) are developed and tested. Background on the pertinent microfluidic phenomena, methodologies and the colloid system of interest was provided in Chapter 1. The focus of the present chapter is the development of the sheath-flow microfluidic reactors, testing and analysis of the results.

The two microfluidic strategies investigated in this chapter involve combining a stream of DMF containing dissolved PS-CdS QDs and PS-*b*-PAA stabilizing chains (DMF/solids stream) with a second stream composed of a mixture of DMF and water (DMF/solids stream). The combination of one laminar stream with another is commonly called a sheath-flow. The streams mix via cross-stream diffusion, and in this case, the

stream containing water penetrates into the DMF/solids stream. Once the local water concentration exceeds the *cwc*, QDCM formation is expected. In the first strategy, the constituents for QDCM formation were combined in the most basic microfluidic geometry; a wide microfluidic T-sensor (as shown in Figure 1.3a). In the second strategy, the constituents were introduced into a two stage flow-focusing microfluidic reactor (a microfluidic focusing geometry is shown in Figure 1.3b). At the first focusing stage, sufficient water is focused into the DMF/solids stream to exceed the *cwc* and initiate QDCM formation. At the second focusing stage, additional water is introduced into the system to kinetically freeze (quench) the QDCMs. The two focusing stages are separated by a long channel that provides sufficient time for the streams from the first focusing stage to fully mix and additional time for QDCMs to grow prior to quenching.

Microfluidic T-sensors and focusers are two of the most common microfluidic passive mixer configurations and have been used for many different applications including chemical synthesis [Jahn et al. (2004)], immunoassays [Hatch et al. (2001)], particle separation [Weigl and Yager (1999)], pH measurements [Galambos et al. (1997)], protein analysis [Hertzog et al. (2006)] and microfluidic fuel cells [Bazylak et al. (2004)]. The mixing characteristics of a microfluidic T-sensor have been investigated in a number of studies [Kamholz et al. (1999); Gobby et al. (2000); Hatch et al. (2004); Munson et al. (2005)]. Mixing in both a microfluidic T-sensor and focuser is diffusion dominated making them well suited for investigating the rates of chemical reactions [Hatch et al. (2004)]. For applications where enhanced mixing is desired, microfluidic T-sensors and focusers have been modified by adding grooves [Nguyen and Wu (2006)] or

heterogeneous surface patches [Erickson and Li (2001)] to the mixing channel in order to increase mixing rates.

In this chapter it is demonstrated that these two continuous sheath-flow microfluidic reactors provide both a means to control the average sizes of QDCMs, as well as a means to observe the self-assembly process on-chip. The analytical basis for the sheath-flow microfluidic reactors is presented, followed by specifics of the methodologies employed. The self-assembly of QDCMs in these reactors is then analyzed using fluorescence microscopy. An off-chip statistical analysis of QDCM populations formed under different operating conditions in the flow-focusing reactor is carried out using transmission electron microscopy (TEM).

2.2 Analytical Analysis of Sheath-Flow Mixing

An analysis of diffusion inside T-sensor and focuser microfluidic systems was performed prior to the finalization of reactor designs. Calculations of the mixing rates inside these systems provided information on the geometric and parametric channel requirements necessary to facilitate on-chip self-assembly of QDCMs. Downstream predictions of the cross-stream water concentration were obtained for a T-sensor using the one-dimensional diffusion equation [Probstein (1994)] shown below:

$$u \frac{\partial c_w(z, x)}{\partial x} = \wp \frac{\partial^2 c_w(z, x)}{\partial z^2} \quad (2.1)$$

Here, c_w is the water concentration, \wp is the diffusion coefficient, z is the cross-stream position vector, x is the downstream position vector and u is the downstream velocity.

2.2.1 Diffusion in a Microfluidic T-Sensor

Analytical predictions of the diffusion rates in a T-sensor were carried out in order to inform the microfluidic chip design and running conditions to be employed. Specifically, it was important to insure that the diffusion time-scales were large enough to allow for the QDCM self-assembly process to be monitored at multiple locations downstream. A solution for $c_w(z,x)$ for a geometry that closely resembles the T-sensor can be derived from Equation 2.1 using the Laplace transform with the following boundary conditions [Bird et al. (1960)]:

$$\begin{aligned}
 c_w(z > 0, 0) &= 0 \\
 c_w(0, x \geq 0) &= \frac{1}{2}c_0 \\
 c_w(z \rightarrow \infty, x \geq 0) &= 0
 \end{aligned}
 \tag{2.2}$$

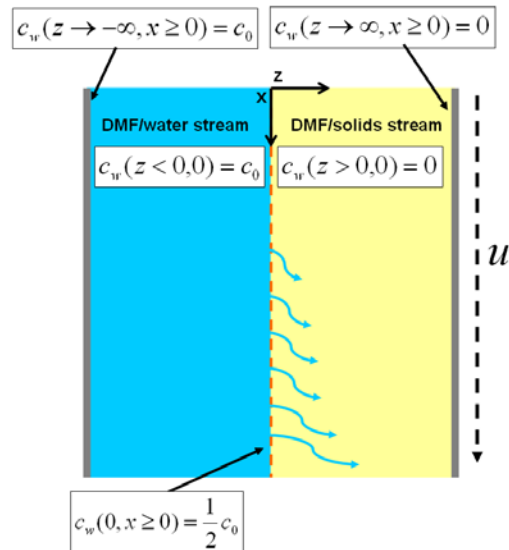


Figure 2.1: Geometry of the T-sensor mixing problem showing the boundary conditions used to derive Equation 2.3 from Equation 2.1. Equation 2.3 is only valid if $c_w \approx 0$ at the right-side wall (or equivalently, the z -domain is effectively infinite).

These conditions, when applied to Equation 2.1, yield the following solution for the steady-state concentration field:

$$c_w(z, x) = \frac{1}{2} c_0 \left(1 - \operatorname{erf} \frac{z}{\sqrt{4\phi \frac{x}{u}}} \right), z \geq 0 \quad (2.3)$$

Equation 2.3 shows the water concentration profile in the right half (DMF/solids stream) of the T-sensor with the two-stream interface located at $z = 0$. The value c_0 represents the initial water concentration in the left stream ($z < 0$) and the interfacial water concentration (at $z = 0$) is assumed to reach steady-state ($c_w(0, x \geq 0) = \frac{1}{2}c_0$) immediately.

The set of conditions from Figure 2.1 and Equation 2.2 imply that there are no walls in the system and that water diffuses into a semi-infinite solution of DMF. In practice, however, Equation 2.3 provides an effective description of the concentration field in a T-sensor provided the wall concentration is near zero (or equivalently, while the domain approximates an infinite domain). Once water concentration at the wall is significant, Equation 2.3 is no longer accurate.

Figure 2.2 shows cross-stream water concentration profiles at a set of downstream (x) locations as predicted by Equation 2.3. A downstream velocity of 13 mm/s (typical of the experimental runs) was used and the diffusion coefficient between DMF and water was estimated at $\phi = 5 \times 10^{-10} \text{ m}^2/\text{s}$. The concentration plotted, $c^* = c/c_0$, is the normalized concentration. The results indicate that diffusion of water inside the T-sensor, under these conditions, will occur slowly enough for the onset QDCM self-assembly to be observed at different downstream locations on-chip. For instance, for a c_0 value corresponding to a 50 wt% water-DMF solution, a visible width ($\sim 50 \text{ }\mu\text{m}$) of the

DMF/solids stream would be above the cwc ($\sim 1\text{-}2\text{ wt}\%$) at the $x = 20\text{ mm}$ downstream location, and thus QDCM formation would be expected over that width (at $x = 20\text{ mm}$). The width of the growth region would be expected to grow downstream, following the advance of the cwc as indicated in Figure 2.2.

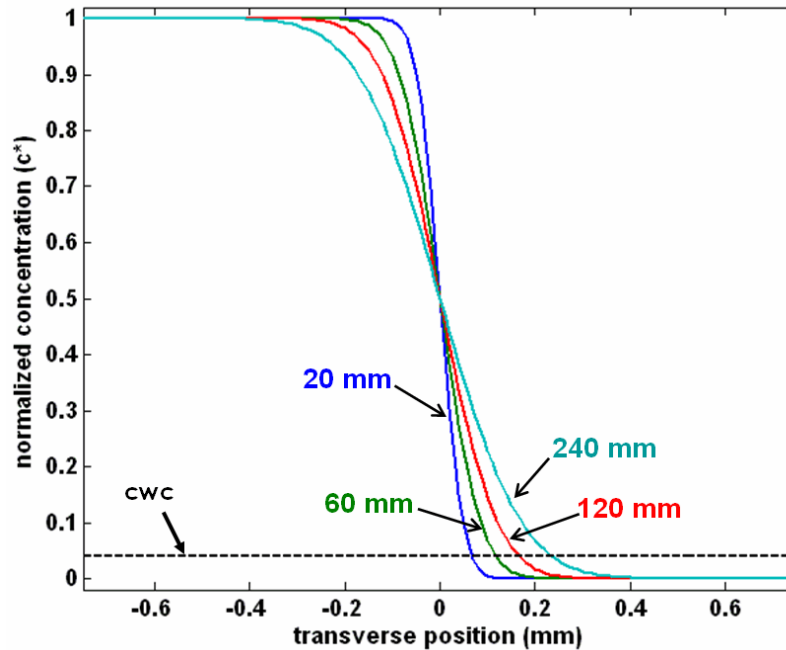


Figure 2.2: The predicted water concentration profiles using Equation 2.3 at 4 downstream (x -direction) positions, in the T-sensor. The walls of the T-sensor are located at $z = \pm 0.75\text{ mm}$ and the water concentration did not change significantly at the walls. The cwc concentration ($\sim 1\text{-}2\text{ wt}\%$) is indicated by a dashed line (assuming a c_0 corresponding to a 50 wt% water-DMF solution).

A major simplification was made in applying Equations 2.1 (and subsequently Equation 2.3) to predict mixing inside the T-sensor. These equations assume one-dimensional cross-stream diffusion and do not account for multi-dimensional effects due to the non-uniformity of the pressure driven velocity profile [Ismagilov et al. (2000); Stone et al. (2004); Bazylak et al. (2005)]. In a wide, thin microchannel the velocity

gradients are most significant in the depth direction, or the out-of-page direction in Figure 1.3. The impact on mixing is commonly referred to as dispersion [Stone et al. (2004)]. Dispersion occurs primarily as a result of particles experiencing different velocities and mixing rates as they move in the vertical direction due to Brownian motion [Probstein (1994)]. Specifically, the cross-stream extent of diffusive mixing near the walls in a T-sensor scales as the one-third power of the downstream distance (x) and scales inversely as the one-third power of maximum flow velocity [Ismagilov et al. (2000)]. These dependencies are in contrast to the cross-stream extent of diffusive mixing in the central plane which scales as the one-half power of downstream distance (x) and scales inversely as the one-half power of average flow velocity [Ismagilov et al. (2000)]. The consequences of these scaling laws are that the effects of dispersion decrease with increasing downstream distance and increase with increasing flow velocity. Equation 2.1 and the analysis above are thus strictly only applicable to the central plane of the microchannel, and underestimate mixing in the near-wall regions.

2.2.2 Particle Size Estimation in a Microfluidic Focuser

Predicting concentration profiles inside a microfluidic focuser required a different solution to Equation 2.1 than that used for the T-sensor. A solution for the concentration of species s , $c_s(z,x)$, for a geometry that closely resembled the focuser geometry was derived from the one-dimensional diffusion equation with the following boundary conditions [Bird et al. (1960)]:

$$\begin{aligned} c_s(0,0) &= \Gamma_s \\ c_s(z \rightarrow \pm\infty, x \geq 0) &= 0 \end{aligned} \tag{2.4}$$

Here, Γ_s is the area under the cross-stream concentration profile at any downstream location ($\Gamma_s = \int_{-\infty}^{\infty} c_s(z, x = \text{const}) dz$). Under these conditions, the solution to Equation 2.1

for the concentration profile $c_s(z, x)$ is:

$$c_s(z, x) = \frac{\Gamma_s}{2\sqrt{\pi\phi\frac{x}{u}}} \exp\left(-\frac{z^2}{4\phi\frac{x}{u}}\right) \quad (2.5)$$

This model represents a spike of species s located at $z = 0$ which diffuses into the surrounding bulk fluid as it travels downstream. The $z = 0$ condition is non-physical, but the subsequent diffusion downstream models well the one-dimensional cross-stream diffusion in the focuser configuration. Similarly to Equation 2.3, Equation 2.5 does not account for the presence of the walls in the system in either cross-stream dimension. Thus, Equation 2.5 has restrictions similar to those of Equation 2.3. Unfortunately, this means that Equation 2.5 cannot be used to predict the downstream distance where the system reaches its steady-state water concentration. Equation 2.5 can, however, be used in conjunction with the fluorescence plots obtained during experimentation to estimate the diffusion coefficients of the fluorescent particles (CdS QDs and QDCMs) in the DMF/solids stream. The mean diameter of these can then be estimated using the following relation [Probstein (1994)]:

$$d_{avg} = \frac{2kT}{6\pi\mu\phi} \quad (2.6)$$

Here, d_{avg} is the mean particle diameter, k is Boltzmann's constant (1.38×10^{-23} Nm/K), T is the temperature in Kelvin (300 K) and μ is the dynamic viscosity of the carrier fluid.

The estimates of the diffusion coefficient and mean-particle diameter obtained from Equations 2.5 and 2.6 are presented in Section 2.4.2.1.

It is important to note that while the analytical solutions presented above provide insight into the diffusive transport in the microfluidic systems of interest, they are approximations. Multi-dimensional effects such as dispersion and the effects of solubility gradients are not included in either the T-sensor or the focuser model.

2.3 Experimental Setup

A detailed description of the microfabrication and experimental methodologies employed is provided in Chapter 1. In this section only specifics relating to the chips and experiments described in this chapter are presented.

2.3.1 Microchannel Fabrication

Microchips were fabricated using standard soft-lithographic techniques [McDonald et al. (2000)]. Negative masters were fabricated on glass slides (Erie Scientific, NH) using a negative-tone photoresist, SU-8 (Microchem, MA). Prior to use, the glass slides were cleaned and heated on a hotplate to remove all moisture. SU-8 films 25 μm thick for the T-sensor and 50 μm thick for the focuser were spin-coated on top of glass slides. The glass slides were then heated to 95 $^{\circ}\text{C}$ for 15/30 minutes (25/50 μm films) to evaporate the solvents from the photoresist films. Photomasks were then placed over the films and the devices were exposed to UV light for 40/90 seconds. After

additional heating at 95°C for 5/10 minutes, the devices were submerged in SU-8 developer (Microchem, MA) until all unexposed photoresist was removed.

Microchips were fabricated from poly(dimethylsiloxane) (PDMS) using a SYLGARD 184 silicone elastomer kit (Dow Corning, MI) with an elastomer base to curing agent ratio of 10:1. The elastomer and curing agent were mixed together and poured onto the negative masters in petri dishes. The petri dishes were placed in a vacuum chamber until all air bubbles in the PDMS were removed and then the PDMS was heated at 85 °C until cured. The microchips were cut and peeled off their negative masters and holes were punched through their reservoirs to allow for the insertion of tubing. A thin PDMS film produced on top of a glass slide by spin-coating was permanently sealed to the base of each microchip after the components were exposed to oxygen plasma for 30 seconds.

2.3.2 Chemical Preparation

PS-CdS and PS(665)-*b*-PAA(68) were provided by the collaborating research group (Moffitt Lab, UVic Chemistry), and dispersed separately in DMF (99.9+ % HPLC Grade, H₂O < 0.03%), each at a total solids concentration of 2 wt%. The solution of stabilizing chains and dispersion of PS-CdS were then combined to form a 50/50 (w/w) blend of constituents in DMF. DMF/water mixtures were created by adding 99.9% pure de-ionized water to DMF on a digital balance (Denver Instrument, CO) to produce mixtures containing 6 and 12 wt% water. Fluorescent dye solution was prepared from fluorescein powder (Invitrogen Inc., ON) dissolved in water at a concentration of 0.2

mM; the fluorescein/water solution was then mixed with DMF to produce a DMF/fluorescein/water solution containing approximately 50 wt% water.

2.3.3 Flow delivery and control

Pressure-driven flow to the inlets of the reactors was provided using 1 mL (T-sensor) and 250 μ L (focuser) gastight syringes (Hamilton, NV) mounted on syringe pumps (Harvard Apparatus, QU). Flowrates were controlled via the syringe pumps. The microchip was connected to the syringes with 1/16th inch (OD) teflon tubing (Scientific Products and Equipment, ON).

2.3.4 Sample Collection and Image Processing

Images of the reactor were captured using a CCD camera (AF6000 Orca, Hamamatsu, NJ) installed on a DMI 6000B inverted microscope (LEICA, NJ). Fluorescence filter cubes (Semrock, NY) inside the microscope were used to capture the fluorescent light emitted from the QDs and fluorescein. The QD filter cube was custom designed for the CdS QDs of interest and transmitted excitation light between 350 and 400 nm to the microscope stage and emission light with a wavelength above 500 nm to the CCD camera. This filter was well suited for tracking CdS QD emission which have an absorption threshold of 465 nm and broad red-shifted emission band centered near 600 nm [Yusuf et al. (2007a)]. The fluorescein filter cube transmitted excitation light

between 450 and 500 nm to the microscope stage and emission light between 510 and 560 nm to the CCD camera.

Image normalization was employed to facilitate comparisons of light emission from QDCMs as compared to the base case of QD fluorescence and to remove non-uniformities in illumination and the image field. The DMF/solids phase constituted the bright field and DMF/water phase constituted the dark field. For the flow-focusing reactor, normalized images were also generated for fluorescein so that fluorescence intensity could be correlated with water concentration. Using the fluorescein filter cube, the DMF/water/fluorescein phase constituted the bright field and the DMF/solids phase constituted the dark field.

For off-chip QDCM size distribution analysis, QDCM dispersions were collected from the chip following the quench step into vials containing deionized water, such that the estimated solids content of the final aqueous dispersions was ~ 0.25 mg/mL. The Moffitt Group (UVic Chemistry) provided TEM images of the various aqueous QDCM samples performed on a Hitachi H-700 electron microscope, operating at an accelerating voltage of 75 kV. An ~ 10 μ L drop of each QDCM dispersion was deposited on a carbon-coated formvar 300 mesh copper grid and then shadowed with Pt/Pd wire for imaging. Particle size analysis and statistics were carried out on the shadowed samples by the Moffitt Group (UVic Chemistry), with various regions of the TEM grid randomly sampled and a minimum of 201 and a maximum 492 particles measured and included in each analysis. Images of selected samples were also taken without Pt/Pd shadowing, in order to characterize the internal structure of QDCMs.

2.4 Results and Discussion

2.4.1 QCDM Self-Assembly in a Microfluidic T-Sensor

The microfluidic self-assembly strategy employed here involved combining a stream containing the PS-CdS and PS(665)-*b*-PAA(68) constituents in DMF (DMF/solids stream) with a second stream containing a 50-50 (by volume) DMF/water solution in a long T-sensor. A schematic of the T-sensor chip is shown in Figure 2.3. The spiraling mixing channel enabled the relatively long channel lengths (~600 mm) to be accommodated on a standard microscope glass slide. The flow-through format employed here enabled the steady-state examination of an unsteady process unfolding in the downstream direction. The geometry of the T-sensor (1500 μm wide, 25 μm high and 600 mm long) provided sufficiently large diffusion time-scales so that the various stages of the QDCM self-assembly process could be observed at multiple downstream locations. The flowrates at the DMF/solids and DMF/water inlets were 16 and 14 $\mu\text{l}/\text{min}$ respectively corresponding to a total in-channel average velocity of 13.3 mm/s. The small difference in inlet flowrates was necessary to achieve a balanced flow field due to the different viscosities of DMF (0.802 mPa.s at 25°C) and water (0.901 mPa.s at 25 °C) [Hatch et al. (2004)].

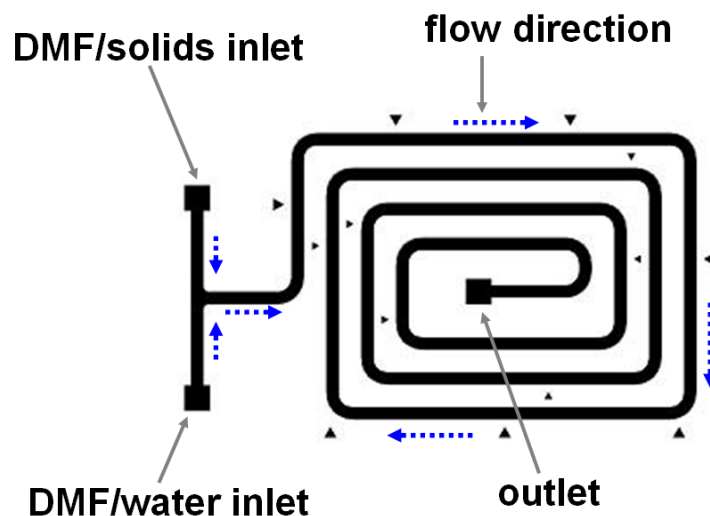


Figure 2.3: Schematic of the microfluidic T-sensor used for QDCM self-assembly.

2.4.1.1 Fluorescence Results

Fluorescence image data was collected at 11 downstream locations in the mixing channel using a CCD camera to collect QD emission from either individually dispersed PS-CdS particles or QDCMs. A compilation of sections from normalized fluorescence images are presented in Figure 2.4. The onset QDCM formation was indicated by an increase in the brightness of the QD fluorescent signal due to increased light scattering of QD emission; increased light scattering was expected where PS-CdS particles and PS(665)-*b*-PAA(68) stabilizing chains self-assembled to form larger QDCMs [Moffitt et al. (1998)]. At the entrance to the mixing channel (0 mm) an increase in brightness was visible at the two-stream interface indicating the onset of localized QDCM formation. This bright region indicating QDCM formation increased in width in the downstream direction, in agreement with the diffusion analysis of Section 2.2.1. The advance of the bright region into the DMF/solids stream (in Figure 2.4), however, occurs more rapidly

than the rate at which the water concentration was predicted (in Figure 2.2) to exceed the c_{wc} , indicating that multi-dimensional effects play a significant role in the mixing process. The images in Figure 2.4 also indicate that the DMF/solids stream shifts to the right, the direction of decreasing water concentration. This effect was observed consistently, and to a greater extent for runs employing higher initial water concentrations. This effect is attributed to the associated solubility gradient which “pushed” the primarily hydrophobic QDCMs and their constituents away from the center of the channel.

Figure 2.5 shows the cross-stream normalized intensity plots of QD emission in the DMF/solids stream at 5 downstream locations in the T-sensor. The bright regions indicative of QDCM formation are readily apparent on these plots as intensity values above unity (the base value intensity for the DMF/solids stream prior to water addition). The intensity levels increased with downstream location in concert with increased QDCM formation. Also noteworthy is the local minima apparent in the 20 mm, 60 mm and 120 mm plots in Figure 2.5. These correspond to the sharp transitions apparent in the associated image data (Figure 2.4). Such discontinuities are rare in microfluidic systems as diffusion is rapid on the characteristic length scale of the channel. While it is not entirely clear why this was observed, one explanation is provided below here. At the cross-stream location corresponding to the c_{wc} , there is an imbalance of diffusion of the PS-CdS QDs. Specifically, PS-CdS QDs that diffuse across the c_{wc} become entrained into larger QDCMs and their diffusion coefficient is reduced. In this way the c_{wc} acts as a one-way trap for diffusing PS-CdS QDs, resulting in local depletion of PS-CdS QDs near the boundary. While the above provides a partial explanation, it is noteworthy that

there are several coupled effects present that complicate the situation including solubility-based focusing, diffusion of both particle types, as well as increased light scattering from the QDCMs.

In summary, the results presented in this section demonstrate that the QDCM self-assembly process can be facilitated and monitored in a microfluidic T-sensor reactor using fluorescence microscopy. The developed T-sensor geometry is useful for studying the formation of QDCMs, however it is not well-suited to generating uniform QDCM populations with specific properties.

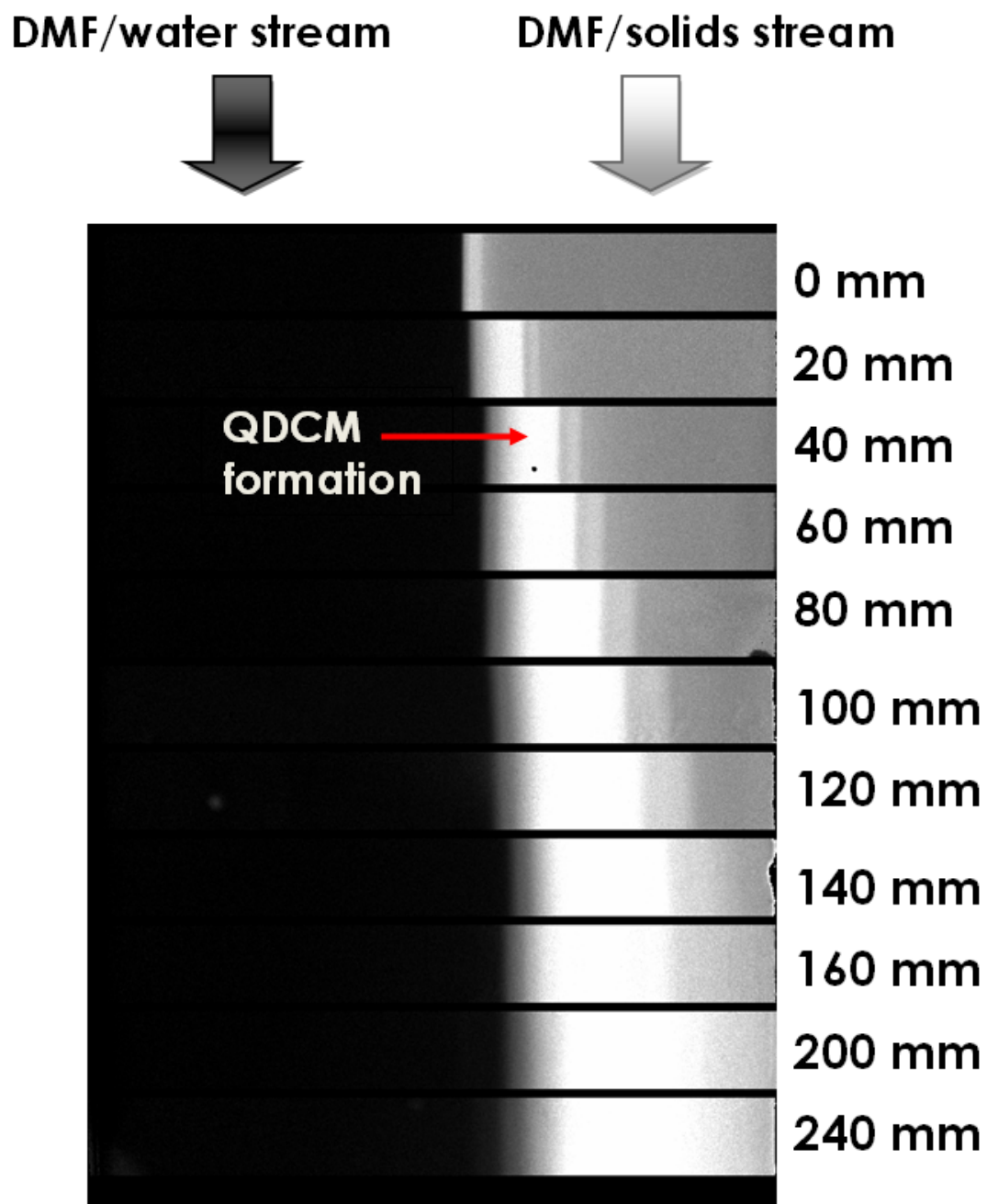


Figure 2.4: Compilation of normalized fluorescence images of the T-sensor taken during the QDCM self-assembly process at 11 different downstream locations in the mixing channel.

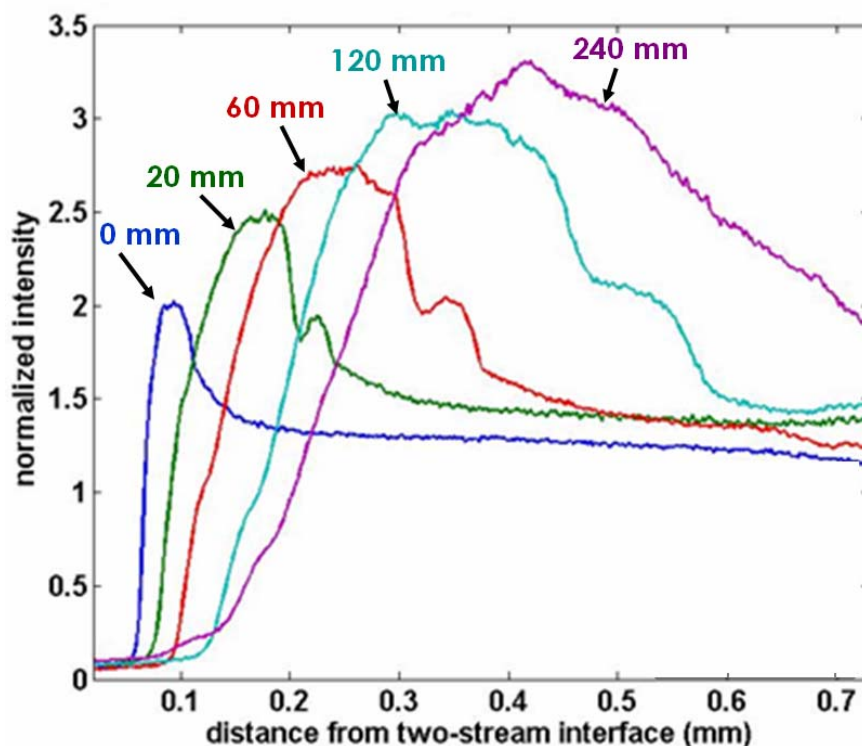


Figure 2.5: Normalized cross-stream fluorescence intensity plots in the DMF/solids stream of the T-sensor at five downstream locations in the mixing channel.

2.4.2 QDCM Self-Assembly in a Microfluidic Flow-Focusing Reactor

This microfluidic QDCM self-assembly strategy involved focusing a stream containing the PS-CdS and PS(665)-*b*-PAA(68) constituents in DMF (DMF/solids stream) with a sheath-flow of DMF/water solution (DMF/water stream) in a channel (growth channel), followed by a similar focusing step with pure water in order to quench the mixture. A schematic of the reactor, and image of a fabricated chip are provided in Figure 2.6. The intention of this strategy is to facilitate a relatively uniform growth period followed by a rapid quench. This configuration is more flexible than the T-sensor, and is designed with the aim to facilitate (as much as possible) similar conditions for the

entire DMF/solids solution and thus output QDCMs with similar and controllable properties. Specifically, as the inlet streams mix due to cross-stream diffusion, water penetrates the central stream and QDCMs are formed where the local water concentration surpasses the cwc (~1-2 wt%). Provided that the inlet solutions and flow rates are set such that the cross-sectional average water concentration remains below the range where QDCMs become kinetically frozen (~8-11 wt%) [Zhang et al. (1997)], continued QDCM growth throughout the growth channel is expected. The growth phase ends with a quench step accomplished by focusing the growth channel output with pure water. The geometry of the growth channel (250 μm wide, 50 μm high and 240 mm long) provided time for the two streams to fully mix, along with additional time for QDCMs to grow. The flowrates at the DMF/water and quenching water inlets were two- and six-times greater than the flowrate at the DMF/solids inlet respectively. Total growth channel flowrates of 3 and 9 $\mu\text{L}/\text{min}$ were employed, corresponding to in-channel average velocities of 4 and 12 mm/s and average growth channel residence times of 60 and 20 s, respectively.

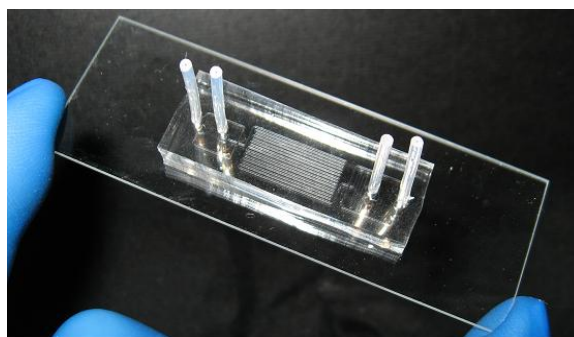
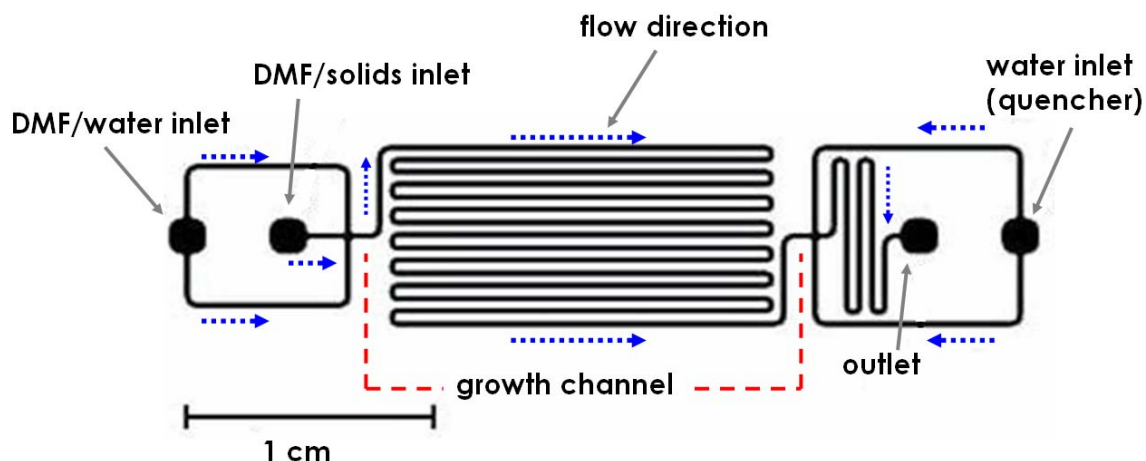


Figure 2.6: Schematic of the microfluidic flow-focusing reactor used for the self-assembly of QDCMs. The DMF/solids stream was focused by a sheath-flow of DMF/water and species mixing and particle growth occurred in the 240 mm long growth channel before the quench step where sufficient water was focused into the system such that the QDCMs became kinetically frozen. The flowrates at the DMF/water and water inlets were two- and six-times greater than that of the DMF/solids inlet, respectively.

At both flowrates, trials were conducted at inlet water concentrations (DMF/water stream) of 0, 6, 12 and 50 wt%, corresponding to cross-sectional average water concentrations of 0, 4, 8, and 33 wt% respectively; a steady-state water concentration of 33 wt% was selected to be well above the range where the QDCMs become kinetically frozen, whereas steady-state water concentrations of 4 and 8 wt% were expected to allow for QDCM growth throughout the growth channel prior to quenching. No QDCM

formation was expected in the 0 wt% water trial, which corresponded to no water addition in the channel.

2.4.2.1 Fluorescence Results

Fluorescence image data for the various trials were collected at a series of downstream locations using a CCD camera to collect QD emission from both individually dispersed PS-CdS particles or QDCMs. To provide a tracer of water diffusion into the DMF/solids stream, a DMF/fluorescein/water solution was used in the 33 wt% case, and fluorescein emission was tracked independently. Normalized fluorescence images are presented in Figures 2.7 and 2.8, for total growth channel flowrates of 3 and 9 $\mu\text{L}/\text{min}$, respectively. In Figures 2.7 and 2.8, the onset of QDCM formation was indicated by an increase in the brightness of the QD fluorescent signal in the central stream, as observed in the T-sensor results. The branched geometry at the top of the 0 mm images indicates the beginning of the growth channel where the central DMF/solids and sheath DMF/water streams first came into contact. The images corresponding to the 15 mm downstream location showed significantly increased signal in the 4, 8 and 33 wt% trials, in contrast to no detectable increase in signal in the 0 wt% trial (where no self-assembly was expected or detected). The dependence of QDCM formation on the diffusion of water into the central stream was particularly apparent in the 33 wt% case, where local increases in the brightness of the QD signal at the beginning of the growth channel (0 mm) indicate rapid formation of QDCMs at the interface between the two solutions.

Figures 2.7 and 2.8 also show that formed QDCM particles and their constituents moved in the cross-stream direction in response to a combination of Brownian effects and solubility gradients (as observed in the T-sensor results). When no water was present in the sheath stream (0 wt% water trial), the movement of PS-CdS particles was solely due to Brownian diffusion, and the expected broadening of the cross-stream QD distribution was observed at increasing distances down the channel (Figures 2.7a and 2.8a). However, when water was present in the sheath stream, the cross-stream diffusion of water established solubility gradients which (as in the T-sensor case) resulted in the primarily hydrophobic QDCMs and their constituents being pushed towards the center of the channel, opposing outward Brownian diffusion. This solubility-gradient focusing effect is particularly apparent in the fluorescence images of the 33 wt% cases (Figures 2.7d and 2.8d) where the cross-stream QD distribution was clearly focused between 0 mm and 15 mm downstream. Although focusing of the central stream observed at the microfluidic intersection (0 mm) was primarily hydrodynamic in nature, the further QD focusing seen downstream (15mm) cannot be hydrodynamic and was therefore attributed to solubility gradients. This effect is further indicated in Figure 2.9, in which the QD and fluorescein fluorescence images from Figures 2.7d and 2.7e (0 mm) are combined. In the expanded image, a visible gap is clearly observed between the edges of the detectable fluorescein water tracer and QD emission regions, suggesting solubility-gradient-induced focusing.

The diffusion of water into the central stream had two effects that can be observed by on-chip analysis: 1) the initiation of QDCM formation, indicated by local increases in QD brightness, and 2) solubility-based QD focusing toward the center of the channel.

Both of these effects are apparent in the cross-stream QD emission profiles plotted in Figures 2.10 and 2.11 for growth channel flowrates of 3 and 9 $\mu\text{L}/\text{min}$ and in the images shown in Figure 2.7 and 2.8, respectively. The 0 wt% water profile serves as a reference case in all the plots. In Figures 2.10a and 2.11a, a relative narrowing of both emission profiles was observed in the 4, and 8 wt % water trials; as well, both showed moderately increased fluorescent intensity compared to the 0 wt% water trial with somewhat higher intensities at the edges, indicating the onset of QDCM formation. Even more significant QD focusing and more developed QDCM formation was observed at 0 mm in the 33 wt% trial; the intensity peaks at the edges of the profile indicate rapid QDCM formation and solubility-based focusing at the interface with the relatively concentrated DMF/water sheath stream. Figures 2.10b-e and 2.11b-e show the evolution of these QD emission profiles downstream. The 0 wt% water profile becomes significantly broader than the 4, 8, and 33 wt% water trials due to the combination of the initial solubility-based focusing effect and reduced diffusion associated with the larger QDCM particles. For completeness, normalized cross-stream concentration profiles for the fluorescein water tracer are provided in Figure 2.12.

Quantitative on-chip analysis of QDCM size and growth dynamics through fluorescence imaging was difficult for two reasons: firstly, the diffraction limit did not allow direct visualization of the mesoscale QDCM particle sizes via fluorescence microscopy; secondly, size analysis based on cross-stream QDCM diffusion was complicated by a combination of particle growth and QD focusing. For the 0 and 33 wt% water trials, however, estimates of the mean particle diameters from observed diffusive broadening of the particle streams were carried out in regions where no QDCM formation

was expected. The analytical solution for the one-dimensional diffusion equation (Equation 2.5) indicated that the QD stream in the 0 wt% water trial exhibited a diffusion coefficient of $\sim 2 \times 10^{-10} \text{ m}^2/\text{s}$, which corresponds to a hydrodynamic diameter of PS-CdS QDs of $\sim 3 \text{ nm}$ (Equation 2.6). This was significantly smaller the hydrodynamic diameter of $\sim 36 \text{ nm}$ measured by Yusuf et al. (2007a). This disagreement is attributed to the multi-dimensional effects which were not considered in this analysis. Similarly, the analytical solution for the one-dimensional diffusion equation (Equation 2.5) indicated that the QDCM stream in 33 wt% water exhibited a diffusion coefficient of $\sim 5 \times 10^{-12} \text{ m}^2/\text{s}$, which corresponds to an estimated mean particle diameter of $\sim 100 \text{ nm}$ (Equation 2.6).

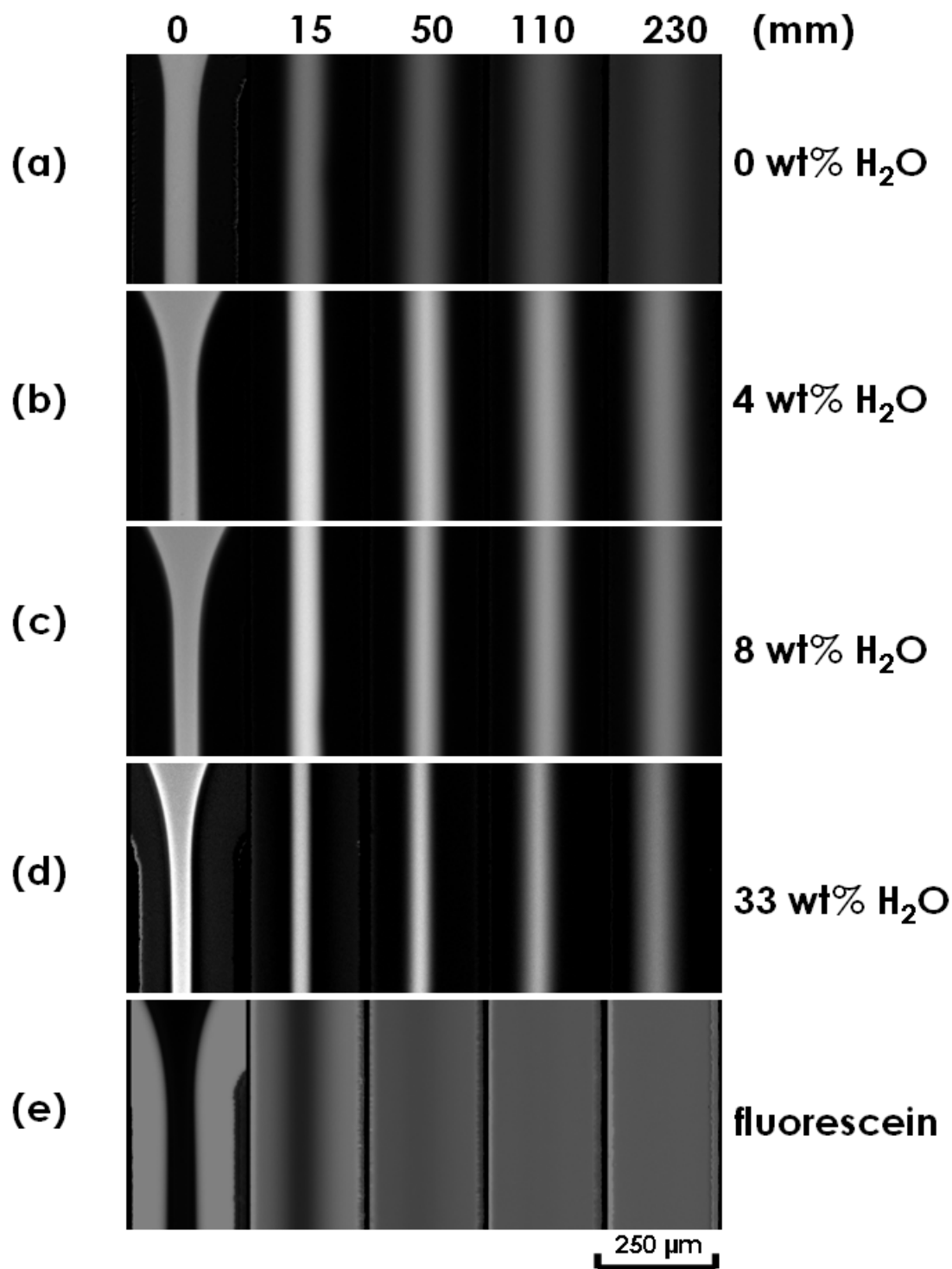


Figure 2.7: Normalized fluorescence images of the QDCM self-assembly process in the flow-focusing reactor (at the downstream locations indicated) for a total growth channel flowrate of $Q = 3 \mu\text{L}/\text{min}$ ($u = 4 \text{ mm}/\text{s}$) and total cross-sectional average water concentrations of (a) 0 wt%, (b) 4 wt%, (c) 8 wt%, (d) 33 wt%, and (e) 33 wt% with a fluorescein tracer imaged.

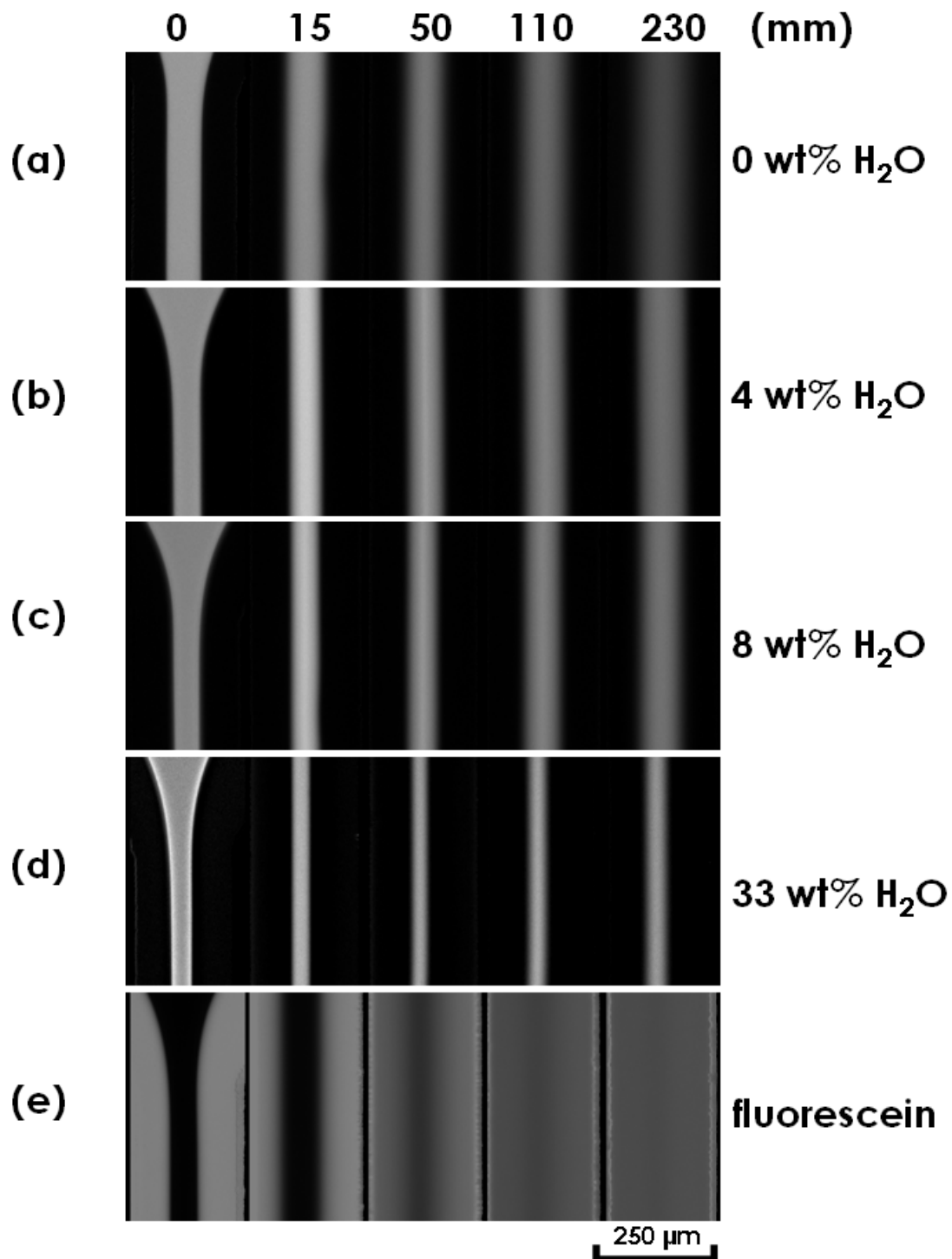


Figure 2.8: Normalized fluorescence images of the QDCM self-assembly process in the flow-focusing reactor (at the downstream locations indicated) for a total growth channel flowrate of $Q = 9 \mu\text{L}/\text{min}$ ($u = 12 \text{ mm}/\text{s}$) and total cross-sectional average water concentrations of (a) 0 wt%, (b) 4 wt%, (c) 8 wt%, (d) 33 wt%, and (e) 33 wt% with a fluorescein tracer imaged.

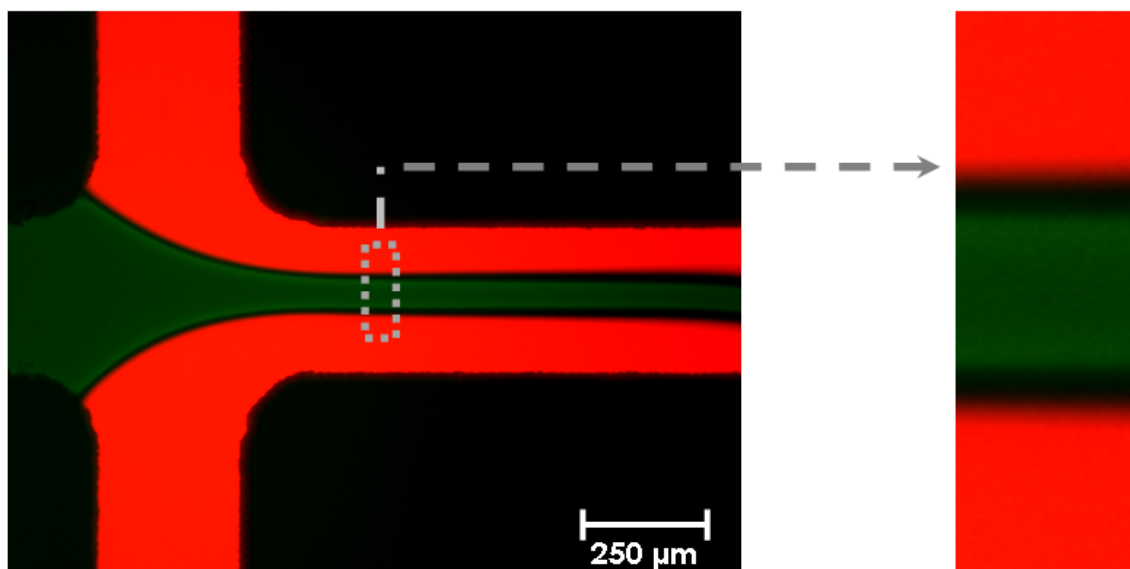


Figure 2.9: Fluorescein and QD emission based analysis: combined image of fluorescein emission (shown red) and QD emission (shown green) with expanded cross-stream region.

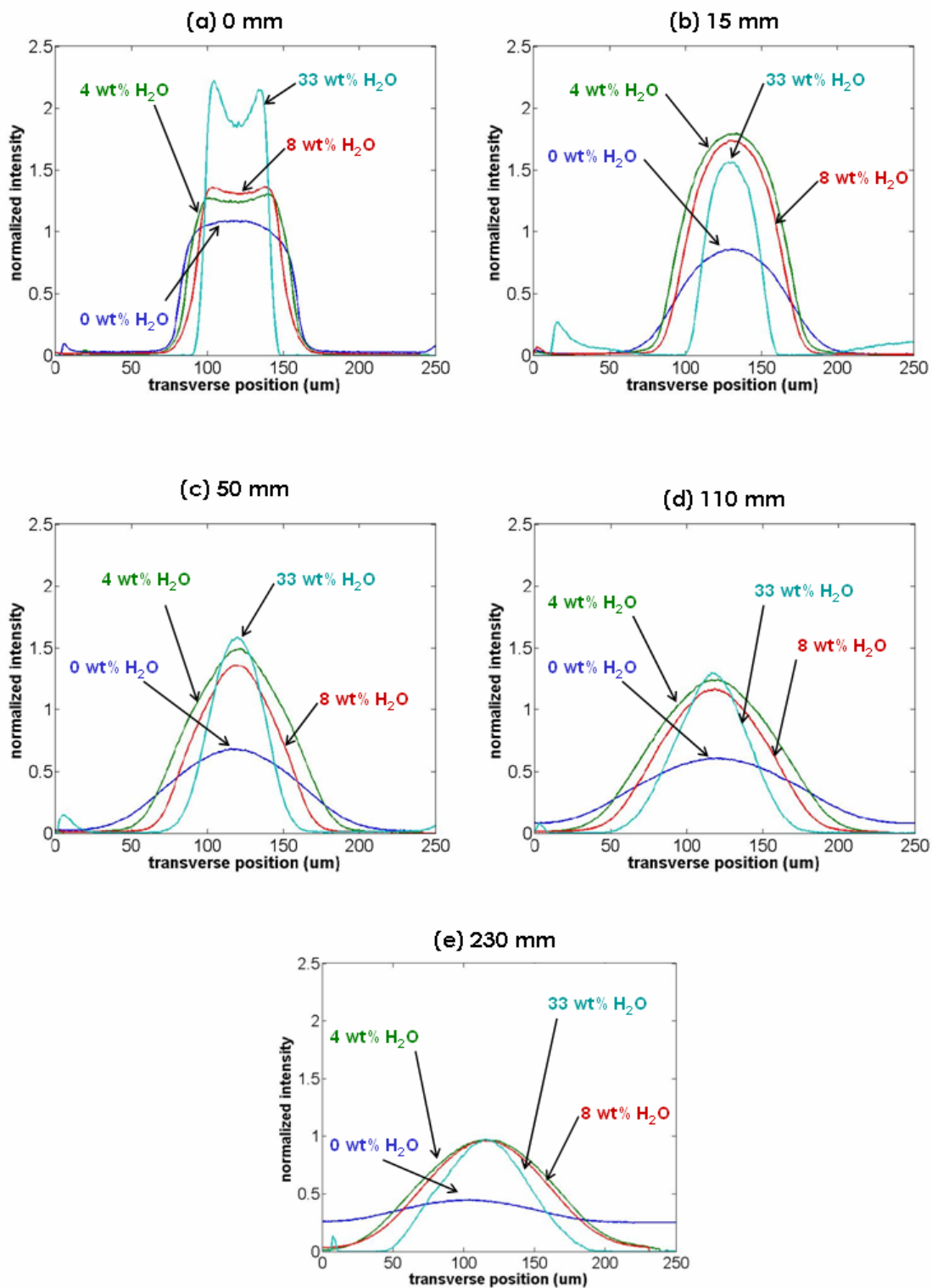


Figure 2.10: Cross-stream QDCM normalized intensity profiles with $Q = 3 \mu\text{L}/\text{min}$ at 5 different downstream locations in the growth channel (a) 0 mm, (b) 15 mm, (c) 50 mm, (d) 110 mm and (e) 230 mm. A normalized intensity value of 1 represents base-case QD emission prior to QDCM formation.

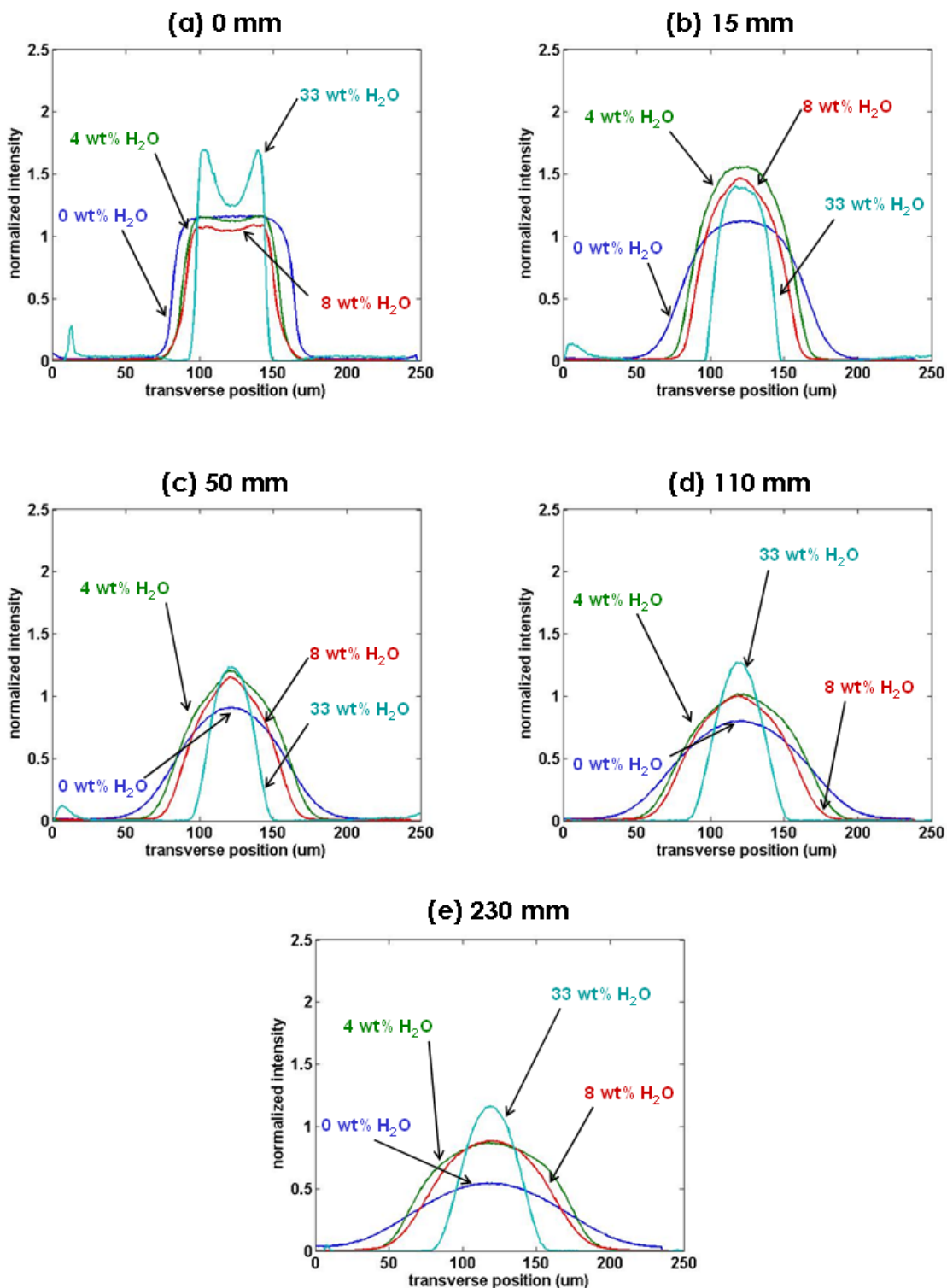


Figure 2.11: Cross-stream QDCM normalized intensity profiles with $Q = 9 \mu\text{L}/\text{min}$ at 5 different downstream locations in the growth channel (a) 0 mm, (b) 15 mm, (c) 50 mm, (d) 110 mm and (e) 230 mm. A normalized intensity value of 1 represents base-case QD emission prior to QDCM formation.

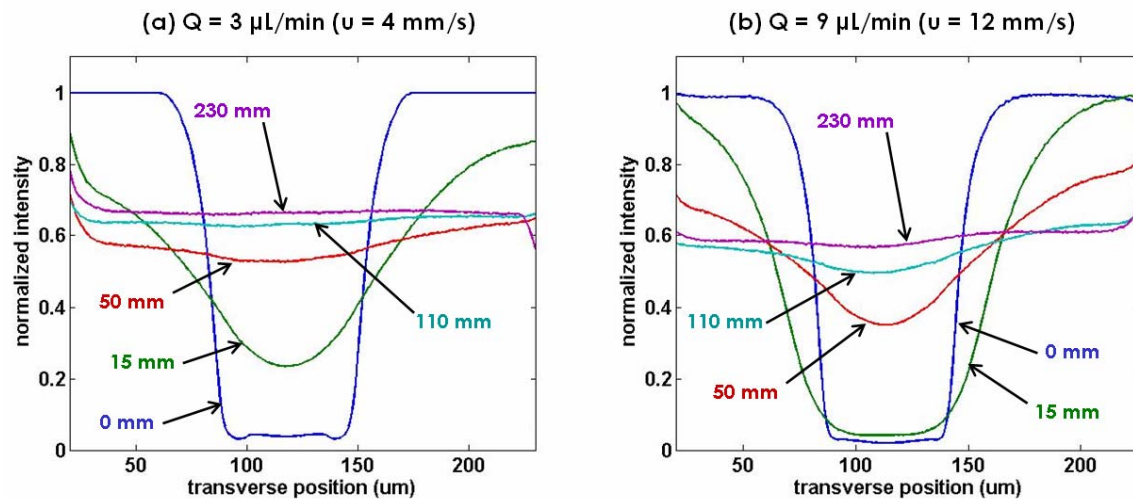


Figure 2.12: Cross-stream fluorescein intensity for the 33 wt% trial at growth channel flowrates of (a) $3 \mu\text{L}/\text{min}$ and (b) $9 \mu\text{L}/\text{min}$.

2.4.2.2 TEM Results

Off-chip TEM imaging of QDCMs formed in this microfluidic reactor under different average water concentrations and flowrates provided a more quantitative measure of particle size distributions than fluorescence imaging. Images of QDCMs prepared in the 4 wt%, $Q = 3 \mu\text{L}/\text{min}$ trial are shown in Figure 2.13, confirming self-assembly by this microfluidics-based approach. These particles were not shadowed with Pt/Pd prior to imaging, allowing their internal structure to be visualized. The dark grey spheres indicate the self-assembled PS chains which make up the matrix of the QDCM interior, with well-dispersed CdS QDs (dark dots) distributed throughout the spheres. Also apparent are the lighter-contrast PAA layers surrounding each QDCM. The aggregation of QDCM particles observed in the image is an artifact of solvent evaporation on the TEM grid; dynamic light scattering of similar QDCM particles confirms that they are well-dispersed, stable colloids in water [Yusuf et al. (2007a)].

Representative TEM images of QDCMs with Pt/Pd shadowing are provided in Figure 2.14 for the 4, 8, and 33 wt% water trials at flowrates of 3 and 9 $\mu\text{L}/\text{min}$. Corresponding particle size distributions are provided in Figure 2.15. Most importantly, these TEM results demonstrate that the QDCM self-assembly process with size-control was achieved with the microfluidics-based method developed here. In all cases, the standard deviations of the QDCM populations are between 24-29% of the mean, consistent with polydispersities demonstrated previously using the method of drop-wise water addition at a constant rate [Yusuf et al. (2007a)]. The observed influences of average water concentration and total flowrate are discussed below.

The TEM results indicate that it is possible to control the sizes of QD/polymer assemblies formed in the flow-focusing reactor via the water concentration of the sheath fluid. The mean QDCM diameter as a function of average water concentration in the channel is plotted in Figure 2.16 for both flowrates, showing that QDCM size decreases with increasing water concentration. The 4, 8 and 33 wt% trials at 3 $\mu\text{L}/\text{min}$, for instance, result in QDCM mean diameters of 85 nm, 67 nm, and 46 nm, respectively. It has been previously demonstrated that QDCM particle sizes are ultimately determined by the progressive decrease in the mobility of PS chains as added water drives the plasticizing DMF from the polymer phase [Yusuf et al. (2007a)]. The observed water concentration dependence is explained as follows: as water diffuses into the central stream, QDCM formation is initiated as the local water concentration surpasses the cwc ($\sim 1\text{-}2$ wt%), beginning at the interface of the DMF/solids and DMF/water streams. Since all average water concentrations (except 0 wt%) are above the cwc at some downstream location, QDCM formation will occur across the entire stream; further downstream, there

will be no further water gradient and all QDCMs will experience the same average water concentration. For higher water concentrations in the sheath stream, cross-stream water diffusion will be faster, such that QDCM formation will occur earlier in the channel; this will result in longer growth times before the final quench. As well, the thermodynamic driving force for domain growth should be larger at higher water concentrations, due to the increase in the quench depth [Termonia (1997)]. However, more importantly, the PS chain mobility will be significantly decreased at higher water concentrations due to lower DMF contents in the polymer phase [Zhang et al. (1997)]; QDCM particles will therefore be harder and particle agglomeration and growth will be slowed, despite longer growth times and a stronger driving force for growth. This kinetic factor appears to dominate the particle size, resulting in the observed decrease in the final QDCM sizes as the water concentration is increased.

Another convenient control parameter is the flowrate, which provides an additional handle with which to vary particle size. As shown in Figure 2.16, increasing the total flowrate by a factor of 3 (from $Q = 3$ to $9 \mu\text{L}/\text{min}$) resulted in a corresponding decrease in the average QDCM residence time in the growth channel from 60 to 20 s, which resulted in a small but notably consistent decrease in mean particle diameter of ~ 4 nm for all cases. Given that cross-stream diffusion dynamics are the primary mixing mechanism, the main influence of increasing the flowrate is decreasing the time available for QDCM growth to occur prior to the final quench stage. The results suggest that some, but very little, QDCM growth occurs after the early stages of the growth channel. This indicates that the QDCM growth rate is non-linear, with assemblies growing rapidly early in the growth channel, and at a much reduced rate further downstream. Considering an

agglomeration model for QDCM growth, this channel-wise nonlinear growth rate can be attributed to two main factors: 1) the local water concentrations will be lower and PS chain mobility will be higher, earlier in the channel; 2) particle number concentrations will be higher in the early stages of growth. The second factor results from particle growth and diffusive broadening of the particle stream, both of which will increase the inter-particle spacing downstream. As well, the QD focusing effect due to initial water concentration gradients, discussed previously, should further concentrate the QDCMs early in the channel, further increasing the growth rate in the early stages. There are additional secondary effects that could also influence self-assembly under these flow conditions, including multi-dimensional mixing effects expected in pressure-driven flows [Ismagilov et al. (2000)] and shear effects [Chen et al. (1997)]. However, shear rates in these cases are rather low, on the order of 10^{-1} N/m, and are thus not expected to significantly influence the self-assembly process.

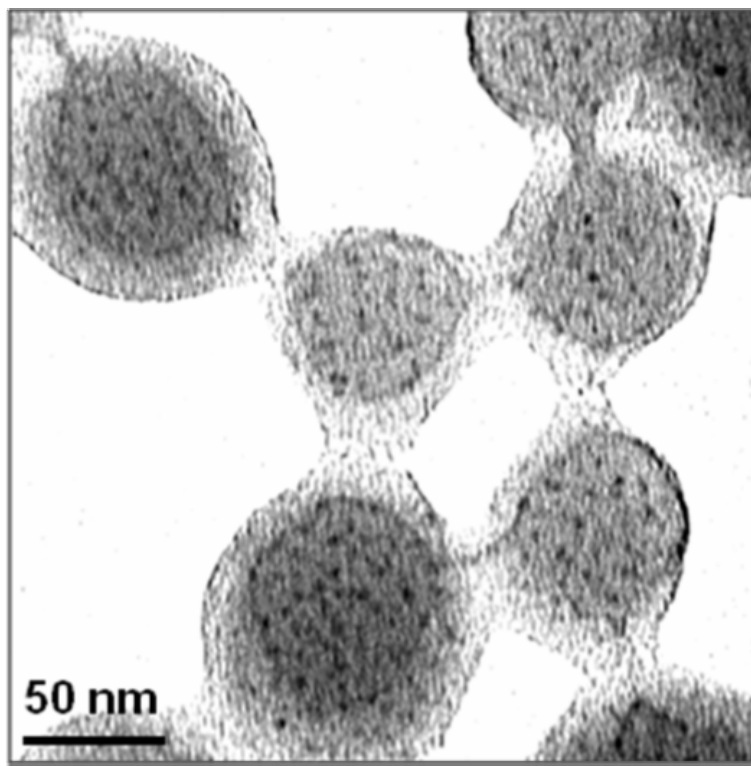


Figure 2.13: A TEM image of QDCM particles formed with the microfluidics-based method. These particles were formed at a total flowrate of $Q = 3 \mu\text{L}/\text{min}$ ($u = 4 \text{ mm}/\text{s}$) and a steady-state water concentration of 4 wt%.

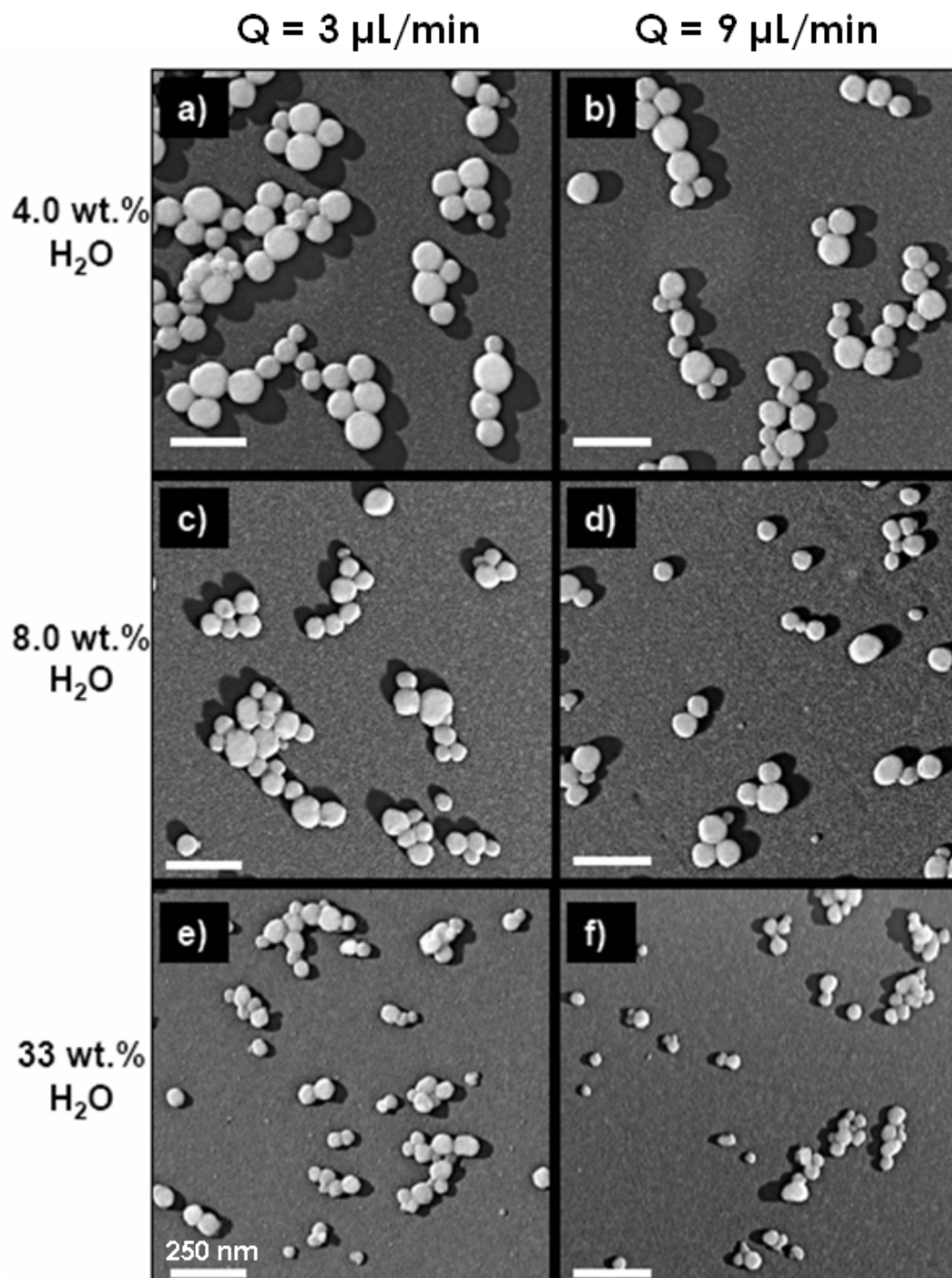


Figure 2.14: Representative shadowed TEM images of QDCMs formed in the flow-focusing microfluidic reactor. The scale bars indicate 250 nm in all cases (TEM images were black/white inverted for presentation). The flowrate was $3 \mu\text{L}/\text{min}$ in (a), (c) and (e) at steady state water concentrations of 4, 8 and 33 wt% respectively. The flowrate was $9 \mu\text{L}/\text{min}$ in (b), (d) and (f) at steady state water concentrations of 4, 8 and 33 wt% respectively.

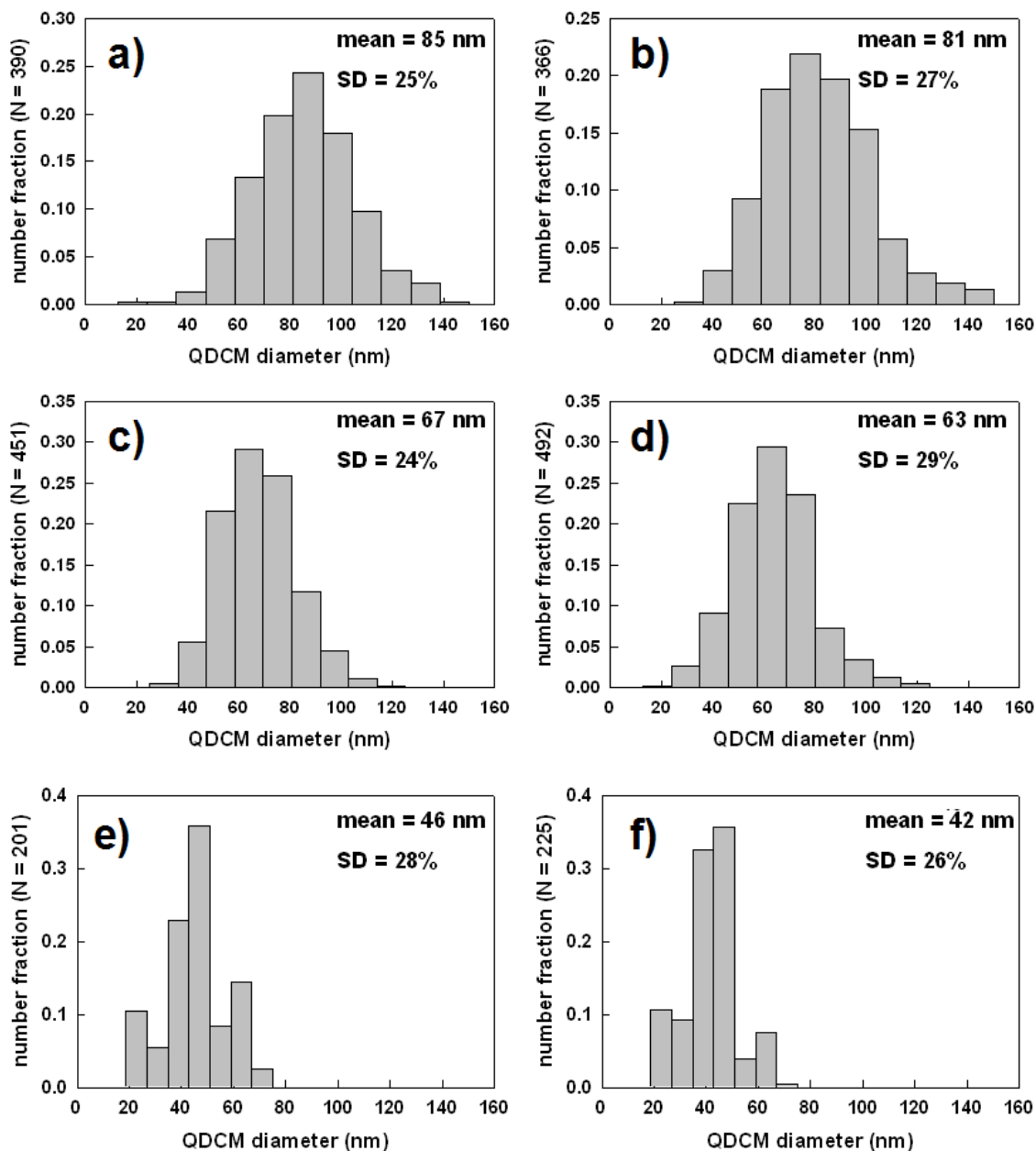


Figure 2.15: QDCM particle size distributions and statistics corresponding to the samples shown in the representative TEM images in Figure 2.14. The flowrate was 3 $\mu\text{L}/\text{min}$ in (a), (c) and (e) at steady state water concentrations of 4, 8 and 33 wt% respectively. The flowrate was 9 $\mu\text{L}/\text{min}$ in (b), (d) and (f) at steady state water concentrations of 4, 8 and 33 wt% respectively.

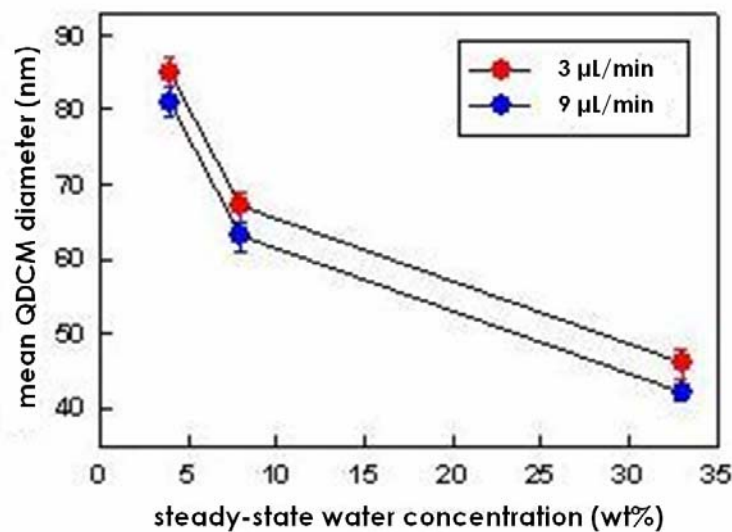


Figure 2.16: Summary plot showing measured mean QDCM diameters as a function of sheath fluid water concentration and total flowrate.

2.5 Summary

In summary, chip-based continuous flow microfluidic reactors were used to control the self-assembly of CdS QDs into aqueous spherical assemblies called QDCMs. Using a T-sensor and flow-focusing reactor, water was introduced into a blend solution of hydrophobic QDs stabilized with a PS brush layer and PS-*b*-PAA stabilizing chains to initiate the self-assembly process and later terminate it. The self-assembly process was observed on-chip using fluorescence microscopy and the onset of QDCM formation was indicated by an increase in the intensity of QD light emission due to light scattering. For the flow-focusing reactor, it was demonstrated through TEM imaging that adjusting the initial water concentration of the sheath-flow stream provided a means for controlling the mean particle diameter of QDCM populations. Steady-state water concentrations of 4, 8 and 33 wt% in DMF produced QDCM populations with mean-particle diameters of 85,

67 and 46 nm respectively. Adjusting the flowrate inside the reactor also provided a small but notable means of adjusting the size of QDCMs. Increasing the growth channel flowrate in the reactor from 3 to 9 $\mu\text{L}/\text{min}$ reduced the mean-particle diameter of QDCM populations by 4 nm at all three water concentrations. In all cases, the polydispersity of QDCMs formed in the flow-focusing reactor was similar to those formed using previous self-assembly methods. The microfluidic reactors described here provided an effective method for controlling the self-assembly of QDs into QDCMs. An alternative microfluidic strategy for QDCM self-assembly is described in the following chapter.

Chapter 3

QDCM SELF-ASSEMBLY IN MULTIPHASE MICROFLUIDIC REACTORS

3.1 Introduction

In this chapter, strategies for the self-assembly of quantum dot compound micelles (QDCMs) in multiphase microfluidic reactors are developed and tested. These strategies involve combining the basic constituents for QDCM formation (PS-CdS and PS-*b*-PAA particles dissolved in DMF with water) in three co-laminar streams and then introducing an immiscible phase of gas or oil into the mixing/growth channel. The interfacial interactions between the two immiscible phases causes one phase to segment into discrete droplets (for oil) or bubbles (for gas) which are carried downstream in the second ‘continuous’ phase in which QDCM formation occurs. Chaotic advection is induced locally in both phases [deMello (2006)] causing the reagents to mix rapidly. Also, the plugs (spaces between droplets or bubbles in the continuous phase) and

droplets/bubbles in a multiphase system move downstream at a similar mean velocity. Thus, with the exception of continuous phase fluid entrained in the film surrounding the droplets/bubbles, every fluid particle experiences a similar on-chip residence time [Günther and Jensen (2006)]. In terms of QDCM processing, this aspect serves to narrow the residence time distribution, and is expected to likewise reduce the particle size distribution of the produced QDCMs. These characteristics make multiphase reactors promising candidates for the self-assembly of QDCMs with uniform and controllable properties.

Multiphase microfluidic systems have been shown in various studies to greatly reduce on-chip mixing times and RTDs when compared to single-phase systems [Tice et al. (2003); Bringer et al. (2004); Günther and Jensen (2006)]. Channel geometries such as a sinusoidal pattern have been used to further enhance mixing rates [Song et al. (2003); Günther et al. (2004)] and in one case, complete mixing of aqueous streams was demonstrated on the order of milliseconds ($\sim 2\text{ms}$) [Song et al. (2003)]. Multiphase microfluidic processing has been successfully applied to the synthesis of various nanoparticles including cadmium selenium (CdSe) QDs [Yen et al. (2005)], CdS and CdS/CdSe nanoparticles [Shestopalov et al. (2004)] and silica particles [Günther et al. (2004)]. In these studies, it was demonstrated that microfluidic multiphase synthesis strategies reduced particle polydispersities and, in some cases, reduced processing times when compared to previous methodologies. Multiphase microfluidics has also been applied to self-assembly processes including the self-assembly of lipid-bilayer membranes [Malmstadt et al. (2006)]. The present work represents, to the authors

knowledge, the first application of multiphase microfluidic processing to QD self-assembly.

In this chapter, multiphase microfluidic processing techniques are developed with the aim of facilitating and controlling the self-assembly of QDs to form QDCMs. These chips have separate feeds for each reactant and are thus more complex, and provide more flexibility than the sheath-flow based reactors developed in Chapter 2. The multiphase flow aspects also introduce additional considerations, with the potential benefit of reduced QDCM polydispersity. Two multiphase reactors are developed: oil was introduced as the immiscible phase in the first reactor and gas in the second. The advantages/disadvantages of both are discussed and fluorescence data obtained from both reactors in operation are analyzed. An off-chip statistical analysis of QDCM distributions assembled under different operating conditions in the gas-liquid reactor is carried out using transmission electron microscopy (TEM). The QDCM characteristics and degree of control achieved with these multiphase methods are compared to those of the sheath-flow reactors presented in Chapter 2.

3.2 Experimental Setup

A detailed description of the microfabrication and experimental methodologies employed is provided in Chapter 1. Similar to Chapter 2, this section provides only specifics relating to the chips and experiments described in this chapter.

3.2.1 Microchannel Fabrication

Microchips were fabricated using standard soft-lithographic techniques [McDonald et al. (2000)]. Negative masters were fabricated on a flat substrate using a negative-tone photoresist, SU-8 (Microchem, MA). High-quality silicon wafers (Silicon Quest Int'l, CA) were used as substrates for the negative masters instead of glass slides, which were used in all previous work. It was found that silicon wafers provided substantially better photoresist-to-substrate adhesion, and this was critical for the relatively large-area and high-channel-density chips required here. Prior to use, the silicon wafers were cleaned and heated on a hotplate to remove all moisture. SU-8 films 50 μm (oil reactor) and 150 μm (gas reactor) thick were spin-coated on the silicon wafers. The silicon wafers were then heated to 95 $^{\circ}\text{C}$ for 30/60 minutes (50/150 μm layers) to evaporate the solvents from the photoresist films. Photomasks were then placed over the films and the devices were exposed to UV light for 90/160 seconds. After additional heating at 95 $^{\circ}\text{C}$ for 10/20 minutes, the devices were submerged in SU-8 developer (Microchem, MA) until all unexposed photoresist was removed.

Microchips were fabricated from poly(dimethylsiloxane) (PDMS) using a SYLGARD 184 silicone elastomer kit (Dow Corning, MI) with an elastomer base to curing agent ratio of 10:1. The elastomer and curing agent were mixed together and poured onto the negative masters in petri dishes. The petri dishes were placed in a vacuum chamber until all air bubbles in the PDMS were removed and then the PDMS was heated at 85 $^{\circ}\text{C}$ until cured. The microchips were cut and peeled off their negative masters and holes were punched through their reservoirs to allow for the insertion of

tubing. A thin PDMS film was formed on a glass slide by spin-coating and was permanently sealed to the base of each microchip following exposure to oxygen plasma for 30 seconds.

The oxygen plasma treatment altered the physical properties of the PDMS transforming its surface from hydrophobic to hydrophilic. For the gas-liquid reactor, a hydrophilic system was desired and the microchip was used immediately after oxygen plasma treatment. A hydrophobic surface was desired for the oil reactor in order to lower the surface energy of the PDMS [Tice et al. (2003)] and these microchips were heated at 110°C for 24 hours after oxygen plasma treatment to revert the PDMS back to its native hydrophobic state.

3.2.2 Chemical Preparation

PS-CdS and PS(665)-*b*-PAA(68) were provided by the collaborating research group (Moffitt Lab, UVic Chemistry), and dispersed separately in DMF (99.9+ % HPLC Grade, H₂O < 0.03%), each at a total solids concentration of 2 wt%. The solution of stabilizing chains and dispersion of PS-CdS were then combined to form a 50/50 (w/w) blend of constituents in DMF. This solution was then further diluted with additional DMF to yield a solution with only 1 wt% solids in DMF. This was necessary because at the original solids concentration (2 wt%), on-chip particle conglomeration was common and would clog the channels of the microfluidic reactors. Reducing the solids wt% in DMF reduced the occurrences of this problem. Reducing the initial solids concentration is known to increase the cwc [Zhang et al. (1997)] and, using previous self-assembly

methodologies, reduce the mean-particle size of QDCM populations [Yusuf et al. (2007a)].

DMF/water mixtures were created by adding 99.9% pure de-ionized water to DMF on a digital balance (Denver Instrument, CO) to produce mixtures containing 12 and 24 wt% water. Fluorescein powder (Invitrogen Inc., ON) was dissolved in water at a concentration of 0.2 mM.

The oil used for the droplet reactors was perfluorodecalin (PFD) (Acros Organics, NJ), a low viscosity oil that is immiscible to water and DMF [Tice et al. (2003)]. This oil was preferred over more readily available oils, such as mineral oil, because its wetting characteristics facilitated water droplet formation in water-PFD systems [Tice et al. (2003)]. For some experiments, a surfactant, 1H,1H,2H,2H-perfluorooctanol (Acros Organics, NJ) was dissolved in PFD at a concentration of 9 wt%. Because the moisture present in air could potentially influence the QDCM self-assembly process, argon, an inert noble gas was used in the gas-liquid reactor.

3.2.3 Flow delivery and control

Pressure-driven flow to the inlets of the reactors was provided using 50, 100 and 250 μL gastight syringes (Hamilton, NV) mounted on syringe pumps (Harvard Apparatus, MA). Flowrates were controlled via the syringe pumps. The microchip was connected to the syringes with 1/16th inch (OD) teflon tubing (Scientific Products and Equipment, ON).

3.2.4 Sample Collection and Image Processing

Images of the reactors were captured using a CCD camera (AF6000 Orca, Hamamatsu, NJ) installed on an inverted microscope (DMI 6000B, LEICA, NJ). The QD filter cube (Semrock, NY) was custom designed for the CdS QDs of interest and transmitted excitation light between 350 and 400 nm to the microscope stage and emission light with a wavelength above 500 nm to the CCD camera. The fluorescein filter cube (Semrock, NY) transmitted excitation light between 450 and 500 nm to the microscope stage and emission light between 510 and 560 nm to the CCD camera.

TEM imaging of produced QDCM samples was performed by the collaborating research group (Moffitt Group, UVic Chemistry) on a Hitachi H-700 electron microscope, operating at an accelerating voltage of 75 kV. For off-chip QDCM size distribution analysis, QDCM dispersions were collected from the chip into vials containing deionized water, such that the estimated solids content of the final aqueous dispersions was ~ 0.25 mg/mL. An ~ 10 μ L drop of each QDCM dispersion was deposited on a carbon-coated formvar 300 mesh copper grid and then shadowed with Pt/Pd wire for imaging. Particle size analysis and statistics were carried out on the shadowed samples, with various regions of the TEM grid randomly sampled. For each sample, the diameters of 300 QDCM particles were measured with a caliper (Mastercraft, FL) on print-outs where the particles were 68,000 times their actual size.

3.3 Results and Discussion

3.3.1 QDCM Self-Assembly in a Microfluidic Droplet Reactor

The microfluidic strategy employed here involved combining the basic constituents for QDCM formation (PS-CdS and PS-*b*-PAA particles dissolved in DMF and water) in three co-laminar streams and then introducing a stream of oil into the reactor. A schematic of the developed microfluidic chip layout is provided in Figure 3.1. The oil used in this work was PFD. Of the first three streams, one contained PS-CdS and PS(665)-*b*-PAA(68) constituents dissolved in DMF (DMF/solids stream) another, a mixture of DMF and water (DMF/water stream) and the third stream, positioned between the first two, contained pure DMF (separator stream). The purpose of the separator stream was to prevent any pre-mixing of reagents prior to droplet formation. Once droplets formed at the injector they traveled downstream through a 10 mm long, 100 μm mixing channel with a sinusoidal pattern [Song et al. (2003)] where the reagents mixed rapidly due to chaotic advection. The droplets then entered the growth channel which was 125 mm long and 100 μm wide. At the end of the mixing channel, the droplets entered an expansion chamber, 1.5 mm wide. The purpose of the expansion chamber was to reduce the fluid velocity sufficiently in order to track the light emission of individual QDCMs through fluorescence imaging. It was anticipated that this reactor would produce sufficiently large QDCMs such that the light emission of individual particles could be measured and correlated with particle diameter. As such, a statistical analysis of the polydispersity of QDCMs formed in this reactor could be conducted using only

fluorescence data. This approach was chosen since fluorescence images require much less time to produce than TEM images. At the end of the reactor, the droplets exited through the outlet and were stored in a waste container. The channel height of the microfluidic reactor was 50 μm .

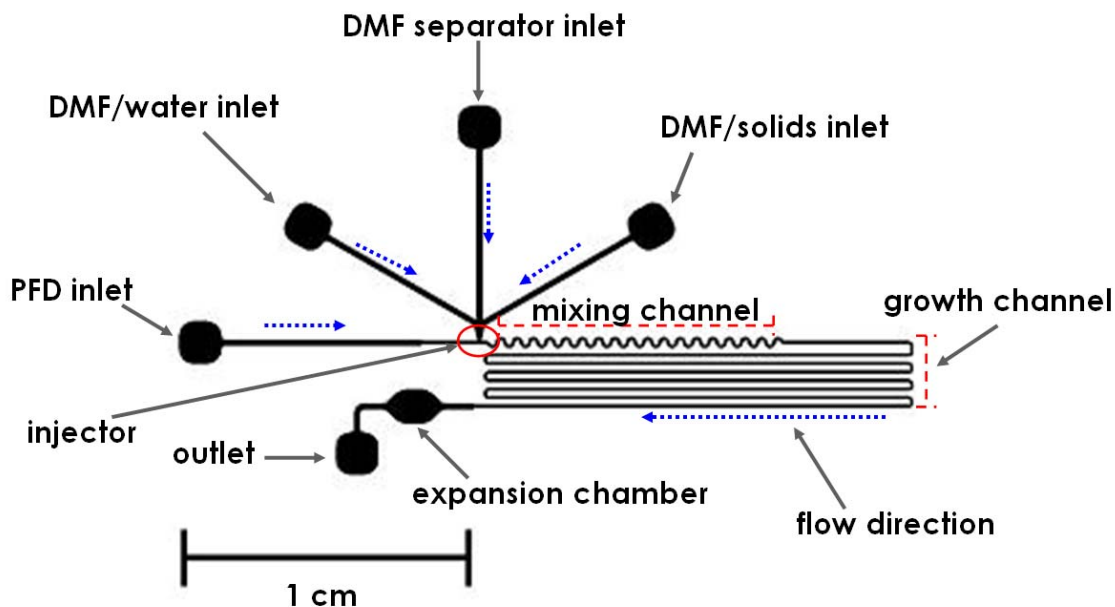


Figure 3.1: Schematic of the microfluidic droplet reactor used for QDCM self-assembly experiments.

In order to achieve the stable formation of water droplets in a water-PFD system, the interfacial tension at the water/PDMS interface (~ 38 mN/m) must be higher than the interfacial tension at the water/PFD interface (~ 55 mN/m) [Tice et al. (2003)]. In order to lower the interfacial tension at the water/PFD interface a surfactant, 1H,1H,2H,2H-perfluorooctanol, was added to PFD at a concentration of 9 wt%. Although the addition of a surfactant to PFD has been shown to result in stable water droplet formation in a water-PFD system [Song et al. (2003); Tice et al. (2003)], it was unknown if it would

also facilitate stable formation of DMF/water droplets in the microfluidic reactor used here.

The flowrate for the DMF/solids, DMF/water and DMF separator streams was 0.1 $\mu\text{L}/\text{min}$. The flowrate of the oil stream was 0.6 $\mu\text{L}/\text{min}$. This corresponded to a total on-chip flowrate of 0.9 $\mu\text{L}/\text{min}$ and a velocity of 3 mm/s. A sensitivity analysis was conducted by varying the water concentration at the DMF/water inlet and by altering the interfacial surface tension of the two-phases by adding the surfactant to the PFD. Trials were conducted using inlet water concentrations of 12 and 100 wt% corresponding to fully mixed water concentrations of 4 and 33 wt% respectively, with and without the addition of the surfactant to PFD. Additional trials were conducted where only water and PFD were introduced into reactor so that the wetting properties of a water-PFD system could be compared to those of a DMF/water-PFD system.

3.3.1.1 Fluorescence Results

Fluorescence images for the various trials were obtained from either individually dispersed PS-CdS particles or QDCMs. Unfortunately, due to the unsteady nature of multiphase flow, it was extremely difficult to obtain bright and dark field image data and thus image normalization was not applied. Thus, a quantitative analysis of on-chip fluorescent intensity could not be conducted. However, fluorescence imaging provided qualitative information regarding the operation of the reactor, particularly the characteristics of the multiphase flow.

Figure 3.2 shows images of fluorescein emission in the serpentine mixing channel for the trial with only fluorescein/water and PFD. Without the addition of the surfactant to the PFD (Figure 3.2a), the two phases each partially wet the channel walls with neither phase forming stable droplets as expected since the interfacial tension of water/PDMS (~ 38 mN/m) [Tice et al. (2003)] is lower than the interfacial tension of water/PFD (~ 55 mN/m) [Tice et al. (2003)]. The addition of the surfactant to PFD (Figure 3.2b) reduces the interfacial tension of water/PFD [Tice et al. (2000)], causing the fluorescein/water phase to form stable droplets and the PFD phase to form the continuous phase. The conditions of Figure 3.2b would be more desirable for the self-assembly process because the reactants were fully encased within the droplets, and would not contact the channel walls where the fluid velocities are reduced due to the no-slip wall condition. Also, the addition of the surfactant significantly reduced the length of each droplet which was desirable since mixing is more rapid in smaller plugs and droplets [Bringer et al. (2004)].

Figure 3.3 shows the QD emission from either individually dispersed PS-CdS particles or QDCMs in a small section of the reactor during the 4 wt% water trial. Similarly to a water-PFD system, without the addition of the surfactant to the PFD, both phases were partially wetting and neither phase formed stable droplets or a continuous phase. The addition of the surfactant to the PFD caused PFD to form stable droplets suggesting that surface energy of the DMF/water solution on PDMS was less than that of PFD on PDMS. This was a less desirable operating condition than if the DMF/water solution formed the droplet phase. With the DMF/water solution as the carrier fluid, the reagents for QDCM formation come in contact with the channel walls where the fluid velocity is slowed due to the no-slip wall condition, increasing the RTD. Figure 3.4 shows QD emission near

the injector during the 33 wt% water trial. Unfortunately, the reactor was highly unstable in this trial and controllable droplet formation was unattainable. This was most likely due to unfavorable interfacial interactions between the three fluids, water, DMF and PFD which were all present in the reactor in significant quantities.

It was determined that the preferred operating condition in the droplet reactor was at a steady-state water concentration of 4 wt% without the addition of the surfactant to the PFD. The partial wetting condition seen in Figure 3.3a was more desirable than having the reagents contained within the continuous phase since the individual DMF/water plugs in a partial wetting environment are more discrete. An additional problem with the use of surfactant in this system was identified; although the surfactant was immiscible in water, it readily dissolved into DMF and thus its performance as a surfactant is in question, and more importantly, it could have unpredictable effects on QDCM formation. Figure 3.5 shows a fluorescence image captured at the expansion chamber during this 4 wt% water trial without the use of the surfactant. In this image, small fluorescent dots are visible and likely represent the emission of individual QDCMs. However the small size of these dots and the background fluorescence made direct size measurements of QDCMs produced with this method impractical. This QDCM self-assembly strategy also involves the added complication of removing the oil from off-chip samples prior to TEM imaging or use. Samples collected from this reactor did not clearly phase separate indicating some homogenization occurred. For the reasons described above, the droplet reactor was discontinued in favor of a gas-liquid reactor.

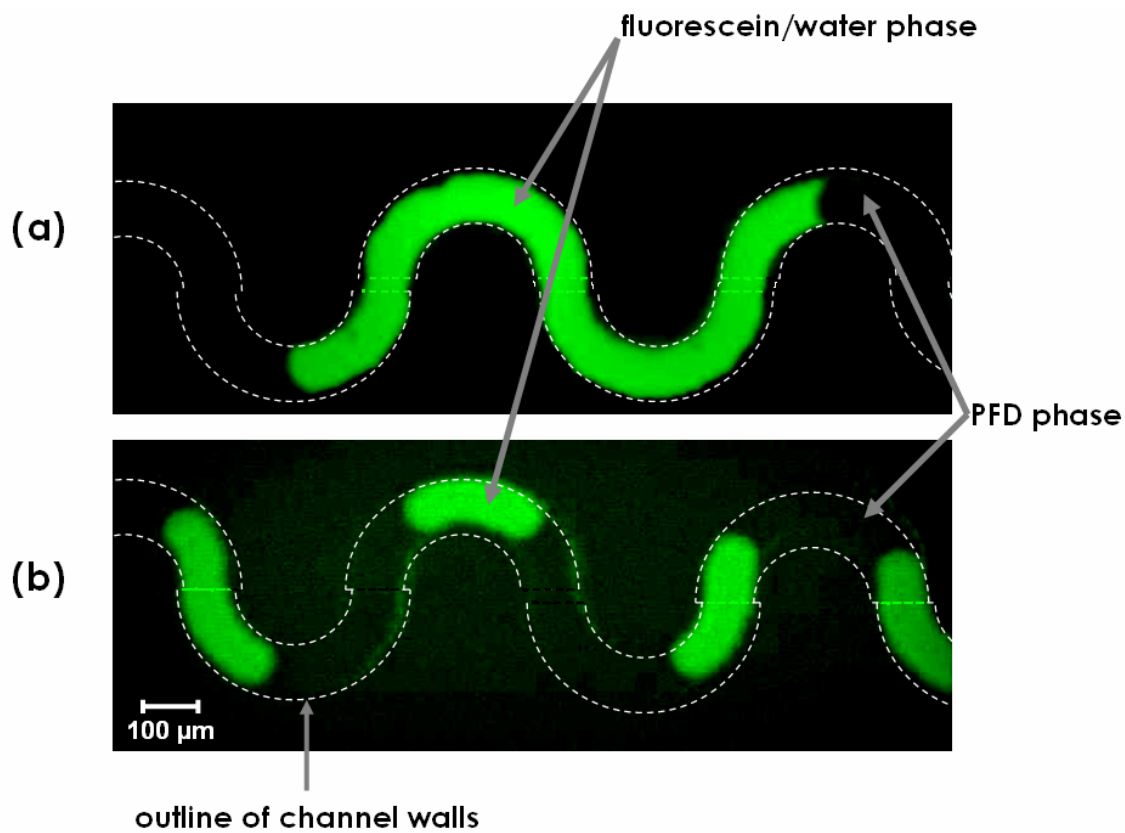


Figure 3.2: Fluorescein emission of fluorescein/water droplets formed in the mixing channel of the microfluidic droplet reactor. (a) No surfactant was dissolved in the PFD. (b) A surfactant, 1H,1H,2H,2H-perfluorooctanol, was dissolved in the PFD at a concentration of 9 wt%. In both cases, the total inlet flowrates for the fluorescein/water phase and PFD were 0.3 and 0.6 $\mu\text{L}/\text{min}$ respectively. (contrast ratio and brightness have been adjusted for clarity of presentation)

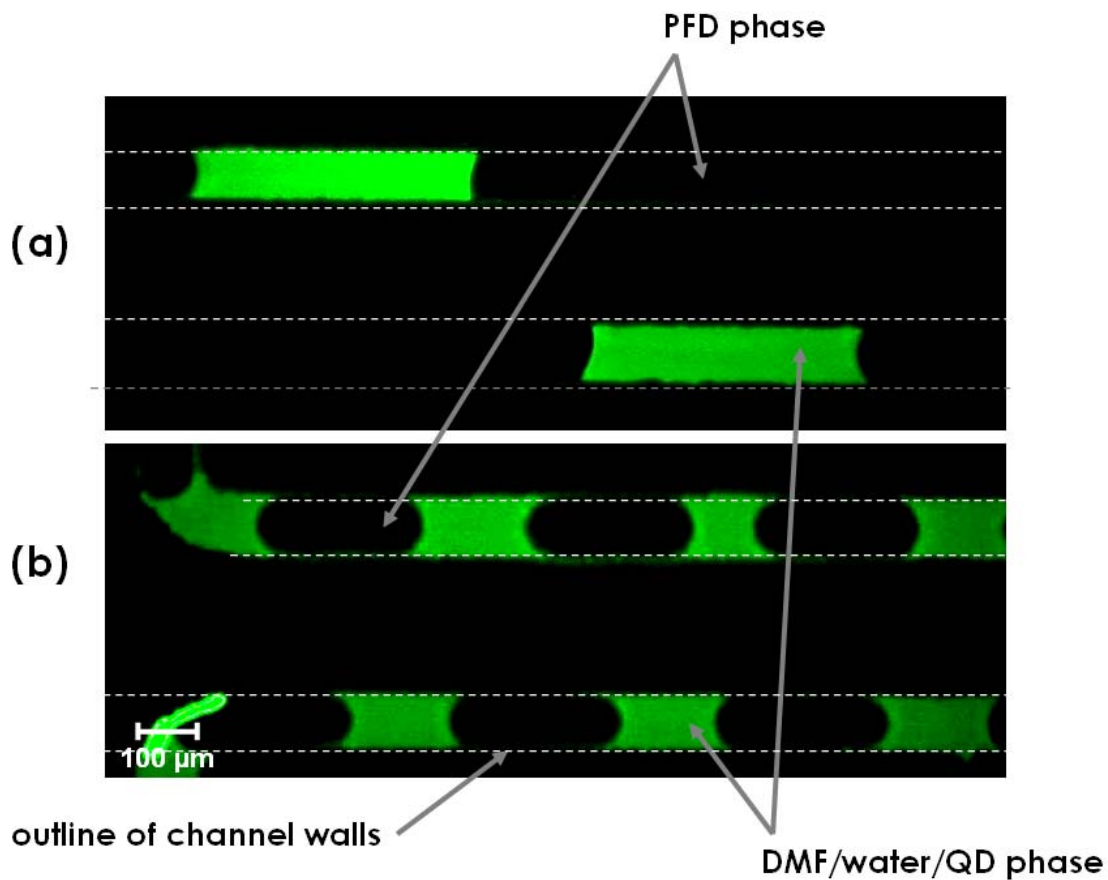


Figure 3.3: QD emission of DMF/water plugs formed in the growth channel of the droplet reactor with a steady-state water concentration of 4 wt%. (a) No surfactant was dissolved in the PFD. (b) A surfactant, 1H,1H,2H,2H-perfluorooctanol, was dissolved in the PFD at a concentration of 9 wt%. In both cases, the total inlet flowrates for the DMF/water/solids phase and PFD were 0.3 and 0.6 $\mu\text{L}/\text{min}$ respectively. (contrast ratio and brightness have been adjusted for clarity of presentation)

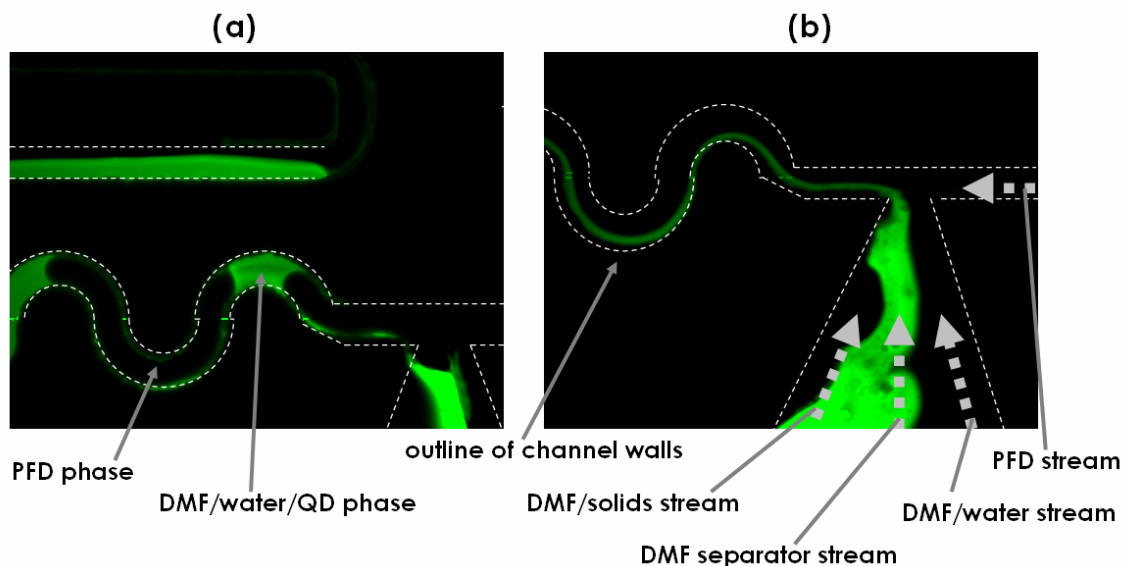


Figure 3.4: QD emission at the injector of the droplet reactor with a steady-state water concentration of 33 wt%. (a) No surfactant was dissolved in the PFD. (b) A surfactant, 1H,1H,2H,2H-perfluorooctonal, was dissolved in the PFD at a concentration of 9 wt%. In both cases the reactor was highly unstable and did not facilitate the QDCM self-assembly process in a controlled or detectable manner (contrast ratio and brightness have been adjusted for clarity of presentation).

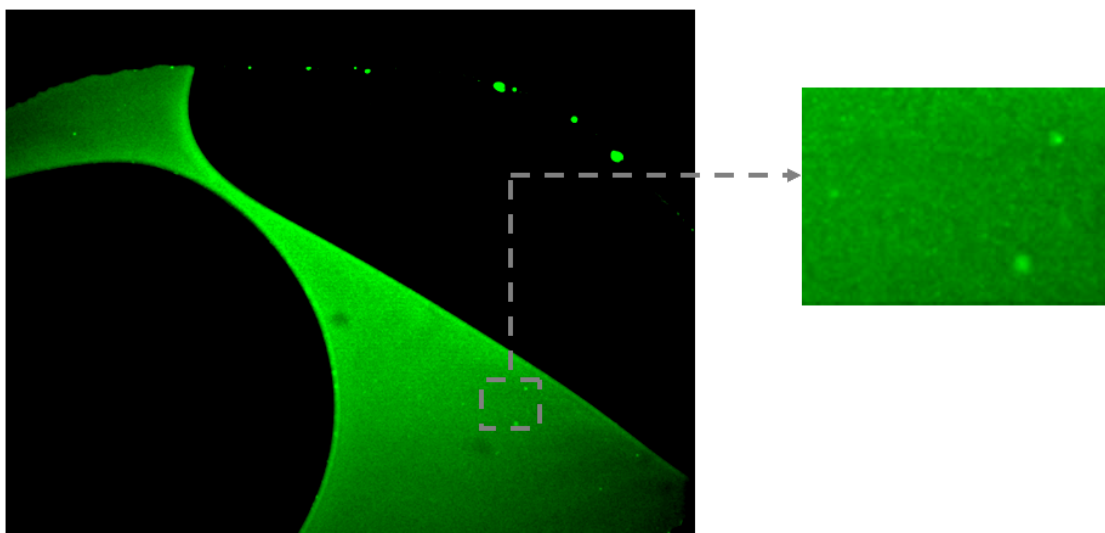


Figure 3.5: QD emission in the expansion chamber of the droplet reactor with a steady-state water concentration of 4 wt%. The small fluorescent dots likely represent the emission of individual QDCMs. However the small size of these dots and the background fluorescent emission made size measurements of QDCMs from these images impractical.

3.3.2 QDCM Self-Assembly in a Microfluidic Gas-Liquid Reactor

The microfluidic strategy employed here involved combining the basic constituents for QDCM formation (PS-CdS and PS-*b*-PAA particles dissolved in DMF and water) in three co-laminar streams and then introducing a stream of gas into the reactor. The gas used was argon. The first three streams were configured as in the droplet reactor with one containing PS-CdS and PS(665)-*b*-PAA(68) constituents dissolved in DMF (DMF/solids stream), another a mixture of DMF and water (DMF/water stream) and the third separating stream containing pure DMF. Gas bubbles formed at the injector and traveled downstream. The liquid and solid reagents traveled downstream in fluid plugs formed between the gas bubbles. In a gas-liquid reactor, the liquid phase is always the carrier fluid and the gas phase is the discrete or ‘droplet’ phase. This is somewhat non-ideal as a thin liquid film is typically present on the channel walls and the reaction occurs in this continuous phase. Similar to the oil phase in the droplet reactor, the liquid plugs come into contact with the channel walls where the fluid velocity slows due to the no-slip wall condition. The result is an increased RTD for the liquid, as compared to the gas phase. Despite this drawback, the liquid plugs do still experience rapid mixing characteristics like droplets inside a droplet reactor and the RTD is still significantly smaller than that of single-phase pressure driven flow [Günther et al. (2004)]. Most importantly from the perspective of QDCM self-assembly, it can be safely assumed that the argon gas phase does not participate in the QDCM formation process and no additional components such as surfactants are required in gas-liquid reactors.

The microfluidic chips employed here were similar in design to the droplet reactor chip. Gas-liquid reactors with lengths of 200 and 740 mm were used and schematics of these reactors are presented in Figures 3.6 and 3.7 respectively. The two gas-liquid reactors with different lengths were used in order to investigate the effects of increasing the on-chip residence time on QDCM size and polydispersity. After bubble formation, the liquid plugs travel through a mixing channel 10 mm long and 100 μm wide. The plugs then enter a widened growth channel, 200 μm wide. In most runs, an off-chip quenching scheme was employed. Liquid exited through the outlet and was transported to a collection vial via 7 cm of Teflon tubing (Scientific Products and Equipment, ON) with an inner diameter of 250 μm . The collection vial was pre-filled with $\sim 250 \mu\text{L}$ of water in order kinetically freeze QDCMs upon entrance. The channel height was 150 μm for the gas-liquid reactor as compared to only 50 μm for the droplet reactor. The channel height was increased in order to facilitate the higher flowrates necessary to achieve stable bubble formation using stepper motor syringe pumps while keeping the on-chip residence times on the order of minutes. The increase in channel height also improved the consistency of bubble formation at the injector. The total QDCM growth times in the two reactors were 2 and 6 minutes including the travel time inside the teflon tube.

It is noteworthy that the chip designs shown in Figures 3.6 and 3.7 and associated channel size specifications and running conditions evolved over many trials and investigations. Originally, an on-chip QDCM quenching scheme was also employed. Specifically, at the end of the mixing channel a stream of water (quencher) entered the reactor in order to kinetically freeze QDCMs. Unfortunately, the presence of two multiphase injection points in one reactor (one at the injector and the second at the

quencher) caused flow instabilities in the reactor that in many cases caused particle conglomeration which blocked the channels. It was found that stable operation could be attained only if the injectors were in phase, and this was not possible to control. Thus, the quencher was blocked and QDCMs were kinetically frozen using the strategy described above.

For all results presented here, the flowrate at each liquid inlet was $0.4 \mu\text{L}/\text{min}$ and the flowrate at the argon inlet was $3.6 \mu\text{L}/\text{min}$ corresponding to a total on-chip flowrate of $4.8 \mu\text{L}/\text{min}$ and growth channel velocity of $2.67 \text{ mm}/\text{s}$. Trials were conducted using inlet (DMF/water inlet) water concentrations of 12 wt% for both reactors and 100 wt% for the 200 mm reactor. This corresponded to steady-state water concentrations of 4 and 33 wt% respectively. An additional trial was conducted using fluorescein (DMF/water inlet) in the 200 mm reactor instead of pure water in order to investigate the mixing rates of DMF and water.

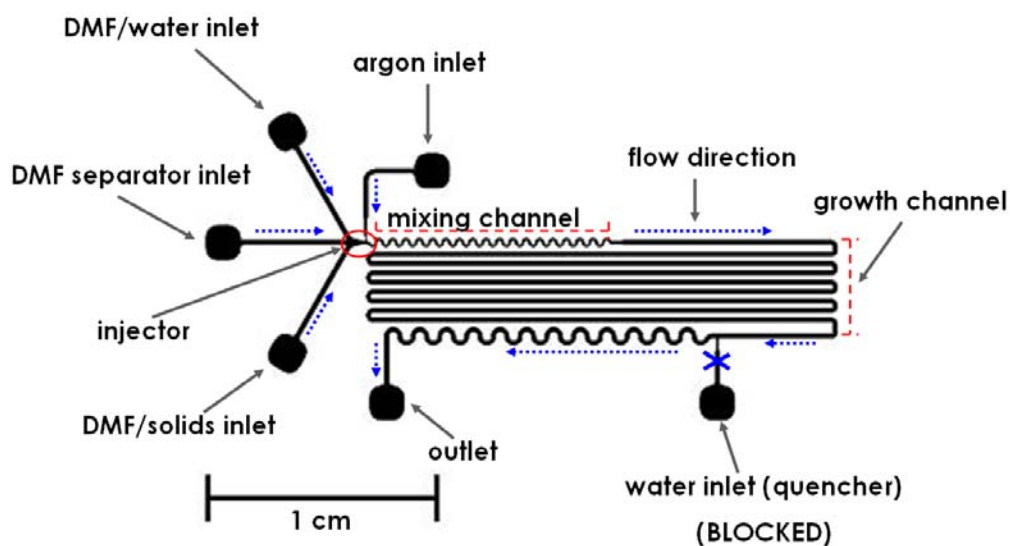


Figure 3.6: Schematic of the 200 mm long microfluidic gas-liquid reactor for QDCM self-assembly experiments.

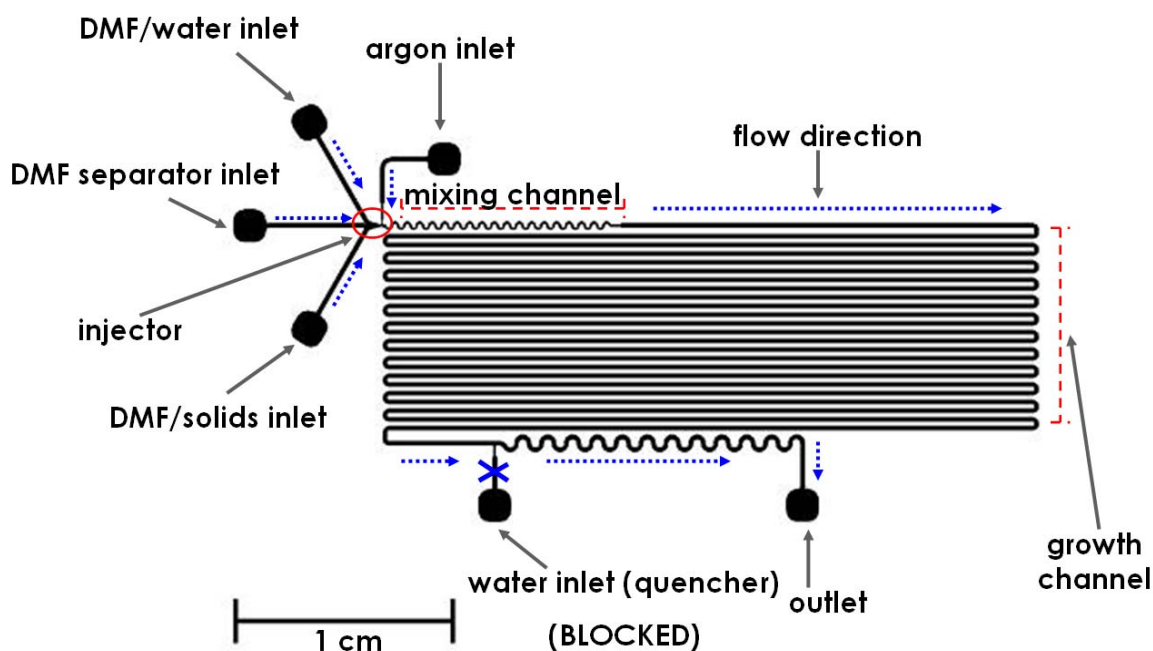


Figure 3.7: Schematic of the 740 mm long microfluidic gas-liquid reactor for QDCM self-assembly experiments.

3.3.2.1 Fluorescence Results

Fluorescence images for the various trials were obtained from either individually dispersed PS-CdS particles or QDCMs. As in the droplet reactor case, it was difficult to obtain bright and dark field image data and data normalization was only employed in a couple of cases.

Figure 3.8 shows the QD emission at three locations in the gas-liquid reactor during operation (200 mm long growth channel, 4 wt% water). These results indicate good segmentation of the liquid flow, full wetting of the liquid phase and stable and repeatable bubble formation and transport without bubble merging or other disturbances. It should be noted that the on-chip quencher was in operation during this run (as shown in

Figure 3.8c). Although at this point the gas-liquid reactor was functioning, particle conglomeration is noticeable at the quencher. In this particular run (and in many others where on-chip quenching was employed) further particle conglomeration over time eventually led to the clogging of the channel. Therefore, in future runs, the inlet to the quencher was blocked and the off-chip quenching strategy described earlier in this section was employed. Noticeable peaks in fluorescent intensity are visible at the gas-liquid interface. These fluorescent peaks are attributed to the refraction of light at the gas-liquid interface and were not an indication of any localized changes in the properties of QDCMs. To confirm this, fluorescence images of fluorescein plugs in an argon-fluorescein system were taken in a different experiment. In Figure 3.9, similar peaks in the intensity of fluorescein emission to those observed in the QD emission from Figure 3.8 are observed, confirming that they are predominantly an artifact of total internal reflection at the gas-liquid surface. This same mechanism has been applied as a microfluidic flow marking technique called micro-bubble lensing induced photobleaching [Sinton (2004)]. The images in Figure 3.10, taken at 100 ms intervals, show the bubble formation process at the injector over one complete cycle. This chip geometry and running parameters resulted in a bubble injection frequency of ~ 5 Hz.

Figure 3.11 shows the fluorescein emission in the mixing channel in the trial where fluorescein was added to water and the steady-state water concentration was 33 wt%. QDs were present in this run, however, their emission was effectively separated from that of the fluorescein by the filter cube. The fluorescein had spread over the entire liquid plug once it had traveled 2 mm downstream from the injector. These results suggest that a uniform concentration of water is achieved within the liquid plugs in less

than one second after the reactants are combined at the injector. In comparison, it took approximately 12 seconds to achieve an approximately uniform concentration of water in the flow-focusing reactor of Chapter 2.

Figure 3.12 shows the QD emission in the mixing channel during the 33 wt% water trial. Fluorescent streamlines in the fluid plug are visible, providing an indication of the advection patterns and subsequent mixing inside the fluid plug. The QDCM particles appear to be almost completely dispersed around the fluid plug 5 mm downstream from the injector, only 2 seconds after leaving the injector. Also, an increase in the brightness of the QD fluorescent signal due to increased light scattering of QD emission is observed as the fluid plug travels downstream. As observed in the sheath-flow reactors of Chapter 2, increased light scattering was expected where PS-CdS particles and PS(665)-*b*-PAA(68) stabilizing chains self-assembled to form QDCMs.

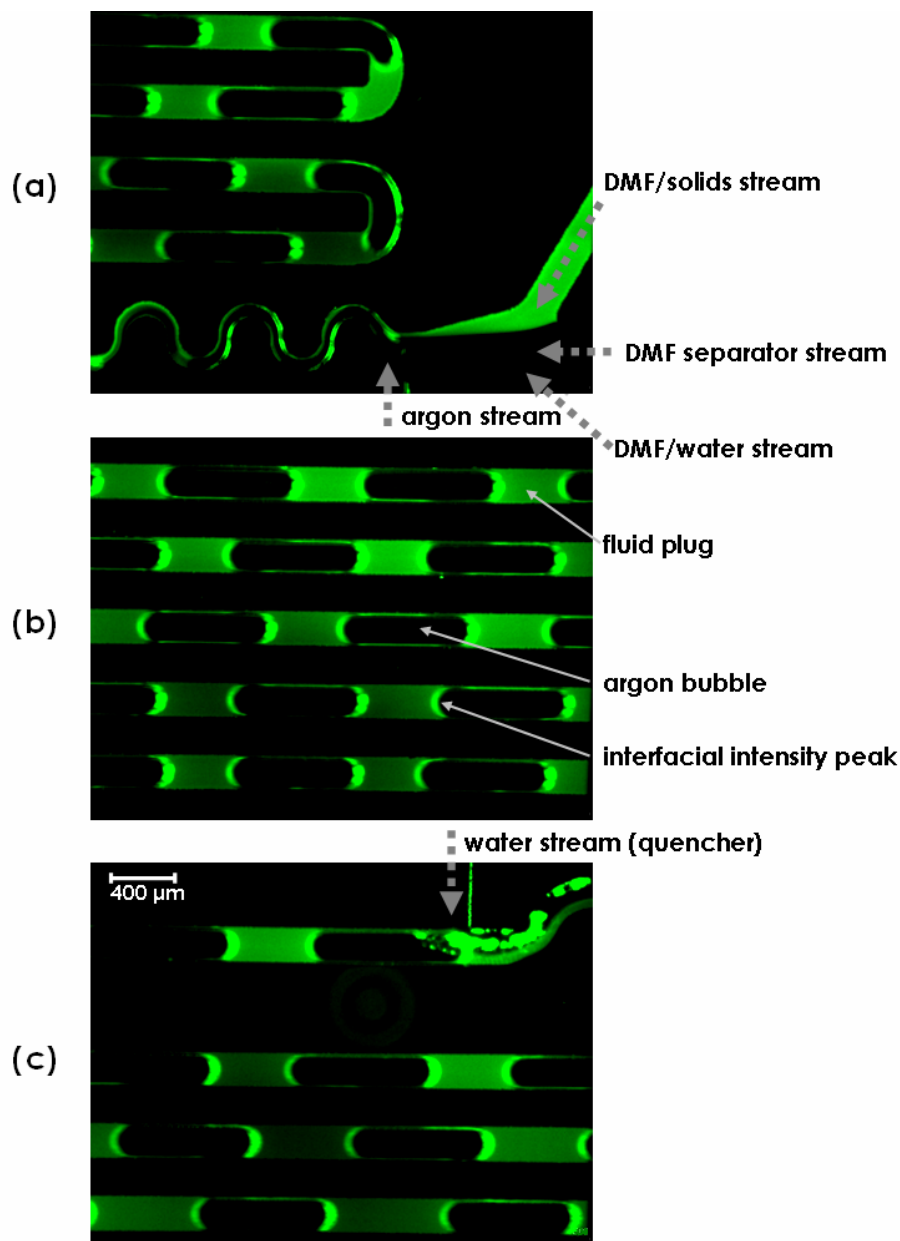


Figure 3.8: QD emission in the microfluidic gas-liquid bubble reactor during operation: the images were captured at (a) the injector, (b) the middle of the growth channel and (c) at the quencher. These images were captured in the 200 mm reactor at a steady-state water concentration was 4 wt% with the on-chip quencher in operation (prior to the breakdown of flow). The variations in fluorescent intensity of the plugs from the bottom to top of each image is a byproduct of a non-uniform distribution of excitation light and does not indicate any change in the properties of QDCMs. (contrast ratio and brightness have been adjusted for clarity of presentation)

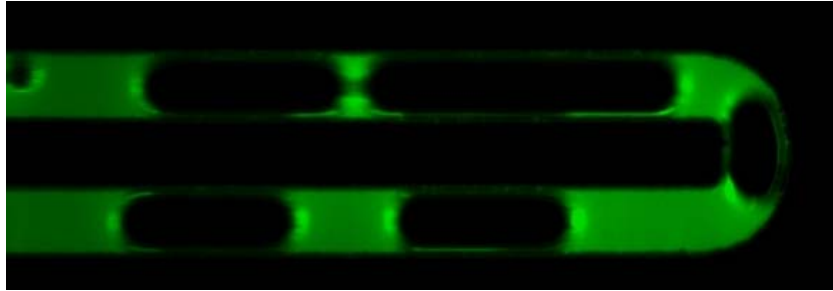


Figure 3.9: Fluorescein emission in multiphase fluorescein/water-argon system. The intensity peaks seen at the two-phase interface are attributed to total internal reflection at the gas-liquid interface.

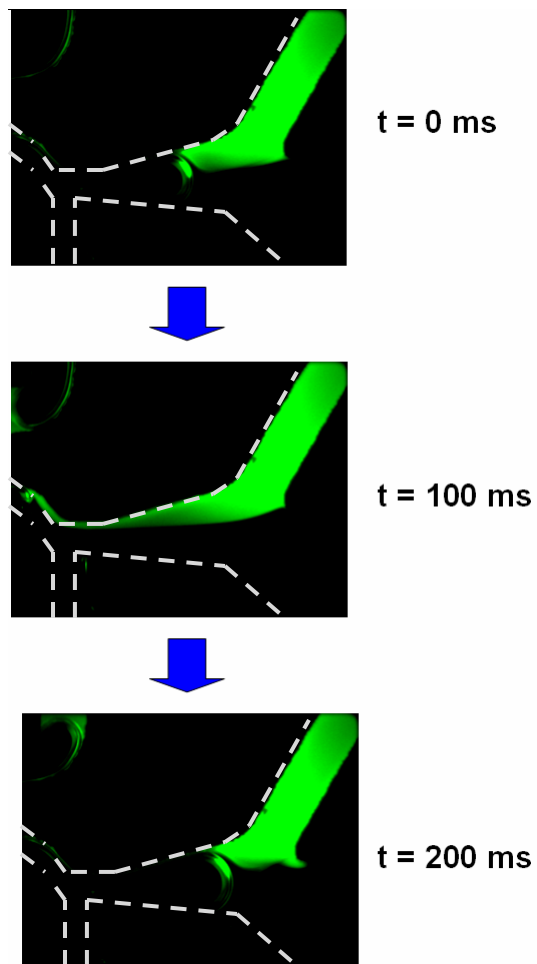


Figure 3.10: Bubble formation process at the injector of the gas-liquid reactor. These images were taken at 100 ms intervals. The steady-state water concentration was 4 wt%. (contrast ratio and brightness have been adjusted for clarity of presentation)

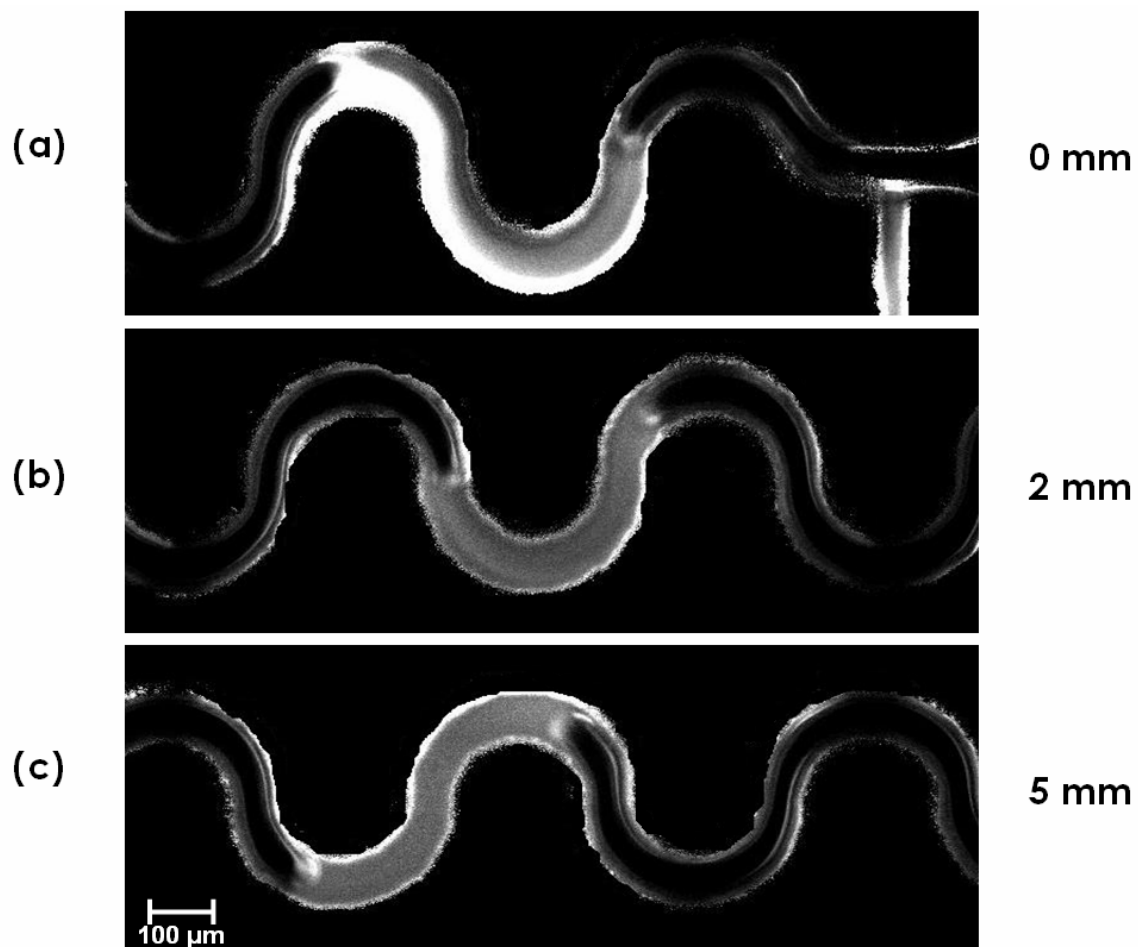


Figure 3.11: Normalized fluorescein emission taken at three downstream locations in the mixing channel during the trial where fluorescein was added to water and the steady-state water concentration was 33 wt%. The images were captured at downstream distances of (a) 0 mm, (b) 2 mm and (c) 5 mm from the injector.

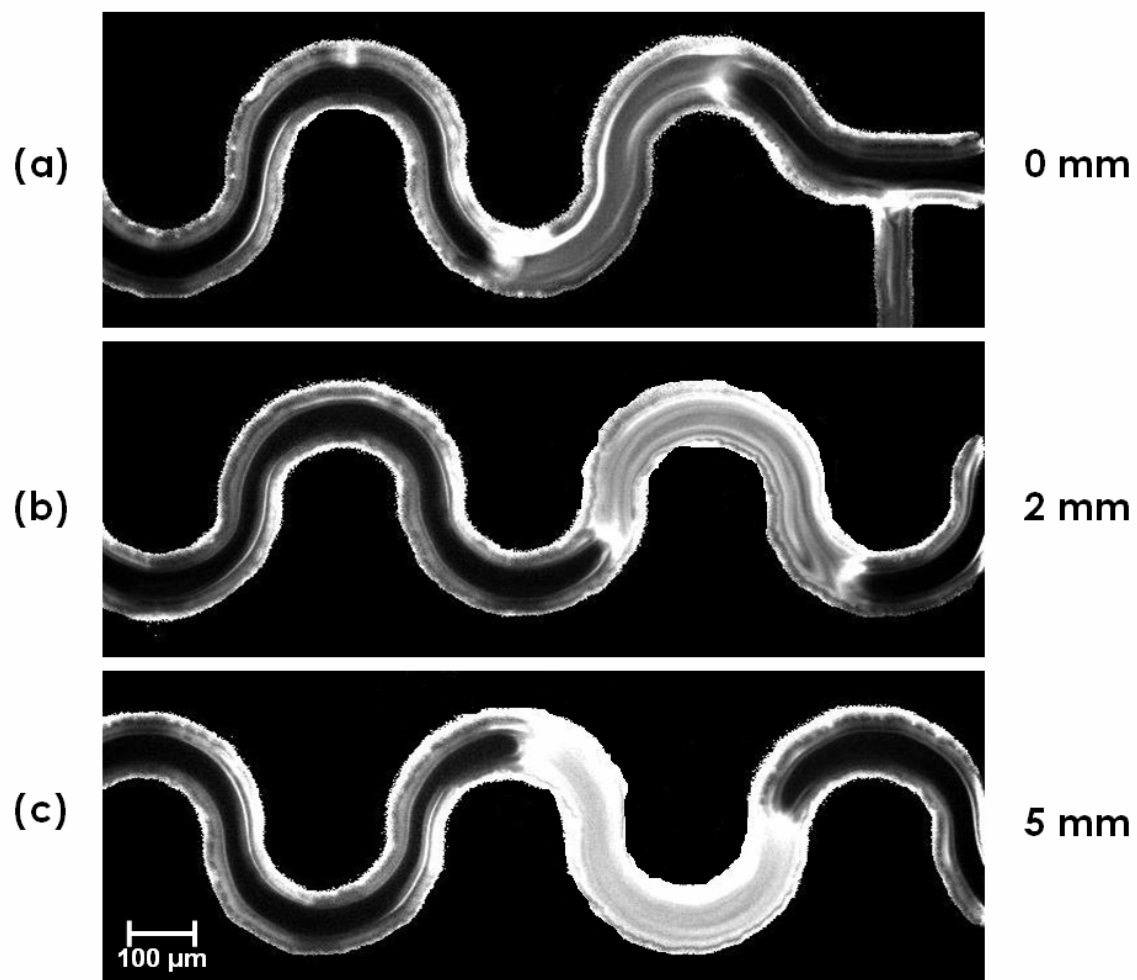


Figure 3.12: Normalized QD emission in the mixing channel for the 33 wt% water trial. The images were captured at downstream distances of (a) 0 mm, (b) 2 mm and (c) 5 mm from the injector.

3.3.2.2 TEM Results

Off-chip TEM imaging of QDCMs formed in this microfluidic reactor under different steady-state water concentrations and on-chip residence times enabled a quantitative analysis of QDCM size and polydispersity. TEM images of QDCMs prepared at a steady-state water concentration of 4 wt% in the 200 and 740 mm long reactors are shown in Figures 3.13 and 3.14 respectively. TEM images of QDCMs prepared at a steady-state water concentration of 33 wt% are shown in Figure 3.15. The statistical data of QDCM distributions for all three trials is shown in Figure 3.16.

The mean particle diameter of QDCMs formed in the 200 mm reactor at a steady-state water concentration of 4 wt% was 81 nm with a standard deviation of 30% of the mean particle diameter. This size distribution was very similar to the size distributions of QDCMs formed in the flow-focusing reactor at the same water concentration. However, the flow-focusing reactor was operated using an initial polymer concentration of 2 wt% in DMF as oppose to a value of 1 wt% used here. The reduction in the initial polymer concentration was necessary in order to reduce the occurrences of particle conglomeration in the reactor. It has been demonstrated that reducing the solids concentration in DMF prior to water addition significantly reduces the mean particle diameter of QDCM formations [Yusuf et al. (2007a)]. Therefore, it is likely that the rapid stirring motion inside the gas-liquid reactor increases the growth rate of QDCMs when compared to the flow-focusing reactor. The mean particle diameter of QDCMs formed in the 740 mm reactor at a steady-state water concentration of 4 wt% was 75 nm with a standard deviation of 22.5% of the mean. Interestingly, the QDCMs formed in the

longer channel were smaller and less polydisperse despite the longer grow time available in the longer reactor. This result is in contrast to the more intuitive operation of the sheath-flow reactor chips in which longer growth times (channel length) resulted in larger populations. The size decrease with channel length in the gas-liquid chip is attributed here to QDCM processing/manipulation within the liquid plugs. Specifically, the vortex motion inside the fluid plugs may promote redistribution of the building block particles between individual QDCMs, producing a more uniform population over time. Such processing is possible with a water concentration of 4 wt%, as the QDCMs are soft and their building block constituents can easily be redistributed. Therefore, the microfluidic gas-liquid reactors developed may provide a novel, albeit somewhat unexpected, technique for reducing the polydispersity of QDCM formations.

The mean particle diameter of QDCMs formed in the 200 mm reactor at a steady-state water concentration of 33 wt% was 58 nm with a standard deviation of 62% of the mean. Although the mean particle diameter here was the lowest of the three trials, larger individual QDCMs formed, some exceeding 200 nm in diameter. These large QDCMs were balanced by a population of much smaller QDCMs with diameters under 20 nm. Therefore, operating the gas-liquid reactor at a steady-state water concentration of 33 wt% was not a viable method of producing QDCMs with low polydispersity.

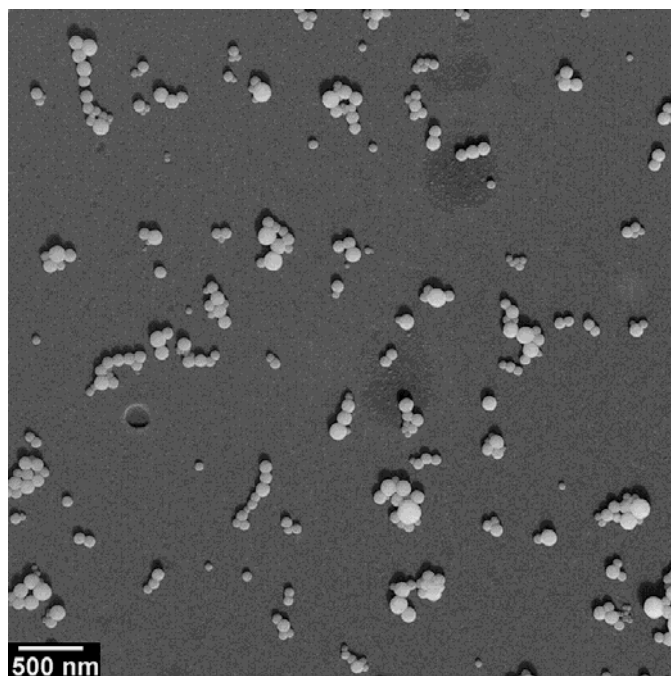


Figure 3.13: Representative shadowed TEM images of QDCMs formed in a 200 mm gas-liquid reactor at a steady-state water concentration of 4 wt%. (TEM images were black/white inverted for presentation).

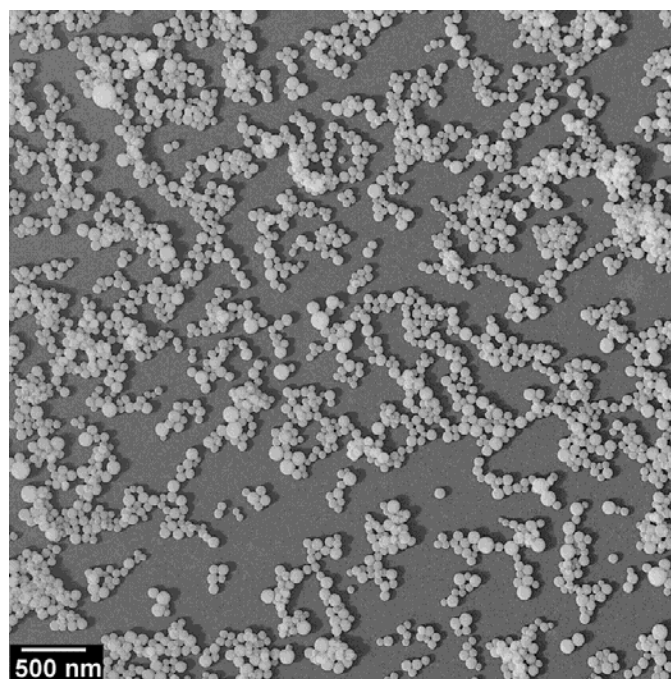


Figure 3.14: Representative shadowed TEM images of QDCMs formed in a 740 mm gas-liquid reactor at a steady-state water concentration of 4 wt%. (TEM images were black/white inverted for presentation).

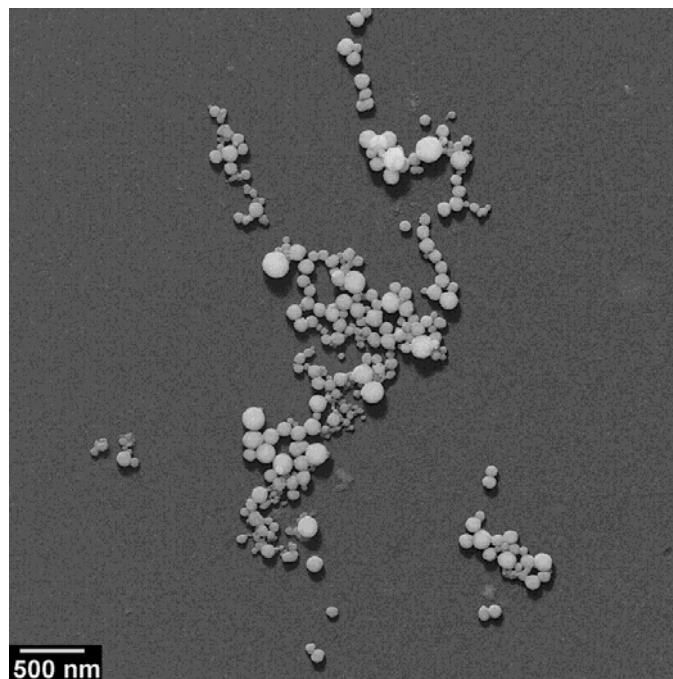


Figure 3.15: Representative shadowed TEM images of QDCMs formed in a 200 mm gas-liquid reactor at a steady-state water concentration of 33 wt%. (TEM images were black/white inverted for presentation).

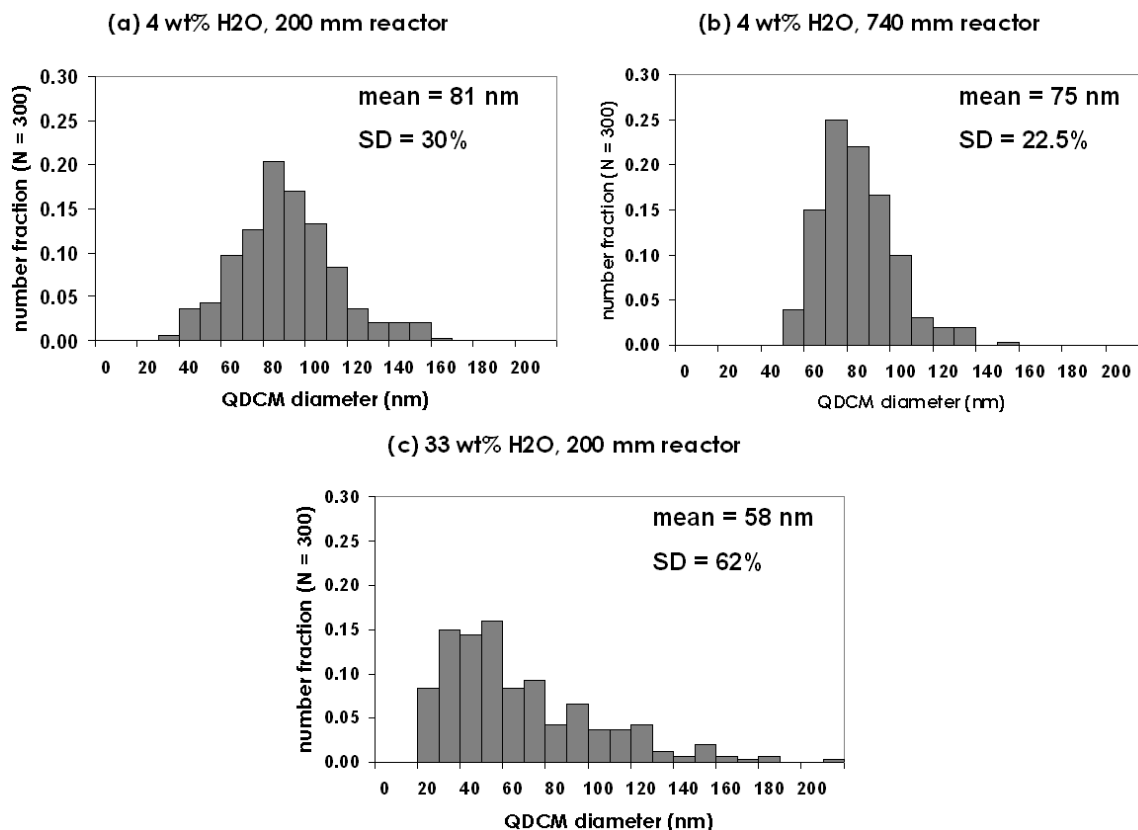


Figure 3.16: QDCM particle size distributions and statistics for QDCMs formed in the microfluidic gas-liquid reactor. In each case, the steady-state water concentration and reactor length were (a) 4 wt% and 200 mm, (b) 4 wt% and 740 mm and (c) 33 wt% and 200 mm.

3.4 Summary

In summary, chip-based multiphase microfluidic reactors were used to facilitate and control the self-assembly of CdS QDs into aqueous spherical assemblies called QDCMs. Water was introduced into a blend solution of hydrophobic CdS QDs stabilized with a PS brush layer and PS-*b*-PAA stabilizing chains dissolved in DMF to initiate the self-assembly process. A second phase of either oil or gas was introduced into the reactor

in order to isolate the reagents into discrete fluid droplets/plugs where the constituents mixed rapidly due to chaotic advection.

A droplet microfluidic reactor was developed first employing an immiscible oil phase. A surfactant was initially employed with the aim to induce full wetting of the oil phase (and thus full compartmentalization of the droplet phase in which QDCM formation occurs). Although this strategy is effective for aqueous droplets, it did not result in stable droplet formation for DMF-containing solutions employed here. It was also found that the surfactant was miscible in the droplets, and thus somewhat ineffectual as a surface-active agent, and also potentially disrupting to the QDCM formation process. Stable operation was achieved with the droplet reactor at a steady-state water concentration of 4 wt% without the addition of the surfactant to the PFD. Further development of the droplet reactor was discontinued, however, in favor of an alternative reactor strategy.

A gas-liquid microfluidic reactor was developed as an improvement on the droplet reactor. Most importantly from the perspective of QDCM self-assembly, it could be safely assumed that the argon gas phase does not participate in the QDCM formation process and no additional components such as surfactants were required in gas-liquid reactors. A fluorescent tracer in the water stream in the gas-liquid reactor showed that the time required for water to fully mix into the DMF/solids constituents was less than 1 second. This was an improvement over the ~12 seconds required in the flow-focusing reactors of Chapter 2. Off-chip TEM imaging of QDCMs formed in this microfluidic reactor under different steady-state water concentrations and on-chip residence times enabled a quantitative analysis of QDCM size and polydispersity. It was found that

adjusting the steady-state water concentration in the reactor from 4 to 33 wt% produced QDCMs with mean particle diameters of 81 and 58 nm respectively with standard deviations 30 and 62 % of their respective mean particle diameters. This trend was similar to that observed in the sheath-flow reactors, and polydispersity of QDCMs formed in this manner was also similar. At a steady-state water concentration of 4 wt%, however, increasing the reactor length from 200 to 740 mm resulted in smaller QDCMs with less polydispersity (mean particle diameter = 75 nm, standard deviation = 22.5%). As such, control over QDCM polydispersity was demonstrated in the gas-liquid reactor and increasing its length even further may provide of means for further reducing the polydispersity of QDCM formations. The size decrease with channel length was attributed to QDCM processing/manipulation by way of the chaotic mixing within the liquid plugs. This result is in contrast to the more intuitive operation of the sheath-flow reactor chips, and indicates the potential for on-chip post-formation processing of QDCMs (to achieve decreased polydispersity) following self-assembly.

Chapter 4

CONCLUSIONS AND FUTURE WORK

4.1 Contributions of this Thesis

This thesis was devoted to the application of microfluidics for the controlled self-assembly of light-emitting nanoparticles called quantum dot compound micelles (QDCMs). The contributions of this work include the design and development of a number of microfluidic reactors where the self-assembly process could be monitored on-chip and the size-distributions of QDCM populations could be controlled by adjusting running parameters (i.e. flowrates, water concentrations and on-chip residence times). To the author's knowledge, this work represents the first demonstration of microfluidic self-assembly of colloidal QDs. Also in the context of the UVic Microfluidics Lab, the development of multiphase microfluidics represents a first, and the multistep, multiphase chips developed through this chapter are the most complex chips developed in the lab to date. The key contributions are summarized below.

4.1.1 QDCM Self-Assembly in a Microfluidic T-sensor

A microfluidic T-sensor was designed to facilitate the self-assembly of QDCMs over sufficiently long time-scales that the process could be monitored using fluorescence microscopy. This strategy involved combining a stream containing the PS-CdS and PS(665)-*b*-PAA(68) constituents in DMF with a second stream containing a mixture of DMF and water in a long microfluidic channel. As the two streams mixed via cross-stream diffusion, QDCMs were formed where the local water concentration exceeded a critical water content (cwc). The onset QDCM formation was indicated by an increase in the brightness of the fluorescent signal due to increased light scattering of QD emission. This system provided a novel technique for real-time monitoring of the QDCM self-assembly process in a microfluidic reactor.

4.1.2 QDCM Self-Assembly in a Microfluidic Focuser

A microfluidic two stage flow-focusing reactor was designed to facilitate the size-controlled self-assembly of QDCMs. Through TEM imaging, it was demonstrated that adjusting controlling parameters such as initial water concentration and flowrates provided a means for controlling the mean particle diameters of QDCM populations. Steady-state water concentrations of 4, 8 and 33 wt% in DMF yielded QDCM populations with mean-particle sizes of 85, 67 and 46 nm respectively. Adjusting the flowrate inside the reactor from 3 to 9 $\mu\text{L}/\text{min}$ reduced the mean particle diameters of QDCM populations by 4 nm at all three water concentrations, providing a small but

notable means of size-control. In all cases, the polydispersity of QDCMs formed in this reactor was similar to those formed using previous self-assembly methodologies [Yusuf et al. (2007a)].

4.1.3 QDCM Self-Assembly in a Multiphase Droplet Reactor

Multiphase microfluidic systems have a number of characteristics such as a rapid mixing and small residence time distributions (RTD) which make them promising candidates for the controlled self-assembly of QDCMs with low polydispersity. A multiphase reactor was designed where the reagents for QDCM formation and immiscible oil were combined causing the oil to form into discrete droplets separated by fluid plugs containing the reagents. A surfactant was initially employed with the aim to induce full wetting of the oil phase (and thus full compartmentalization of the droplet phase in which QDCM formation occurs). It was found, however, that the surfactant was miscible in the droplets, and thus potentially affecting the QDCM self-assembly process. Without the addition of the surfactant, stable operation was achieved with the droplet reactor at a steady-state water concentration of 4 wt%. Further development of the droplet reactor was discontinued, however, in favor of a more robust gas-liquid reactor strategy.

4.1.4 QDCM Self-Assembly in a Multiphase Gas-Liquid Reactor

A multiphase reactor was designed where the reagents for QDCM self-assembly were combined with a gas, argon, in a microfluidic reactor causing the periodic formation of gas bubbles separated by liquid plugs. Stable operation was demonstrated for the two water concentrations and two reactor lengths tested. A fluorescent tracer in the water stream in the gas-liquid reactor showed that the time required for water to fully mix into the DMF/solids constituents was less than 1 second for this chip (an order-of-magnitude improvement over the flow-focusing reactor of Chapter 2). Through off-chip TEM imaging, it was demonstrated that increasing the length of the reactor provided a means for reducing the mean size and polydispersity of QDCM populations. At a steady-state water concentration of 4 wt%, increasing the reactor length from 200 to 740 mm reduced the standard deviation of QDCM populations from 30% to 22.5% of their respective mean particle diameters. This result is in contrast to the more intuitive operation of the sheath-flow reactor chips, and indicates the potential for on-chip post-formation processing of QDCMs (to achieve decreased polydispersity) following on-chip QDCM self-assembly.

4.2 Proposed Extensions of This Work

There are a number of microfluidics-based strategies that may further reduce the polydispersity of QDCMs formed in the microfluidic reactors developed in this work. Two of these strategies, one for the flow-focusing reactor and the other for the multiphase

gas-liquid reactor, are described below. Also, some interesting large scale particle formations observed in this work are described which are interesting candidates for future study.

4.2.1 On-chip Diffusion-Based QDCM Size-Sorting in a Flow-Focusing Microfluidic Reactor

From the findings from Chapter 2, it is unlikely that single-phase microfluidic reactors can facilitate the self-assembly of low polydispersity QDCMs due to long mixing times and large residence time distributions associated with these systems. However, diffusion based on-chip sorting techniques may provide a method for post-assembly size-sorting of QDCMs. Spherical nanoparticles dissolved in a bulk liquid experience a rate of cross-stream diffusion that is inversely proportional to their diameters (Equation 2.6). This has led to the development of a microfluidic particle sorting device known as an H-filter [Weigl and Yager (1999); Jandik et al. (2002); Hatch et al. (2004)]. In an H-filter, two laminar streams, one containing polydisperse particles, are brought into contact for a short time before being branched off in different directions (think of a sideways H). While the two streams are in contact they are free to mix via cross-stream diffusion. Since smaller particles diffuse faster than larger ones, more of them will traverse over to the second stream, thus providing a technique for separating particles based on size [Jandik et al. (2002)]. The addition of a series of H-filters to the end of the flow-focusing reactor may provide a means of size-sorting QDCMs on-chip following self-assembly.

4.2.2 Further Enhancement of the Gas-Liquid Microfluidic Reactor

In Chapter 3, it was demonstrated that increasing the length of the gas-liquid reactor significantly reduced the polydispersity of QDCM populations at a steady-state water concentration of 4 wt%. It is likely that the vortex motion inside the fluid plugs promoted the redistribution of the building block particles of QDCMs, evening out their sizes over time. Further experimentation should be conducted using gas-liquid reactors with even longer lengths to determine if further reduction in QDCM polydispersity can be achieved. Increasing the operating flowrate of the gas-liquid reactor may also provide a means for reducing QDCM polydispersity since this would result in faster mixing of reagents and more rigorous particle circulation inside fluid plugs [Song et al. (2003)]. Enhancement of the microfluidic gas-liquid reactor by fine-tuning these controllable parameters may hold the key for producing less polydisperse QDCMs.

4.2.3 The Formation of Large-Scale Quantum Dot Structures in a Microfluidic Device

During some of the experiments conducted in this work, the on-chip formation of large QDCM structures, with dimensions as large as 100 μm , was observed. These very large QDCM structures, were seen in both the sheath-flow and multiphase reactors and formed at times when the flow inside the reactors was unstable, and/or residence times were very long. Figure 4.1 shows fluorescence images of some of these formations formed inside a microfluidic device. Controllable and predictable formation of these

large scale particles was not achieved under steady-state operating conditions. These structures are much larger than the particle sizes targeted through this work, and thus beyond the scope of this thesis. They are included here, however, as a point of interest, and a potential avenue for future work. Further investigation could focus on the mechanisms of formation and to determine if the assembly of these large scale structures can be systematically controlled through microfluidics. It may also be of interest to use the cross-sectional channel geometry to influence the shape of these structures, for instance rods or disks could potentially be produced.

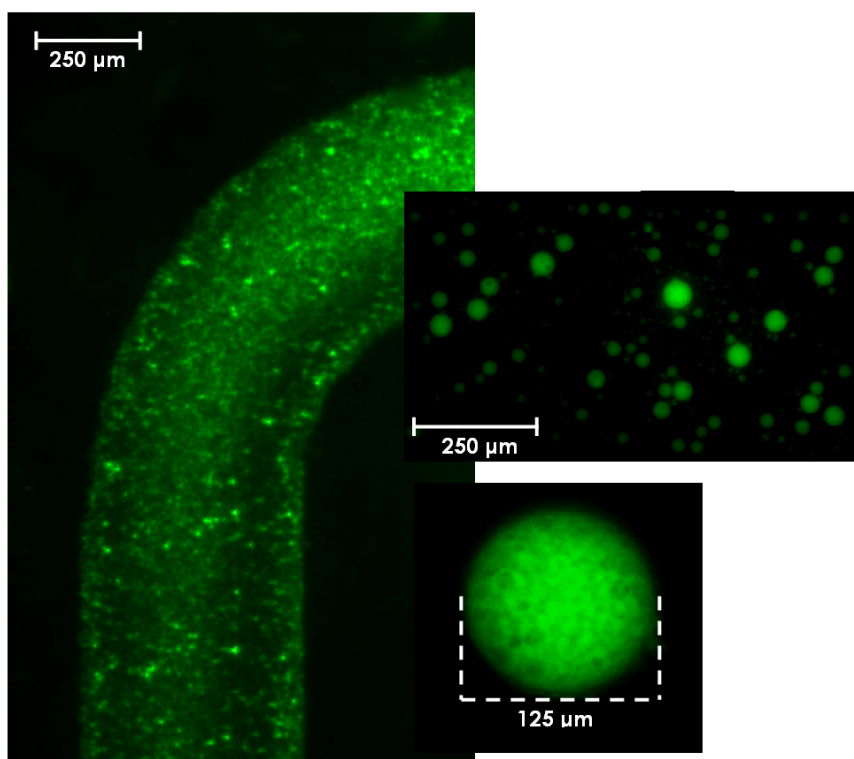


Figure 4.1: Large QD structures formed inside microfluidic reactors. The largest particles shown have dimensions on the order of 100 μm.

REFERENCES

- Acheson, D.J., 1990, "Elementary Fluid Mechanics", *Oxford University Press*, New York.
- Atencia, J. and Beebe, D.J., "Controlled Microfluidic Interfaces", *Nature*, **437**, pp. 648-655.
- Bazylak, A., Sinton, D., Djilali, N. (2005) "Improved Fuel Utilization in Microfluidic Fuel Cells: A Computational Study." *Journal of Power Sources*, **143**, pp. 57-66
- Beebe, D.J., Mensing, G.A. and Walker, G.M., 2002, "Physics and Applications of Microfluidics in Biology", *Annual Review of Biomedical Engineering*, **2**, pp. 261-286.
- Biddiss, E., Erickson, D. and Li, D., 2004, "Heterogeneous Surface Charge Enhanced Micromixing For Electrokinetic Flows", *Analytical Chemistry*, **76**, pp. 3208-3213.
- Bird, R.B., Stewart, W.E. and Lightfoot, E.N., 1960, "Transport Phenomena", John Wiley & Sons, New York.
- Bringer, M.R., Gerdts, C.J., Song, H., Tice, J.D. and Ismagilov, R.F., 2004, "Microfluidics Systems for Chemical Kinetics That Rely on Chaotic Mixing in Droplets", *Philosophical Transactions Royal Society London*, **362**, pp. 1087-1104.
- Brus, L., 1991, "Quantum Crystallites and Non-Linear Optics", *Applied Physics A*, **53**, pp. 465-474.
- Chan, W.C.W., Maxwell, D.J., Gao, X., Bailey, R.E., Han, M. and Nie, S., 2002, "Luminescent quantum dots for multiplexed biological detection and imaging", *Current Opinion in Biotechnology*, **13**, pp. 40-46.
- Chan, E.M, Mathies, R.A. and Alivisatos, A.P., 2002, "Size-Controlled Growth of CdSe Nanocrystals in Microfluidic Reactors", *Nano Letters*, **3 (2)**, pp. 199-201.
- Chan, E.M., Alivisatos, A.P. and Mathies, R.A., 2005, "High-Temperature Microfluidic Synthesis of CdSe Nanocrystals in Nanoliter Droplets", *Journal of American Chemical Society*, **127**, pp. 13854-13861.
- Chen, Y. and Rosenzweig, Z., 2002, Luminescent CdSe Quantum Dot Dope Stabilized Micelles", *Nano Letters*, **2 (11)**, pp. 1299-1302.
- Chen, Z-R., Kornfield, J.A., Smith, S.D., Grothaus, J.T. and Satkowski, M.M., 1997, "Pathways to Macroscale Order in Nanostructured Block Copolymers", *Science*, **277**, pp. 1248-1253.
- Cohen, M.L. and Chelikowsky, J.R., 1988, "Electronic Structure and Optical Properties of Semiconductors", Springer-Verlag, New York.

Coleman, J.T., 2005, "Electrokinetic Processes for Microfluidic Devices", M.A.Sc. Thesis, *Department of Mechanical Engineering, University of Victoria*.

Coleman, J.T., McKechnie, J. and Sinton D., 2006, "High-Efficiency Electrokinetic Micromixing Through Sequential Injection and Expansion", *Lab on a Chip*, **6**, pp. 1033-1039.

Coleman, J.T. and Sinton, D., 2004, "Microfluidic Mixing Through Sequential Sample Injection With Rapid Expansion", *International Mechanical Engineering Congress and RD&D Exposition, Anaheim, CA, USA*, Nov.13-19.

Cottam, B.F., Krishnadasan, S., deMello, A.J., deMello, J.C. and Shaffer, M.S.P., 2007, "Accelerated Synthesis of Titanium Oxide Nanostructures Using Microfluidic Chips", *Lab on a Chip*, **7**, pp. 167-169.

Cubaud, T., Ulmanella, U. and Ho, C-M., 2004, "Two-Phase Flow in Microchannels with Surface Modifications", *5th International Conference on Multiphase Flow*, Yokohoma, Japan, May 30 – June 4.

De Leebeeck, A., 2006, "Nanofluidic Species Transport and Nanostructure Based Detection On-Chip", M.A.Sc. Thesis, *Department of Mechanical Engineering, University of Victoria*.

deMello, A.J., 2006, "Control and Detection of Chemical Reactions in Microfluidic Systems", *Nature*, **442**, pp. 394-402.

Dolnik, V., Liu, S. and Jovanich, S., 2000, "Capillary Electrophoresis on Microchip", *Electrophoresis*, **21**, pp. 41-54.

Dreyfus, R., Tabeling, P. and Willaime, H., 2003, "Ordered and Disordered Patterns in Two-Phase Flows in Microchannels", *Physical Review Letters*, **90 (14)**, pp. 144505-1-144505-4.

Duffy, D.C., McDonald, J.C., Schueller, O.J. A., Whitesides, G. M., 1998, "Rapid Prototyping of Microfluidic Systems in Poly(dimethylsiloxane)", *Analytical Chemistry*, **70**, pp 3781 – 3789.

Dyer, C.K., 2002, "Fuel Cells for Portable Applications", *Journal of Power Sources*, **106**, pp. 31-34.

Epstein, I.R., 2007, "Can Droplets and Bubbles Think?", *Science*, **315**, pp. 775-776.

Erickson, D. and Li, D., 2004, "Integrated Microfluidic Devices", *Analitica Chimica Acta*, **507**, pp. 11 – 26.

Galambos, P., Forster, F.K. and Weigl, B.H., 1997, "A Method for Determination of pH Using a T-sensor", *International Conference on Solid-State Sensors and Actuators*, Chicago, June 16-19.

Gao, Z. and Eisenberg, A., 1993, "A Model of Micellization for Block Copolymers in Solutions", *Macromolecules*, **26**, pp. 7353-7360.

Garstecki, P., Fuerstman, M.J., Stone, H.A., and Whitesides, G.M., 2006, "Formation of Droplets and Bubbles in a Microfluidic T-junction- Scaling and Mechanism of Break-up", *Lab on a Chip*, **6**, pp. 437-446.

Gobby, D., Angeli, P. and Gavriilidis, A., 2001, "Mixing Characteristics of T-type Microfluidic Mixers", *Journal of Micromechanics and Microengineering*, **11**, pp. 126-132.

Günther, A. and Jensen, K.F., "Multiphase Microfluidics: From Flow Characteristics to Chemical and Materials Synthesis", *Lab on Chip*, **6**, pp. 1487-1503.

Günther, A., Khan, S.A., Thalmann, M., Trachsel, F. and Jensen, K.F., 2004, "Transport and Reaction in Microscale Segmented Gas-Liquid Flow", *Lab on a Chip*, **4**, pp. 278-286.

Hatch, A., Garcia, E. and Yager, P., 2004, "Diffusion-Based Analysis of Molecular Interactions in Microfluidic Devices", *Proceeding of the IEEE*, **92(1)**, pp. 126-139.

Hatch, A., Kamholz, A.E., Hawkins, K.R., Munson, M.S., Schilling, E.A., Weigl, B.H. and Yager, P., 2001, "A Rapid Diffusion Immunoassay in a T-Sensor", *Nature Publishing Group*, **19**, pp. 461-465.

Hertzog, D.E., Ivorra, B., Mohammadi, B., Bakajin, O. and Santiago, J.G., 2006, "Optimization of a Microfluidic Mixer for Studying Protein Folding Kinetics", *Analytical Chemistry*, **78**, pp. 4299-4306.

Hu, Y.Z., Lindberg, M. and Koch, S.W., 1990, "Theory of Optically Excited Intrinsic Semiconductor Quantum Dots", *Physical Review B*, **42 (3)**, pp. 1713-1723.

Inoue, S. and Spring, K.R., 1997, "Video Microscopy the Fundamentals, 2nd Edition", *Plenum Press*, New York.

Ismagilov, R.F., Stroock, A.D., Kenis, J.A., Stone, H.A. and Whitesides, G., 2000, "Experimental and Theoretical Scaling Laws For Transverse Diffusive Broadening in Two-Phase Laminar Flows in Microchannels", *Applied Physics Letters*, **76 (17)**, pp. 2376-2378.

Jacobsen, S.C., Culbertson, C.T., Daler, J.E. and Ramsey, J.M., 1998, "Microchip Structures for Submillisecond Electrophoresis", *Analytical Chemistry*, **70**, pp. 3476-3480.

Jahn, S.C., Vreeland, W.N., Gaitan, M. and Locasio, L.E., 2004, "Controlled Vesicle Self-Assembly in Microfluidic Channels with Hydrodynamic Focusing", *Journal of American Chemical Society*, **126(9)**, pp. 2674-2675.

Jandik, P., Weigl, B.H., Kessler, N., Cheng, J., Morris, C.J., Schulte, T. and Avdalovic, N., 2002, "Initial study of using a laminar fluid diffusion interface for sample preparation in high-performance liquid chromatography", *Journal of Chromatography*, **954**, pp. 30-40.

Johnson, L.V., Walsh, M.L., Bockus, B.J. and Chen, L.B., 1981, "Monitoring of Relative Mitochondrial Membrane Potential in Living Cells by Fluorescence Microscopy", *The Journal of Cell Biology*, **88**, pp. 526-535.

Jonscher, A.K., 1965, "Solid Semiconductors", *Dover Publication Inc.*, New York.

Kakuta, M., Jayawickrama, D.A., Wolters, A.M., Manz, A. and Sweedler, J.V., 2003, "Micromixer-Based Time-Resolved NMR: Applications to Ubiquitin Protein Conformation" *Analytical Chemistry*, **75**, pp. 956-960.

Kamholz, A. E., 2004, "Proliferation of Microfluidics in Literature and Intellectual Property", *Lab on Chip*, **4**, pp. 16N-20N.

Kamholz, A.E., Weigl, B.H., Finlayson, B.A. and Yager, P., 1999, "Quantitative Analysis of Molecular Interaction in a Microfluidic Channel: The T-sensor", *Analytical Chemistry*, **71 (23)**, pp. 5340-5347.

Kan, S., Aharoni, A., Mokari, T. and Banin, U., 2004, "Shape control of III-V semiconductor nanocrystals: Synthesis and properties of InAs quantum rods", *Faraday Discussion*, **125**, pp.23-38.

Kataoka, K., Harada, A. and Nagasaki, Y., 2001, "Block copolymer micelles for drug delivery: design, characterization and biological significance", *Advanced Drug Delivery Review*, **47 (1)**, pp. 113-131.

Kirby, B. and Hasselbrink Jr., E.F., 2004, "Zeta Potential of Microfluidic Substrates: 1. Theory, Experimental Techniques and Effects on Separations", *Electrophoresis*, **25**, pp. 187-202.

Kjeang, E., Proctor, B. T., Brolo, A. G., Harrington, D. A., Djilali, N., Sinton, D. (accepted 2007) "High-Performance Microfluidic Vanadium Redox Fuel Cell." *Electrochimica Acta*, accepted.

Krishnadasan, S., Tovilla, J., Vilar, R., deMello, A. J. and deMello J. C., 2004, "On-line analysis of CdSe nanoparticle formation in a continuous flow chip-based microreactor", *Journal of Materials Chemistry*, **14**, pp. 2655-2660.

- Lee, J.N., Park, C. and Whitesides, G.M., 2003, "Solvent Compatibility of Poly(dimethylsiloxane)-Based Microfluidic Devices", *Analytical Chemistry*, **75**, pp. 6544-6554.
- Loss, D. and DiVincenzo, D.P., 1998, "Quantum Computation with Quantum Dots", *Physical Review A*, **57** (1), pp. 120-126.
- Malmstadt, N., Nash, M.A., Purnell, R.F., and Schmidt, J.J., 2006, "Automated Formation of Lipid-Bilayer Membranes in a Microfluidic Device", *Nano Letters*, **6** (9), pp. 1961-1965.
- Malmsten, M. and Lindman, B., 1992, "Self-Assembly in Aqueous **Block** Copolymer Solutions", *Macromolecules*, **25**, pp. 5440-5445.
- Marsh, J.H., Bhattacharyya, D., Helmy, A.S., Avrutin, E.A. and Bryce, A.C., 2000, "Engineering Quantum-Dot Lasers", *Physica E*, **8**, pp. 154-163.
- McDonald, J. C., Duffy, D.C., Anderson, J.R., Chiu, D.T., Wu, H., Schueller, O.J.A, Whitesides, G.M., 2000, "Fabrication of microfluidic systems in poly(dimethylsiloxane)", *Electrophoresis*, **21**, pp. 27-40.
- McKechnie, J., 2006, "Fabrication of Microfluidic Devices with Applications to Membraneless Fuel Cells", M.A.Sc. Thesis, *Department of Mechanical Engineering, University of Victoria*.
- MicroChem, *Nano SU-8: Negative tone photoresist, formulation 2-25*. Newton, MA, 2002a.
- MicroChem, *Nano SU-8: Negative tone photoresist, formulation 50-100*. Newton, MA, 2002a.
- Moffitt, M., Vali, H. and Eisenberg, A., 1998, "Spherical Assemblies of Nanoparticles in Water-Soluble Block Copolymer Aggregates", *Chemistry of Materials*, **10**, pp. 1021-1028.
- Munson, M.S., Hawkins, K.R., Hasenbrank, M.S. and Yager, P., 2005, "Diffusion Based Analysis in a Sheath-flow Microchannel: The Sheath-flow T-sensor", *Lab on Chip*, **5**, pp. 856-862.
- Ng, J. Gitlin, I., Stroock, A.D. and Whitesides, G.M., 2002, "Components for Integrated Poly(dimethylsiloxane) Microfluidic Systems", *Electrophoresis*, **23**, pp. 3461-3473.
- Nguyen, N-T. and Wu, Z., 2004, "Micromixers – A Review", *Journal of Micromechanics and Microengineering*, **15**, pp. R1-R16.

Nie, Z., Li, W., Seo, M., Xu, S. and Kumacheva, E., 2006, "Janus and Ternary Generated by Microfluidic Synthesis: Design, Synthesis, and Self-Assembly", *Journal of the American Chemical Society*, **128**, pp. 9408-9412.

Nozik, A.J., 2002, "Quantum Dot Solar Cells", *Physica E*, **14**, pp. 115-120.

Owen, M. J. and Smith, P.J., 1994, "Plasma Treatment of Polydimethylsiloxane", *Journal of Adhesion Science and Technology*, **8**, pp. 1061-1224.

Park, N-M., Kim, T-S. and Parka, S-J., 2001, "Band gap engineering of amorphous silicon quantum dots for light-emitting diodes", *Applied Physical Letters*, **78 (17)**, pp. 2575-2577.

Periasamy, A. and Day, R.N., 2005, "Molecular Imaging: FRET Microscopy and Spectroscopy", *Oxford University Press*, Oxford, England.

Pinaud, F., Michalet, ., Bentolila, L.A., Tsay, J.M., Doose1, S., Li, J.J., Iyer, G., Weiss, S., 2005, "Advances in fluorescence imaging with quantum dot bio-probes", *Biomaterials*, **27**, pp. 1679-1697.

Prakash, M. and Gershenfeld, N., "Microfluidic Bubble Logic", *Science*, **315**, pp. 832-835.

Probstein, R.F., 1994, "Physiochemical Hydrodynamics", 2nd edn., *Wiley*, New York.

Purcell, E.M., 1976, "Life at Low Reynolds Number", *Amercian Journal of Physics*, **45 (1)**, pp.3-9.

Reimer, L., 1989, "Transmission Electron Microscopy: Physics of Image Formation and Microanalysis", *Springer-Verlag*, New York, NY.

Reyes, D.R., Iossifidis, D., Aurox, P-A. and Manz, A., 2002, "Micro Total Analysis Systems. 1. Introduction, Theory and Technology", *Analytical Chemistry*, **74**, pp. 2623-2636.

Reynolds, O., 1883, "An Experimental Investigation of the Circumstances Which Determine Whether the Motion of Water Shall be Direct or Sinuous, and of the Law of Resistance in Parallel Channels", *Philosophical Transactions of the Royal Society of London*, **174**, pp. 935-982.

Seo, M., Nie, Z., Xu, S., Mok, M., Lewis, P.C., Graham, R. and Kumacheva, E., 2005, "Continuous Microfluidic Reactors for Polymer Particles", *Langmuir*, **21**, pp. 11614-11622.

Shestopalov, I., Tice, J.D. and Ismagilov, R.F., 2004, "Multi-step synthesis of nanoparticles performed on millisecond time scale in a microfluidic droplet-based system", *Lab on Chip*, **4**, pp. 316-321.

Sharp, K.V., Adrian, R.J., Santiago, J. G. and Molho, J.I., 2002, "Liquid Flows in Microchannels", Chapter 6 in *The Mems Handbook*, CRC Press, New York, NY.

Sinton, D., 2004, "Macroscale Flow Visualization", *Microfluid Nanofluid*, **1**, pp. 2-21.

Sinton, D., Ren, L. and Li, D., 2003, "A Dynamic Loading Step for Microfluidic Chip Sample Injection", *Journal of Colloid and Interface Science*, **266**, pp. 448–456.

Squires, T.M. and Quake S.R., 2005, "Microfluidics: Fluid physics at the Nanoliter Scale", *Review of Modern Physics*, **77**, pp. 977-1026

Steinbacher, J.L., Moy, R.W.Y., Price, K.E., Cummings, M.A., Roychowdhury, C., Buffy, J.J., Olbricht, W.L., Haaf, M. and McQuade, D.T., 2006, "Rapid Self-Assembly of Core-Shell Organosilicon Microcapsules within a Microfluidic Device", *Journal of the American Chemical Society*, **128**, pp. 9442-9447.

Stone, H.A., Strook, A.D. and Ajdari, A., 2004, "Engineering Flows in Small Devices: Microfluidics Towards a Lab-on-a-Chip", *Annual Review of Fluid Mechanics*, **36**, pp. 381-411.

Song, H., Tice, J.D. and Ismagilov, R.F., 2003, "A Microfluidic System for Controlling Reaction Networks in Time", *Angewandte Chemie International Edition*, **42 No. 7**, pp. 767-772.

Termonia, Y., 1997, "Molecular Modeling of Structure Development upon Quenching of a Polymer Solution", *Macromolecules*, **30**, pp. 5367-5371.

Thorsen, T., Roberts, R.W., Arnold, F.H. and Quake, S.R., 2001, "Dynamic Pattern Formation in a Vesicle-Generating Microfluidic Device", *Physical Review Letters*, **86 (18)**, pp. 4163-4166.

Tice, J.D., Song, H., Lyon, A.D. and Ismagilov, R.F., 2003, "Formation of Droplets and Mixing in Multiphase Microfluidics at Low Values of the Reynolds and the Capillary Numbers", *Langmuir*, **19**, pp. 9127-9133.

Vilkner, T., Janasek, D. and Manz, A. 2004, "Micro Total Analysis Systems. Recent Developments", *Analytical Chemistry*, **76**, pp. 3373-3386.

Wang, C.-W. and Moffitt, M. G., 2004, "Surface-Tunable Photoluminescence from Block Copolymer-Stabilized Cadmium Sulfide Quantum Dots", *Langmuir*, **20**, pp. 11784-11796.

Weigl, B.H. and Yager, P., 1999, "Microfluidics Diffusion-Based Separation and Detection", *Science*, **283 (5400)**, pp. 346-347.

Wang, J., 2000, "From DNA Biosensors to Gene Chips. Nucleic Acids", *Nucleic Acids Research*, **28**, pp. 3011-3016.

White, F.M., 2003, "Fluid Mechanics: Fifth Edition", *McGraw Hill*, New York.

Wolfe, C.M., Holonyak, N. Jr. and Stillman, G.E., 1989, "Physical Properties of Semiconductors", *Prentice-Hall Inc.*, Englewood Cliffs, New Jersey.

Yen, B.K.H., Günther, A., Schmidt, M.A., Jensen, K.F. and Bawendi, M.G., 2005, "A Microfabricated Gas-Liquid Segmented Flow Reactor for High-Temperature Synthesis: The Case of CdSe Quantum Dots", *Angewandte Chemie International Edition*, **44**, pp. 5447-5451.

Yusuf, H., 2006, "A Multi-Step Self-Assembly Route to Three-Dimensional Block Copolymer-Semiconducting Nanoparticle Photonic Arrays with Structural Hierarchy", M.A.Sc. Thesis, *Department of Chemistry, University of Victoria*.

Yusuf, H., Kim, W-G., Lee, D. H., Guo, Y. and Moffitt, M. G., 2007a, "Size Control of Mesoscale Aqueous Assemblies of Quantum Dots and Block Copolymers", *Langmuir*, **23**, pp. 868-878.

Yusuf, H., Kim, W-G., Lee, D. H., Aleshyna, M., Brolo, A.G. and Moffitt, M. G., 2007b, "A Hierarchical Self-Assembly Route to Three-Dimensional Polymer-Quantum Dot Photonic Arrays", *Langmuir*, **23**, pp. 5251-5254.

Zhang, L., Shen, H. and Eisenberg A., 1997, "Phase Separation Behaviour and Crew-Cut Micelle Formation of Polystyrene-*b*-poly(acrylic acid) Copolymers in Solutions", *Macromolecules*, **30**, pp. 1001-1011.

Zhang, L. and Eisenberg, A., 1999, "Thermodynamic vs Kinetic Aspects in the Formation and Morphological Transitions of Crew-Cut Aggregates Produced by Self-Assembly of Polystyrene-*b*-poly(acrylic acid) Block Copolymers in Dilute Solutions", *Macromolecules*, **32**, pp. 2239-2249.